KARAZIN UNIVERSITY
CLASSICS AHEAD OF TIME

Kharkiv University
Bulletin

Chemical Series

Вісник Харківського національного університету імені В. Н. Каразіна серія

ХІМІЯ

34'2020

Вісник **Х**арківського **Н**аціонального **У**ніверситету
імені В. Н. Каразіна

СЕРІЯ «ХІМІЯ»
Вип. 34 (57)

Заснований 1935 року як
"Труди інституту хемії при Харківському державному університеті"

Харків 2020

ЗМІСТ

CONTENTS

СОДЕРЖАНИЕ

УДК 541.2+544.7

RECENT ADVANCES IN THEORETICAL INVESTIGATION OF TITANIUM DIOXIDE NANOMATERIALS. A REVIEW

M.M. Blazhynska[†,a], A.V. Kyrychenko[†,b], D.S. Stepaniuk[†,c], O.M. Korsun[†,d], S.M. Kovalenko[†,e], V.V. Ivanov[†,f], F.-A. Miannay[‡,g], A. Idrissi[‡,h], O.N. Kalugin[†,i]

† *V.N. Karazin Kharkiv National University, School of Chemistry, 4 Svobody sqr.,61022 Kharkiv, Ukraine*

‡ *University Lille, LASIR UMR8516, Cité Scientifique, 59655, Villeneuve d'Ascq Cendex, France*

a) ✉ *blazhynska@gmail.com*   *https://orcid.org/0000-0003-0749-8772*
b) ✉ *a.v.kyrychenko@karazin.ua*   *https://orcid.org/0000-0002-6223-0990*
c) ✉ *d.s.stepaniuk@gmail.com*   *https://orcid.org/0000-0002-2629-0427*
d) ✉ *oleksandr.korsun@gmail.com*   *https://orcid.org/0000-0003-0792-2342*
e) ✉ *kovalenko.sergiy.m@gmail.com*   *https://orcid.org/0000-0003-2222-8180*
f) ✉ *vivanov@karazin.ua*   *https://orcid.org/0000-0003-2297-9048*
g) ✉ *francois-alexandre.miannay@univ-lille.fr*   *https://orcid.org/0000-0003-1131-8287*
h) ✉ *abdenacer.idrissi@univ-lille.fr*   *https://orcid.org/0000-0002-6924-6434*
i) ✉ *onkalugin@gmail.com*   *https://orcid.org/0000-0003-3273-9259*

Titanium dioxide (TiO_2) is one of the most widely used nanomaterials in many emerging areas of material science, including solar energy harvesting and biomedical implanting. In this review, we present progress and recent achievements in the theory and computer simulations of the physicochemical properties of small TiO_2 clusters, middle-size nanoparticles, as well as the liquid-solid interface. The historical overview and the development of empirical force fields for classical molecular dynamics (MD) of various TiO_2 polymorphs, such as rutile, anatase, and brookite, are given. The adsorption behavior of solvent molecules, ions, small organic ligands, and biomacromolecules on TiO_2 interfaces are examined with the aim of the understanding of driving forces and mechanisms, which govern binding and recognition between adsorbate and surfaces. The effects of crystal forms, crystallographic planes, surface defects, and solvent environments on the adsorption process are discussed. Structural details and dynamics of adsorption phenomena, occurring at liquid-solid interfaces, are overviewed starting from early empirical potential models up to recent reactive ReaxFF MD simulations, capable of capturing dissociative adsorption of water molecules. The performance of different theoretical methods, ranged from quantum mechanical (QM) calculations (*ab initio* and the density functional theory) up to classical force field and hybrid MM/QM simulations, is critically analyzed. In addition, the recent progress in computational chemistry of light-induced electronic processes, underlying the structure, dynamics, and functioning of molecular and hybrid materials is discussed with the focus on the solar energy applications in dye-sensitized solar cells (DSSC), which are currently under development. Besides, dye design principles, the role of anchoring moiety and dye aggregation in the DSSC performance are crucially analyzed. Finally, we outline the perspectives and challenges for further progress in research and promising directions in the development of accurate computational tools for modeling interactions between inorganic materials with not perfect structures and natural biomacromolecules at physiological conditions.

Keywords: titanium dioxide, rutile, anatase, brookite, dye sensitization, nanoparticle, liquid-solid interface, molecular dynamics simulations, *ab initio* molecular dynamics.

Introduction

Nanocrystalline titanium dioxide (TiO_2) is one of the most widely used nanomaterials because of its chemical stability and environmental compatibility. In addition to many traditional applications in pigment chemistry, metallurgy, and catalysis, nano-sized TiO_2 has become a very appealing material for novel emerging areas of material science, including solar energy harvesting and hydrogen generation from water through photochemical reactions [1-2]. The performance of these applications depends critically upon size, shape, crystallinity, and morphology of TiO_2 nanomaterials.

TiO_2 exists in various polymorphs, such as rutile, anatase, brookite, and other rare phases (Fig. 1) [3]. Rutile and anatase have been widely used in the industry over the last decades [2,4]. Due to its large dielectric constant and its high reflectivity across the visible spectrum, rutile is commonly used in electronic devices, such as thin-film capacitors, interference filters, and optical waveguides. Anatase

is frequently used as a photocatalyst [1] because of its high photoreactivity in homogeneous and heterogeneous catalysis. Chemical reactions on TiO_2 surfaces play decisive roles in photocatalysis and photoconduction reactions.
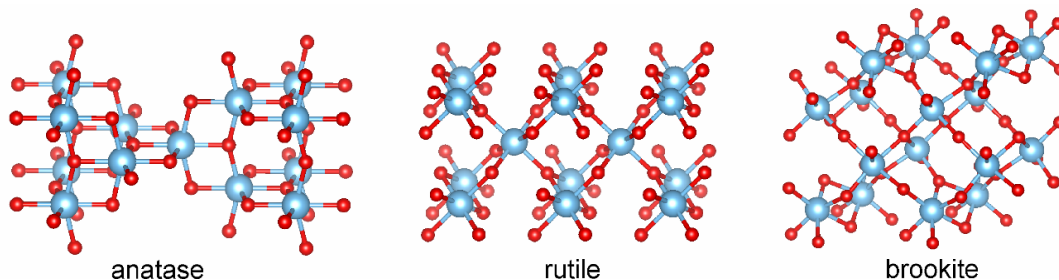
Figure 1. Crystallographic structure of anatase, rutile, and brookite TiO_2. Visualization and graphics were drawn with the VESTA program package [5].

One of the advantages of TiO_2 nanomaterials is their biocompatibility. Engineered TiO_2 nanostructures can exist in contact with human body tissue without causing an unacceptable degree of harm to the body [6]. Due to this unique capability, TiO_2 has emerged in many biomedical applications, such as artificial bones, joints and dental implants [7]. Therefore, significant experimental and computational efforts have been invested in studying phenomena occurring at the liquid-solid interface because their mechanisms and driving forces can point to new directions for biomaterial design and evaluation [8]. It has been shown that TiO_2 contributed to the development of a novel class of composite materials that physically integrates inorganic nanoparticles and biological molecules [9-10]. These hybrid conjugates can offer new opportunities for diverse applications in biosensing, site-selective recognition, and may potentially be incorporated into living organisms and biological cells [11]. Therefore, understanding protein adsorption on biomaterial surfaces is of great importance since, alongside water-surface interactions, it can significantly affect the performance of a biomaterial [10].

In this contribution, we discuss recent progress and achievements in the theory and computational modeling of TiO_2 nanomaterials and their applications across a wide range of research fields [12-13]. The effects of crystal morphology, crystallographic planes, surface defects, on the adsorption process are discussed. The role of the environmental effects, such as solvent, pH, and temperature, in the adsorption behavior of small organic ligands and biopolymers, is analyzed in detail. In addition, we overview the recent progress in classical MD simulations and some advanced MD sampling techniques, such as replica exchange and umbrella sampling, examining the energetics and dynamics of the interactions of single amino acids, small peptides, and proteins with TiO_2 surfaces [6]. Some quantitative insights into molecular recognition mechanisms between biopolymers and inorganic interfaces, including structure-function relationships are also considered. Particular focus is given to how MD simulations have contributed to our current understanding of peptide-surface adsorption at atomic detail. Finally, the perspectives, challenges, and promising directions in computational modeling interactions between inorganic materials and natural biomacromolecules are outlined.

Modeling of TiO_2 Surfaces and Aqueous Interfaces

The first empirical force-field (FF) for bulk TiO_2 was developed by Matsui and Akaogi (MA) [14] in 1991, in which the non-bonded interaction parameters between Ti and O were determined by reproducing the crystal structure of various polymorphic forms of TiO_2 (Fig. 1). In the MA force-field, the energetic interactions in TiO_2 were assumed to be completely non-covalent. The dispersion and repulsion interactions were represented by the Buckingham potential (1) (Table 1) [14]. The electrostatic contributions were treated with the pairwise additive Coulomb potential.

$$U_{LJ}\left(r_{ij}\right) = A_{ij} \cdot \exp\left(\frac{r_{ij}}{B_{ij}}\right) - \frac{C_{ij}}{r_{ij}^6} \tag{1}$$

The Buckingham potential parameters of the MA force-field were derived to reproduce the observed crystal structures, volume compressibilities, and thermal expansivities of rutile, anatase, and brookite, respectively. The effective partial charges at O and Ti atoms were assumed to be $q_O = -q_{Ti}/2$, where $q_O = -1.098$ and $q_{Ti} = +2.196$, respectively. Since the development, the MA force-field has become a paradigm for modeling of a broad range of TiO_2 nanomaterials [15-25].

Table 1. Parameters of the Buckingham potential suitable for modeling of TiO$_2$ polymorphs [14].

ion-ion	A_{ij} (kcal/mol)	B_{ij} (Å)	C_{ij} (kcal·Å^6·mol^{-1})
Ti-Ti	7.177×10^5	0.154	1.210×10^2
Ti-O	3.911×10^5	0.194	2.904×10^2
O-O	2.717×10^5	0.234	6.969×10^2

In succeeding years, the MA force-field has been used as an initial guess for further extension and the development of more complex computational models, suitable for simulations of TiO$_2$ surfaces, interfaces, nanoparticles and small clusters [26-27]. The first attempt to follow this approach has been performed by Bandura *et al.* [28-29] by using periodic density functional theory (DFT) calculations to derive new empirical FF parameters for modeling the TiO$_2$ (110) surface. A primary interest in modeling and simulations of TiO$_2$ interfaces was focused on studying of adsorption of biological molecules, especially peptides and proteins [30-31].

Because the most experimental studies were conducted in aqueous solution, it was vital that the adsorption interactions between TiO$_2$ and water molecules were adequately described. Since then, numerous MD simulations have been focused on modeling TiO$_2$-water interfaces [32-35].

The adsorption behavior and the interfacial structure of water molecules on the uncharged and negatively charged rutile (110) surface were studied by classical MD simulations at 298 K and 1 atm. [32-33]. The original interaction parameters of the MA force-field for TiO$_2$ were further adjusted by *ab initio* calculations of relaxed structures, and charges of the ideal rutile (110) surface. As a result, new modified interaction parameters were suggested for interfacial and deeper layers of TiO$_2$ atoms. Water molecules were treated with the SPC/E water model [36]. Therefore, the interactions between Ti atoms and the oxygen atoms of water molecules (Ti-O$_{H2O}$) were optimized by *ab initio* structure optimization and are described by a Buckingham potential (1). It was found that the positions of water molecules at the interface were found to be above each terminal titanium atom. A single additional layer of adsorbed water molecules occupies distinct sites related to the underlying crystal surface structure [32]. The water structure and mobility quickly decay to the bulk liquid properties beyond the second water layer. It was concluded that the influence of the interface for all simulated physico-chemical properties, including spatial orientation and diffusivity of water molecules, is negligible beyond distances of about 15 Å from the surface [32].

Starting from the interatomic potentials proposed by Bandura and Kubicki [28], Alimohammadi and Fichthorn [34] have developed a new set of FF parameters for modeling the interaction of water molecules adsorbed either molecularly or dissociatively onto the TiO$_2$ surface. The proposed FF was validated by computing binding energies and conformations for molecular adsorption of water molecules on the (101) and (112) surfaces of anatase, and the (110) surface of rutile. Moreover, the dissociative adsorption on water molecules onto the bulk-terminated (001) surface of anatase and the (110) surface of rutile was considered for various water surface coverages. The MD simulation results were found to be in good agreement with those of first-principles DFT calculations and experimental observations [34].
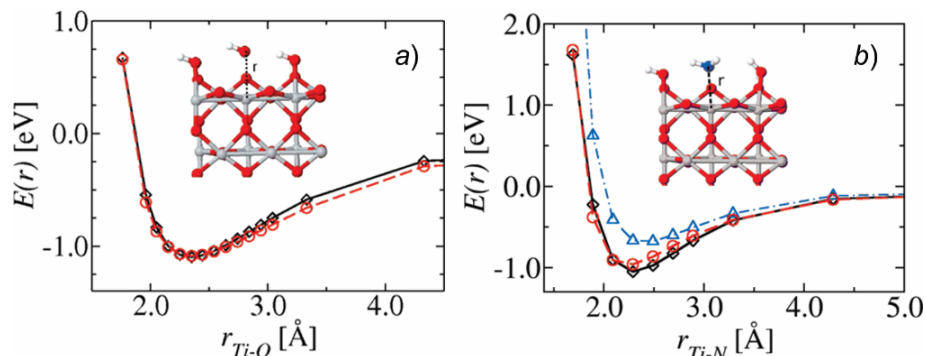
Figure 2. Potential energy surfaces of a water molecule (*a*) and an ammonia molecule (*b*) at various separations from the TiO$_2$ rutile(110) surface: DFT (black diamonds, ◊) and classical MD calculations (red circles, ○). The corresponding structure is displayed in the inset. Adapted with permission from [37]. Copyright © 2011, American Chemical Society.

Schneider and Ciacchi have performed a robust computational procedure of the development and validation of empirical potentials for classical MD simulations of the Ti/TiO$_x$/water interface employing *ab initio* MD simulations [37]. The procedure was based on the mapping of the adsorption energy profile of a single water molecule on the rutile TiO$_2$ (110) surface with Coulomb and Lennard-Jones potentials (Fig. 2). The following LJ parameters were suggested: σ(Ti)=0.07827 nm, σ(O)=0.1615 nm and ε(Ti)=1.402557 kJ/mol and ε(O)=1.91151 kJ/mol, respectively. The proposed FF was then validated over a representative series of small organic molecules, such as CH$_3$OH, CH$_3$NH$_2$, HCOOH, as well as the tripeptide Arg-Gly-Asp (RGD) adsorbed onto the oxidized Ti surface [37].
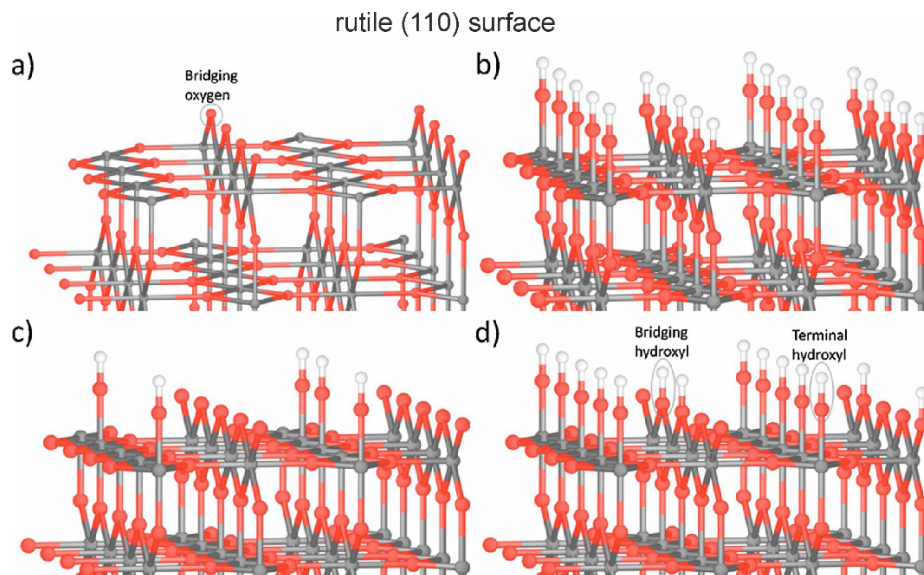
Figure 3. Scheme of rutile (110) surface: a) non-hydroxylated surface, b) fully hydroxylated surface showing the bridging and terminal hydroxyl groups, c) the surface partially covered by terminal hydroxyl groups, d) the surface covered completely by terminal hydroxyl groups and partially covered of bridging hydroxyl groups. Adapted from with permission from [32]. Copyright © 2004, American Chemical Society.

Skelton and Walsh have studied the interactions of liquid water and dissolved Na$^+$ and Cl$^-$ ions with the non-hydroxylated and hydroxylated rutile (110) surface (Fig. 3) by using a modified TIP3P water model, which is compatible with the CHARMM FF [38]. Moreover, further extension of the original MA FF has been released by MD simulations of the adsorption of water molecules onto different surfaces of TiO$_2$, such rutile (110, 100, 101, 001) and anatase (101, 001), in which water molecules were represented with a flexible SPC model. A primary goal of this study was focused on studying the structure, ordering, and orientation of water molecules located in the first and second interfacial layers [39-41].
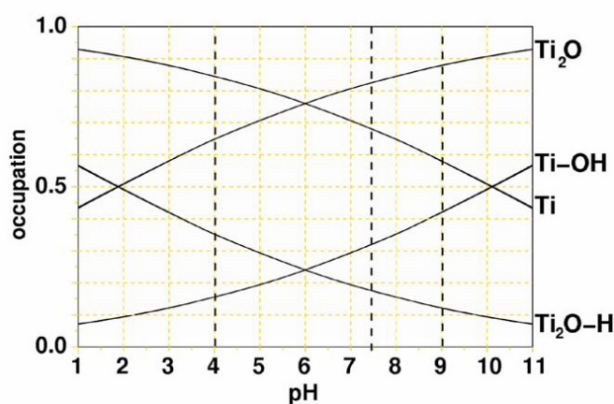
Figure 4. Occupation of surface adsorption sites: Ti$_2$O un-protonated, Ti$_2$O–H protonated bridging O atoms, Ti non-hydroxylated, Ti–OH hydroxylated surface Ti atoms. Adapted from [42]. Copyright © 2006 Elsevier B.V. All rights reserved.

In 2006, Köppen and Langel developed a new set of empirical FF parameters, suitable for modeling of the interfacial phenomena occurring at the rutile (100) surface in contact with NaCl aqueous solutions by using a two-particle interaction model with the Morse potential and Coulombic interactions [42]. Their FF model was able to mimic acid-base properties, such as the protonation and hydroxylation equilibriums of the TiO_2 interface, which could be adjusted to specific pH values (4, 7.4, and 9). Interfacial pH changes were mimicked by varying a ratio of protonated and hydroxylated residues at the interface, according to Fig. 4. The primary focus of their study was on validation of the Stern model by confirming of a dense layer of counterions on the charged TiO_2 surface and a diffuse layer propagated into the bulk water [42].

Conventional MD simulations of the TiO_2 interface are able to sample statistical mechanical ensembles with a fixed surface composition, which are well described by classical non-bonded interactions or fixed valence FF models. In classical MD simulations, an initially assigned protonation state of the TiO_2 interfacial atoms can not be altered during the simulation, which imposes some limitations for modeling the acid-base interfacial phenomena. One of the promising approaches, overcoming these restrictions, has recently been proposed by the development of a new ReaxFF reactive FF [43], capable of modeling chemosorption reactions in the Ti−O−H system [44-46]. The ReaxFF force field parameters have been fitted to a quantum mechanical (QM) structures and energies related to bond dissociation energies, angle, and dihedral distortions. Fig. 5 shows snapshots of the rutile (110) surface with layers of water molecules [46]. Moreover, reactions between water and TiO_2, as well as experimental crystal structures, heats of formation, and bulk modulus data were also compared. The authors demonstrated that the results of the ReaxFF calculations match reasonably well with those of DFT results for water binding energies, surface energies, and H_2O dissociation energy barriers [46]. The agreement between the DFT/MD simulation and ReaxFF simulations of water dissociation levels was reported to be within a 10% error [44,46].
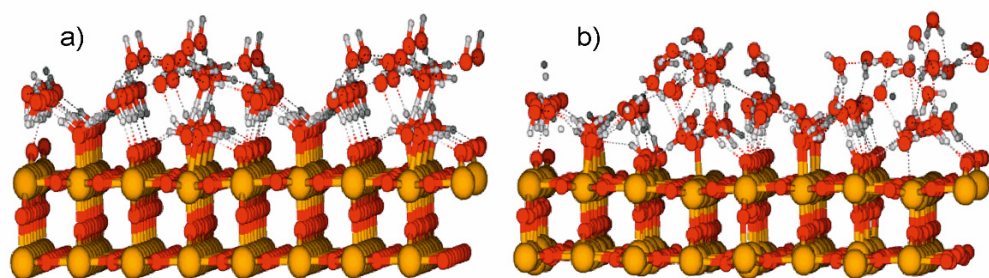
Figure 5. ReaxFF MD simulations of the amount of water dissociated on the 3 layers of the rutile (110) surface taken at the beginning (*a*) and the end (*b*) of the sampling. Adapted with permission from [46]. Copyright © 2013, American Chemical Society.

One of fundamental simplification of classical MD simulations of the water-TiO_2 interfaces is that a site charge located at each Ti and O atom kept fixed during modeling so that the variations of the surface dipoles in TiO_2 induced by water and the dipole moments of water molecules near the TiO_2 surfaces are not taken into consideration. Recently, a novel polarizable FF for water/rutile interfaces was developed [47]. This polarizable model takes into account the effect of the surface polarity induced by liquid−solid interactions explicitly. The model represents some extension of the charge response kernel (CRK) method [48-50] for molecules to solid surfaces by introducing the surface CRK (SCRK) (Fig. 6*a-b*), in which the CRK parameters were systematically derived by the first-principles calculations in the TiO_2 slab with the dipole-correction method.

The proposed polarizable FF was validated for the water/clean rutile TiO_2(110) interface (Fig. 6*c*). Good agreement was observed between structures and induced charges of a single water molecule, adsorbed onto the TiO_2 surface, obtained by the polarizable FF and those predicted by the first-principles calculations [50-51]. In addition, MD simulations of the liquid water/TiO_2 interface were benchmarked over stable structures of water adsorbed onto the TiO_2 surface, indicating that the dipole moments of water and TiO_2 induced by the water−TiO_2 interactions have a significant impact on the structure and dynamics of the water/TiO_2 interface [47,52].
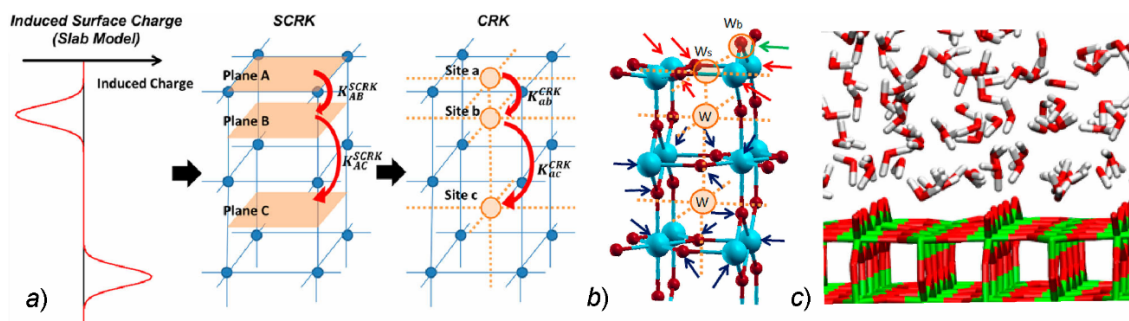
Figure 6. (*a*) Calculation scheme for the SCRK and CRK for the solid surfaces. (*b*) Schematic representation of the CRK sites. Ti and O atoms are represented by *sky blue* and *dark red* balls, while the CRK sites are represented by *orange* circles. (*c*) A snapshot of the water/clean rutile $TiO_2(110)$ interface. Adapted with permission from [47]. Copyright © 2013, American Chemical Society. (For interpretation of the references to color in this figure legend, the reader is referred to the Web version of this article.)

It should be noted that the numerous studies of the absorption behavior and the structure of water layers at water/TiO_2 interfaces have many similar features with computational studies of other liquid/solid interfaces [53]. To identify interface criteria, it would be instructive to apply a concept of the "10-90 width", which is defined as the distance from the solid surface over which a specific interfacial order parameter changes from 10% to 90% of the bulk value [53]. This concept was successfully utilized in MD simulations of the basal and prism interfaces formed by ice 1h and water molecules, approximated with the rigid SPC/E model [54]. The use of this concept by analyzing of the translational and window average-density order parameters allowed the authors to show that the interfaces consist of a series of relaxed double layers, which differ in diffusion coefficients and bond arrangement. The thickness of the interfaces was found to be 0.9-1.1 nm, which was consistent with ellipsometry measurements [54]. Importance of the "10-90 width" concept was recently highlighted for the proper setup of *ab initio*/DFT MD simulations of water/ice interfaces, for which a relatively large size of ~1.1 nm of water interface should be utilized [55].

It has long been recognized that the structure of water molecules confined into nano-sized volumes differs significantly from that of bulk water. In ref [56], MD simulations of the SPC/E water molecules, confined in TiO_2-rutile pores of diameters 1.3, 2.8, and 5.1 nm, were carried out at various water contents. It has been found that the proximity to the interface affects density and diffusivity of water molecules within a distance of around 10 Å from the walls, beyond which all structural and dynamics properties tend to converge [56].

To understand the difference between polar TiO_2 and hydrophobic graphite surfaces, the microstructure of water molecules absorbed at the nano-slits of the rutile (110) surfaces with the separation distance ranging from 0.8 to 2.0 nm were analyzed by using MD simulations [57]. MD simulation results show that the residence time of water at a TiO_2 surface is considerably longer than that at the graphite surface. Besides, the bound water molecules at the TiO_2 surface and the hydrogen bond network reduce the diffusivity of water through the TiO_2 slits. These MD simulations show that the surface chemistry is crucial to the diffusion of water inside nanoscale pores as compared to geometric size effects [57]. To investigate the microstructure and lubrication of water molecules confined in TiO_2 nano-slits under shearing, a series of non-equilibrium MD simulations have also been carried out [58]. To shed light on the role of the confined water molecules on lubrication, the effects of varying slit gap widths (0.8, 1.2, 1.6, and 2.0 nm) and shear velocities (200, 100, 50, and 10 m/s) on the friction coefficients between TiO_2 and water molecules (SPC/E) were evaluated. It has been shown that the friction coefficient decreased as the slit width increased. The detailed analysis of the microstructure of water layers revealed that water molecules confined in the slits were ordered up to two interfacial layers [58].

Using MD simulations with the LAMMPS package, the static and dynamic properties of water on TiO_2 nanotubes (TiO_2-NTs) with a diameter of ~1.0 nm (Fig. 7*a-b*) were studied [59]. The MA forcefield was used for TiO_2, whereas the SPC/E model was utilized for water. The MD simulation results showed that the water molecules outside TiO_2-NT conform to the two-layer model for water, which is typical for water adsorbed onto a planar surface. The difference was that the first water layer was further affected by the surface curvature, indicating the more facile water desorption from the surface.

This layer disappears for water inside TiO_2-NT, leaving a water layer with the hydrogen atoms pointing to the oxygen atom O_{2c} to form hydrogen bonds (Fig. 7*c-d*) [59].

The mechanical behavior of anatase TiO_2 nanotubes in axial loading was examined by using MD simulations with the MA force-field [60]. The nanotubes of different radii and lengths were modeled at 300 K and subjected to both stretching and compression. The MD simulations demonstrated that, as the radius of the nanotubes increases, their surface was wrinkled axially, which in turn caused their axial behavior to change dramatically. The threshold radius was observed to be 50 Å for a length of 300 Å [60].
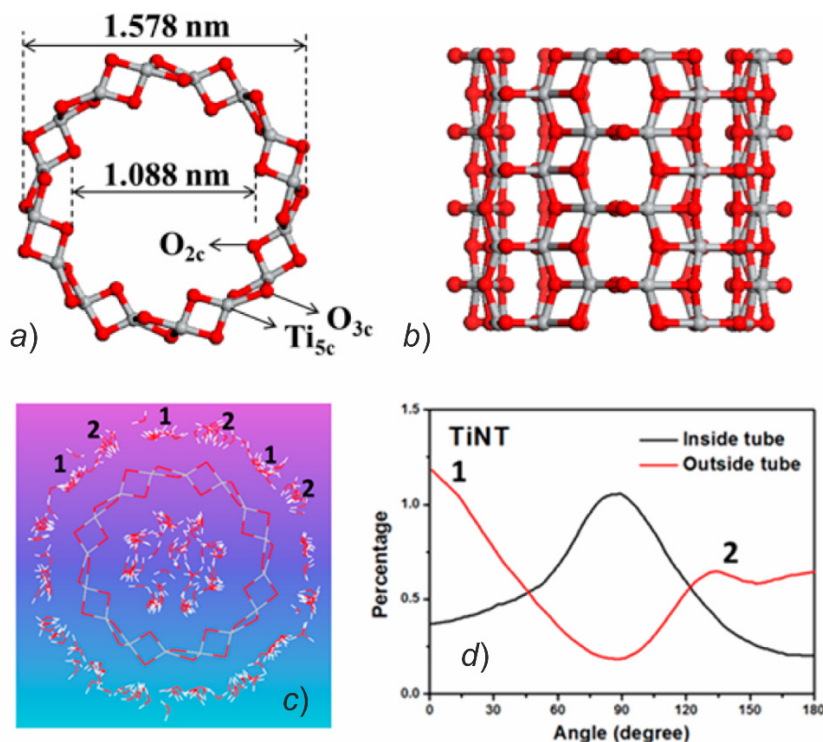
Figure 7. (*a*) Atomic structure of TiO_2-NT viewed along the axial direction. (*b*) Side view of TiO_2-NT. (*c*) Snapshots of the equilibrium structure of a water−NT system (along the axial direction). (*d*) Distribution of the angle of the water molecules' dipole vectors along the radial direction of NT (point from the tube center to the tube wall). Adapted with permission from [59]. Copyright © 2016, American Chemical Society.

The phase behavior of the *n*-octacosane (*n*-C_{28})−water mixture inside TiO_2 nanopores was considered with classical MD simulations [61]. Three model systems having different TiO_2 (101) anatase pore sizes of 34, 40, and 55 Å were examined (Fig. 8*a* and 8*c*). TiO_2 atoms were modeled as Lennard-Jones spheres with $\sigma(Ti)$=0.092 nm, $\sigma(O)$=0.303 nm and $\varepsilon(Ti)$=0.17138 kJ/mol and $\varepsilon(O)$=0.5016 kJ/mol as taken from [62]. Water molecules were treated with the SPC/E model, whereas the united-atom TraPPE (transferable potential for phase equilibria) FF was used for *n*-C_{28}. The standard Lorentz−Berthelot combining rules were used for calculations of nonbonded Lennard-Jones interactions between sites of a different type. It was found that even though phase segregated mixtures retained their structural properties, as compared to their bulk counterparts, some significant deviations were observed in the density profiles inside the nanopore (Fig. 8*b* and 8*d*). Water molecules were organized into two discrete layers on the TiO_2 surface so that *n*-C_{28} was shielded from the nanopore walls (Fig. 8*d*). It was suggested that octacosane's self-diffusion was influenced only slightly by confinement. However, water molecules were severely hindered by the TiO_2 nanopore surface. Similarly to other studies, it was found that water diffusivity revealed a strong dependence on the distance from the nanopore center [61].

Recently, the MA force-field has been utilized as the initial guess for the development of interatomic potentials for modeling the deposition of calcium and phosphate species (calcium phosphate, $Ca_3(PO_4)_2$) on the anatase TiO_2 (101) and (100) surfaces, respectively [63]. The authors have parameterized the missing two-body interactions between Ca^{2+}, PO_4^{3-} and TiO_2, and performed classical MD simulations of the deposition of calcium phosphate on the anatase surface in aqueous solution, which

were further benchmarked over DFT results. The comparison between the DFT and MD simulations results have shown the outstanding performance of the new set of FF parameters in describing the adsorption of $Ca_3(PO_4)_2$ on the most stable (101) surface of anatase [63].
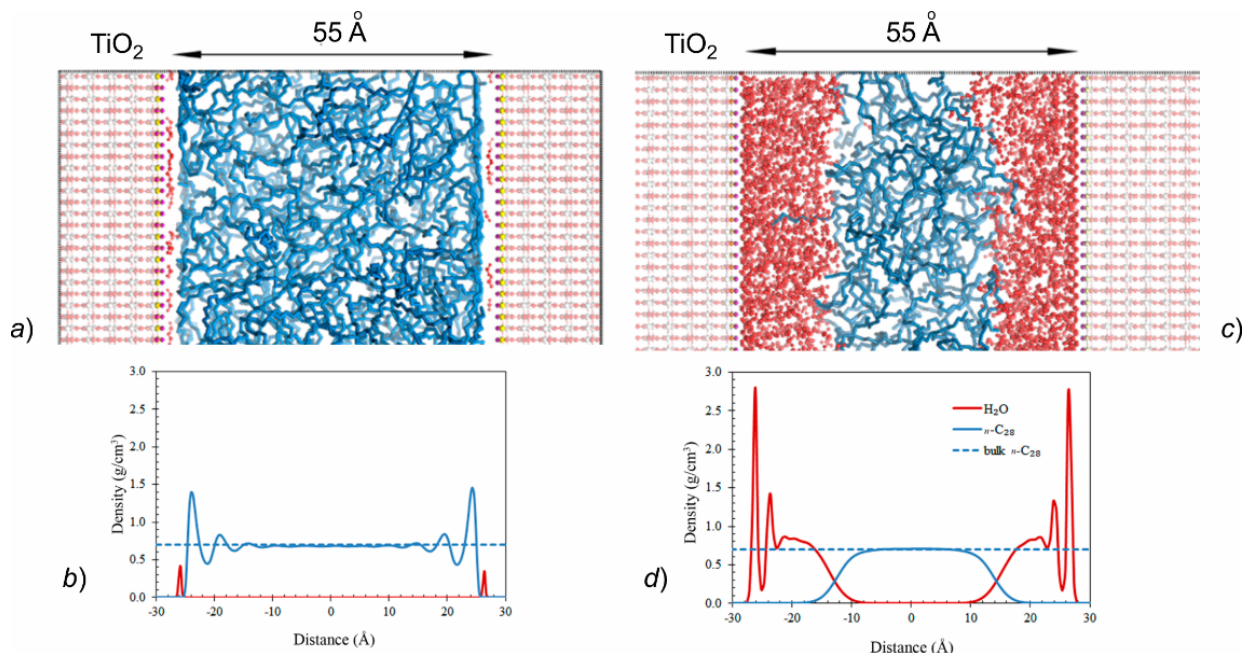
Figure 8. Final MD configuration of n-C_{28}−H_2O mixture taken at 473 K and the corresponding density profile of water and n-C_{28} in the z-direction: (*a*) $\chi(H_2O)$=0.20 and (*c*) $\chi(H_2O)$=0.9655 confined in the TiO_2 55 Å diameter pore. Adapted with permission from [61]. Copyright © 2016, American Chemical Society.

New insights on the molecular processes in the initial nucleation of $Ca_3(PO_4)_2$ on the rutile TiO_2 surfaces were obtained by using classical (MD) simulations [64]. Five kinds of TiO_2 substrates were considered: nonhydroxylated and fully hydroxylated perfect TiO_2 surfaces, and the stepped-, grooved-, and ridged-structured TiO_2 surfaces with full surface hydroxylation. The FF parameters for the surface hydroxyls were obtained from Předota's work [32]. The FF interaction parameters between $Ca_3(PO_4)_2$ and TiO_2 were previously derived from the *ab initio* calculations [65]. The MD simulation results suggested that the surface hydroxylation and the shape and the structure of the TiO_2 substrate contributed significantly to the initial nucleation of calcium phosphate. Surface hydroxyls on TiO_2 provided active sites for the aggregation of calcium phosphate. Both Ca^{2+} and PO_4^{3-} ions were able to bind to the hydroxylated TiO_2 surface directly or indirectly via the first water layer (Fig. 9*a-b*). Surface nano-topographies (e.g., grooves or ridges) were able to restrict the diffusion of Ca^{2+} and PO_4^{3-} ions (Fig. 9*c*) [64].
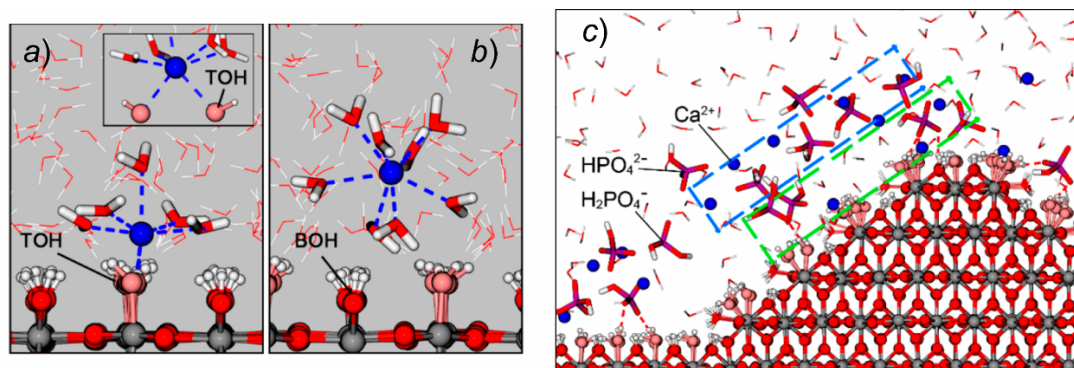
Figure 9. MD snapshots of Ca^{2+} onto the rutile TiO_2 (110) surface shown in the direct adsorption conformations (*a*) and the hydrated adsorption conformations (*b*). Adsorption conformation of calcium phosphate ions on the ridge-structured TiO_2 surface (*c*). Adapted with permission from [64]. Copyright © 2018, American Chemical Society.

Adsorption of small additives onto TiO$_2$

Crystal growth and morphology of crystalline TiO$_2$ are governed by adsorption of small organic additives. These parameters are also essential for the development of novel functional materials. Therefore, MD simulations of the binding modes and thermodynamically stable conformations of small ligands at the surfaces of TiO$_2$ crystals have become attractive tools for understanding the mechanisms underlying additive-surface interactions. As results, numerous computational studied have been devoted to examining the adsorption behavior of small organic compounds, such as ammonium [66], methane [67], methanol [66], formic acid [67], benzene [66-67], and dimethyl methylphosphonate [68], on TiO$_2$ surfaces. Adsorption of a rhodamine dye [69] and some biologically-relevant molecules, such as phospholipids (DOPC, DOPS, and DMTAP) [70], onto TiO$_2$ was also examined.

Recently, the use of the electronic continuum correction (ECC) theory, which suggests some adjustment of point charges at Ti and O atoms to reproduce the adsorption phenomena occurring at the TiO$_2$−liquid interface, has received significant attention [32-33,71-75]. MD simulations, augmented by free energy calculations and supported by *ab initio* calculations, were used to study the adsorption of oxalic acid ions (oxalate and hydrogen oxalate) on the rutile (110) surface [76-77]. The predicted adsorption on perfect non-hydroxylated and hydroxylated surfaces (Fig. 3) was found in agreement with experimental adsorption data and predictions of the charge-distribution multisite ion complexation model [76]. The most favorable surface species were identified to be outer-sphere complexes because of the strong hydrogen bonding of oxalic acid ions with surface hydroxyls and adsorbed water molecules [76]. Moreover, MD simulations were performed to identify the thermodynamically stable conformations of glycolate (CH$_2$(OH)COO$^-$), lactate, and 2-hydroxybutyrate ions (Fig. 10) at the (001) and (110) planes of rutile crystals by using the MA force field [78-79]. The MD results suggested that, for both planes, the conformation and dynamics of the glycolate ion were strongly dominated by a layered structure of water on the surface. It was found that the glycolate ion was bound to the surface more stably on the (110) plane than on the (001) plane [78]. Besides, the bound conformation in which the COO$^-$ group was oriented toward the rutile surface was found to be the most stable for the lactate and 2-hydroxybutyrate ions. In contrast, a conformation, in which the COO$^-$ group was oriented toward bulk water, was found to be the most stable for the glycolate ion [79].

glycolate ion   lactate ion   2-hydroxybutyrate ion
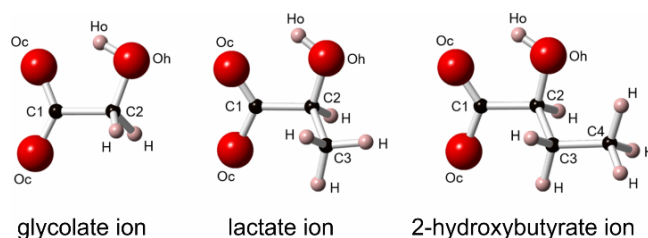
Figure 10. Minimum-energy structures of the glycolate, lactate, and 2-hydroxybutyrate ions. Adapted with permission from [79]. Copyright © 2019, American Chemical Society.

The adsorption process of a nanodroplet of cysteine molecules onto a perfect and the defective rutile (110) surface was simulated in the gas phase using classical MD approaches, based on reactive and nonreactive FF parameterizations [44]. Three molecular forms of cysteine species, namely, one neutral and two zwitterionic ones, were considered. It has been shown that the adsorption of cysteine molecules on perfect and defective rutile surfaces indicates that both of the computational approaches are able to recognize the importance of the sulfur atom in the binding process. However, it was also pointed out that only through a reactive FF description, the protonation state of cysteine at the interfaces produced by environmental effects could be correctly identified [44].

Interaction of biomacromolecules with TiO$_2$ surfaces

Understanding the interaction mechanism between metal and metal oxide surfaces and biomolecules, such as proteins/peptides/aminoacids, is crucial to the successful usage of hybrid biomaterials in complex physiological environments [13,15,80-81]. Therefore, the development of theory and computational approaches for modeling organic/inorganic interfaces may accelerate the development of novel biomaterials [10,81-83].

The MA force-field has attracted essential interest in MD simulations TiO$_2$ nanomaterials: however, its applicability for nano-bio MD simulations remains limited because of its discrepancy with the standard force fields for biomolecular simulations already available in the literature (e.g., AMBER, CHARMM, OPLS). So, some long-standing problems of accurate sampling of biomolecules near inorganic surfaces and calculation of binding free energies of amino acid side chain analogs and a peptide to the TiO$_2$ surface require the development of the compatible FF parameters. To accomplish this goal, Brandt and Lyubartsev [84] developed bonded and non-bonded interaction parameters for classical MD simulations of TiO$_2$ surfaces in contact with aqueous media (including biomatter) (Fig. 11a).

The proposed FF was designed in agreement with the following criteria: (1) compatibility with standard FFs for biomolecular simulations; (2) transferability of TiO$_2$ interactions to a wide variety of biomolecules: proteins, lipids, and nucleic acids so that Lennard-Jones nonbonded interactions with new molecules could be estimated by standard combination rules; (3) the force field should reproduce interactions at biologically relevant conditions, such as room temperature and atmospheric pressure; (4) the FF parameters were derived in a thermodynamically consistent manner from known experimental data. The modeling was performed by quantum mechanical geometry optimizations of water on TiO$_2$ surfaces using density functional theory using the Perdew−Wang exchange-correlation functional and ultrasoft pseudopotentials (Fig. 11b). A bonded TiO$_2$−surface model was developed based on these optimized geometries [84]. The performance of the proposed bonded TiO$_2$ FF was validated by calculations of adsorption profiles and adsorption free energies for the side chain analogs of the 20 naturally occurring amino acids and a titanium binding peptide on the TiO$_2$ (100) surface [85]. Finally, adsorption simulations of a titanium binding RKLPDA-peptide were benchmarked to identify peptide binding modes on a TiO$_2$ (100) surface (Fig. 11c-d) [85].

The adsorption behavior of the four DNA bases (adenine, guanine, thymine, and cytosine) on a charged partially hydroxylated rutile (110) surface was studied through classical MD simulations [86]. The FF parameters reported by Predota et al. was used for the hydroxylated rutile (110) slab [32]. The AMBER FF was used for the DNA bases and the modified TIP3P FF for water [87].

To identify the best binding arrangement, and quantify the strength of their interactions with the inorganic surface, the potential of mean constrained force (PMF) was calculated. The general tendency was observed so that each DNA base adsorbed onto structured solvent layers, which were in direct contact with the TiO$_2$ substrate. Upon the surface binding, the DNA bases were located to be perpendicular to the slab without adopting a preferential orientation. The DNA base binding to the TiO$_2$ surface was rather weak, so that desorption back into the bulk solvent was observed [86].
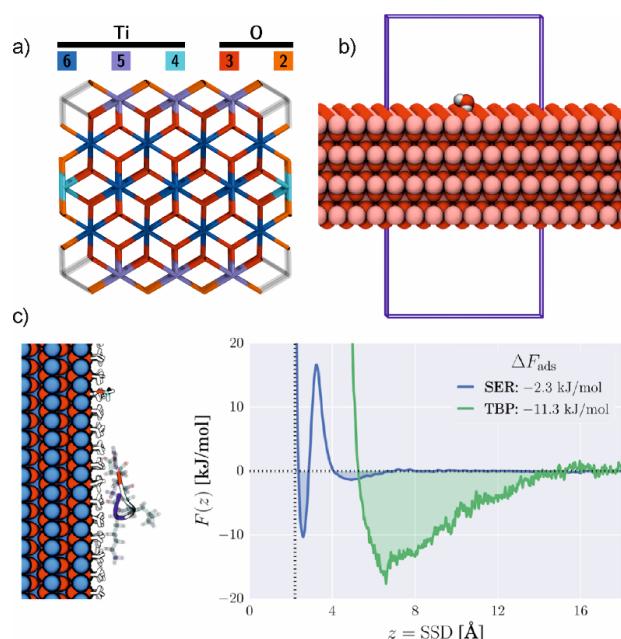
Figure 11. (a) The coordination number for Ti and O atoms. (b) Interface simulations of a (5×8) TiO$_2$ slab were used for calibration of TiO$_2$−water adsorption enthalpy. (c) Snapshot of a peptide on the TiO$_2$ (100) surface and an adsorption free energy profile calculated by MD simulations. Adapted with permission from [84-85]. Copyright © 2015, American Chemical Society.

Single amino acids or short peptides have been the first molecules to be computationally studied [13,80-81,88-89]. *Ab initio* periodic calculations and classical MD simulations were performed to investigate the adsorption mode, conformational characteristics, and inter-adsorbate interactions of alanine and several dipeptides, such as alanine-glutamic acid and alanine-lysine onto the TiO_2 (110) rutile surface [30,90].

Among the many possible peptides, the RGD (Arg-Gly-Asp) and RKLPDA sequences of amino acids are of great interest [6]. After the placement of a Ti implant inside the body, integrin receptors at the cell membrane will search for specific ligands on the surface for binding. If the ligand is present and its conformation on the surface is suitable, further interaction between the cell and the implant can occur. Protein ligands, such as fibronectin, vitronectin, and collagen, are present in the extracellular matrix (ECM). The cellular response induced by these extracellular matrix proteins, however, is mainly through the Arg-Gly-Asp (RGD) sequence (Fig. 12*a*) [91].

The adsorption of RGD-peptide onto the rutile TiO_2 (110) surface was modeled by using the MA force-field for TiO_2 and TIP3P for waters [92-93]. It was found that RGD-peptide was able to adsorb rapidly on the surfaces by amino groups NH_2 and NH_3^+, and the carboxyl group COO^- could edge out the adsorbed water molecules and bond to the surface titanium atom (Fig. 12*b*).
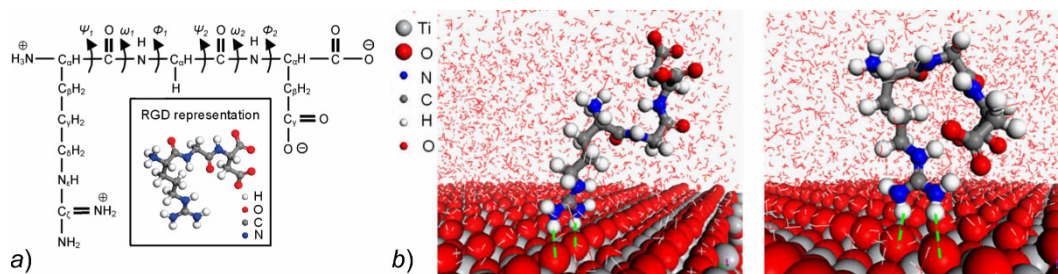
Figure 12. (*a*) RGD-peptide (Arg-Gly-Asp). (*b*) Snapshots of a conformation of RGD-peptide adsorbed on the perfect TiO_2 (110) in at 2.0 ns and 4.0 ns, respectively. Adapted with permission from [92-93]. Copyright © 2010, American Chemical Society.

Since earlier computational studies [93], RGD-peptide has become a benchmark system for the understanding of the origin and molecular mechanism of the molecular recognition between proteins and peptides, and the TiO_2-aqueous interface [37,65,94-99]. While the physicochemical aspects of the adsorption of RGD-peptide onto TiO_2 surfaces were studied in detail, the mechanism by which other peptides adsorb to titanium surfaces is not yet fully understood [65,100-103].

Two experimentally identified 12-mer peptide sequences referred to as the titania-binding peptides Ti-1 (QPYLFATDSLIK) and Ti-2 (GHTHYHAVRTQT) [88,100] revealed the unusual adsorption affinity to for titania that efficiently promote titania mineralization from an aqueous titanium bisammonium lactatodihydroxide (TiBALDH) solution [104]. Influences of Ca^{2+} ions at the aqueous TiO_2 interface on the binding modes of Ti-1 and Ti-2 peptides was investigated using replica exchange MD simulations combined with solute tempering MD simulations [105]. It was observed that for Ti-1, Ca^{2+} ions enhanced the adsorption of the negatively charged Asp8 residue in this sequence to the negatively charged surface, via Asp–Ca^{2+}–TiO_2 bridging. However, for Ti-2, fewer residues were predicted to adsorb directly to the surface in the presence of Ca^{2+}, possibly due to competition between the other peptide residues and Ca^{2+} ions to adsorb to the surface [105]. Recently, a new Ti-binding peptide of 13 amino acids (AMRKLPDAPGMHC) was identified by using a series of multiple 300 ns MD samplings of adsorption dynamics of the peptide at the aqueous interface of a TiO_2 anatase surface, started from different peptide orientations with respect to the surface [106]. It was suggested that the peptide anchoring was mediated by the interfacial water layers by means of the charged groups of the side chains of the peptide [106].

Bone morphogenetic protein-2 (BMP-2), a dimeric cysteine knot protein, has therapeutic effects for ectopic bone [107]. Moreover, it plays a crucial role in osteoblast differentiation and proliferation [107]. Classical MD simulations and a hybrid approach of steered molecular dynamics (SMD) combined with MD simulations were employed to investigate the initial stages of the adsorption of BMP-2 upon approaching hydrophilic surfaces of rutile TiO_2 [62]. Surface adsorption was evaluated for six different orientations of the protein, two end-on, and four side-on, in an explicit water environment. It

was observed that BMP-2 adsorbed only loosely to the hydrophilic TiO_2 surface. Despite favorable interaction energy between BMP-2 and the TiO_2 surface, the rapid formation of a two-layer water structure prevented the direct interaction between protein and TiO_2. It was suggested that the first water adlayer had a strong repulsive effect on BMP-2, while the second attracted the protein toward the surface [62].

Adsorption orientation and conformation of myoglobin on perfect rutile (110) and (001) surfaces were investigated by combining Monte Carlo and MD simulations [108]. Myoglobin was modeled with the CHARMM27 FF, whereas the modified MA force-field [103] re-fitted to the Lennard-Jones potential, was utilized for rigid TiO_2 surfaces. It was found that the adsorbed myoglobin conformations were not influenced by the physicochemical properties of the rutile (110) and (001) surfaces (Fig. 13). These findings were understood in terms of the strong hydrophilicity of both surfaces. The adsorption behavior of myoglobin was governed by two layers of adsorbed water molecules formed on both rutile surfaces. After 80 ns MD simulation, the heme of myoglobin was found to be close to the rutile (001) surface and far away from the rutile (110) surface [108].
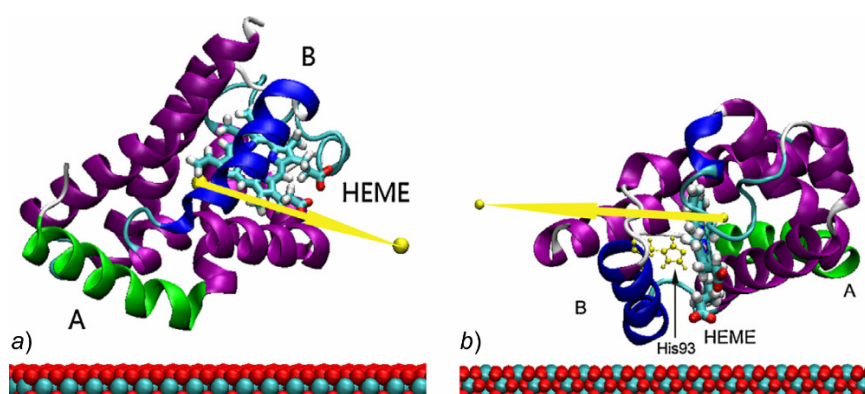
Figure 13. Final representative adsorption configurations of myoglobin (*a*) on rutile (110); (*b*) on rutile (001) after 80 ns MD simulations. The arrows indicate the dipole direction of myoglobin. Adapted from [108].

RNA aptamers with unique tertiary structure and high affinity for binding to a specific target with high affinity and specificity targets are used as therapeutic agents [109]. The adsorption behavior of an RNA aptamer with (101), (100) and (110) surfaces of TiO_2 anatase was investigated by using MD simulations [110]. Analysis of the structural parameters and interaction energies demonstrated that the (110) surface was energetically more favorable for the adsorption of the RNA aptamer than the (100) and (101) surfaces, respectively [110].

Collagen is the main structural protein in the extracellular matrix, which plays an important and irreplaceable role in biomineralization [111]. Collagen is used to modify biomaterial surfaces so that the pre-adsorbed collagen on TiO_2 could improve adhesion. It stimulates cell behaviors mainly through the amino acid sequence Arg–Gly–Asp interacting with the integrin at the cell membrane in cell adhesion. It is believed that the carboxyl groups in collagen play a key role in hydroxyapatite nucleation [112]. The adsorption of collagen on the perfect and grooved rutile (110) surface in aqueous solution was modeled by classical MD simulation [113-114]. Preferable binding modes were examined, including direct and indirect binding modes, in which the peptide interacted with the substrate surface directly or via the first layer water molecules (Fig. 14). The MD simulations suggested that the initial poses of collagen on the rutile surface could influence the final adsorption conformation of collagen. The reduced rutile surface provided active sites for collagen adsorption. It was concluded that the direct binding mode was responsible for the stable adsorption of collagen. The indirect binding mode might also play an important part at the initial adsorption stage, but itself alone could not 'trap' the collagen on the surface stably unless the direct binding mode had already been formed [113]. The nonspecific adsorption of noncollagenous bone matrix proteins (NCPs) onto a titania interface was examined for the case of the adsorption of the α-1 domain of osteocalcin [115].

Fibronectin (FN) is a major component of the extracellular matrix in tissue, which influences cell adhesion and migration through interactions with other extracellular components [116]. FN contains the important cell-binding sequence — arginine–glycine–aspartic acid (RGD), which can serve as a

primary attachment site for TiO_2. To investigate the topographical dependency of FN adsorption, MD simulations were employed to describe its adsorption behavior on nanostructured rutile (110) surfaces (Fig. 15) [117]. It was found that the residence time of adsorbed FN was relied on its binding mode (direct or indirect) with the substrate and the surface interior. In the direct binding mode, FN molecules were found to be 'trapped' at the anchoring sites of the rutile surface, or even penetrate deep into the interior of nanostructures, regardless of the initial configuration on the surface [117].
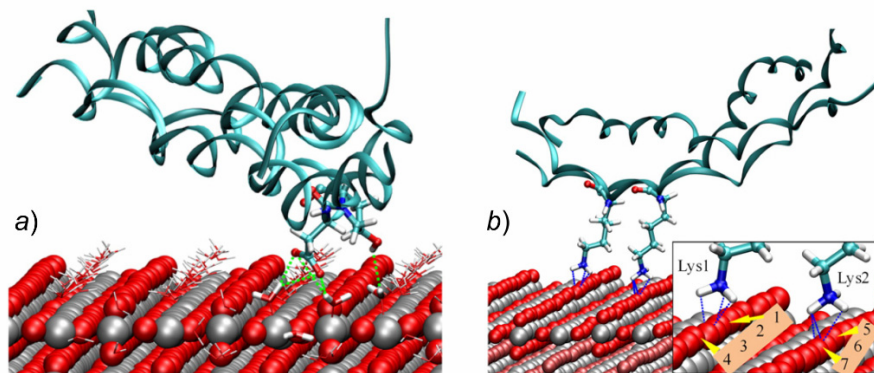
Figure 14. (*a*) MD snapshot of collagen interacted with the rutile surface via the water molecules near the surface. (*b*) Adsorption conformation of the collagen segment interacted with the rutile surface directly via the hydrogen bonds between Lys and the rutile oxygen atom. Inserts show the bridging atoms along the (001) directions interacted with the Lys residues, respectively. Adapted from [113]. Copyright © 2013 Elsevier B.V. All rights reserved.
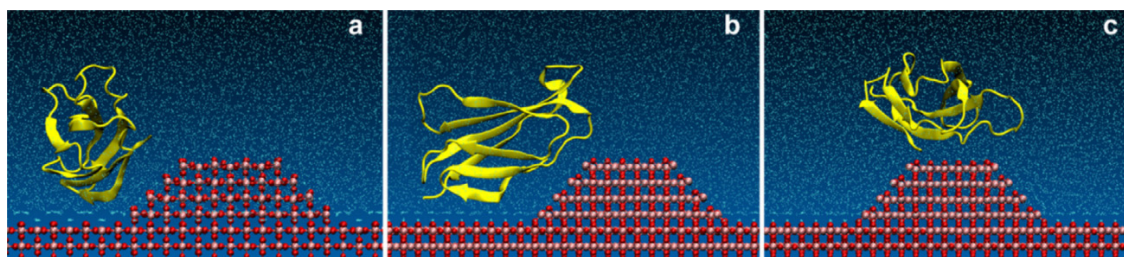
Figure 15. Initial configurations of fibronectin on the rutile (110) surface with a protrusion. Adapted from [117]. Copyright © 2016 Elsevier B.V. All rights reserved.

Interaction of polymers with TiO₂ surfaces

Passivation of metal and metal oxide nanoparticles by polymer coating is the conventional approach to improve their colloidal stability and biocompatibility [118-122].

MD simulations of the interface between poly(ethylene oxide) (PEO_{54}) and TiO_2 were performed at 423 K using a quantum chemistry-based FF [123]. A representative model system, used for the FF parameterization, consisted of a PEO monomer (dimethyl ether) complexed with the TiO_5H_9 cluster. It was found that the PEO density was significantly perturbed by TiO_2 surfaces so that layers of highly dense polymer were formed that persisted up to 15 Å from the surface. Conformational and structural relaxations of the interfacial PEO were found to be dramatically slower than those of bulk PEO. It was suggested that the surface structure and electrostatic interactions between PEO and TiO_2 governed the nature of PEO relaxation at the TiO_2 interface [123]. Adsorption of poly(3-hexylthiophene) on the nanostructured titania (110) rutile surface *in vacuo* was studied using MD simulations as a function of local surface curvature and roughness [124].

Coating of TiO_2 with polyethylene glycol (PEG) is particularly convenient because it is inexpensive, FDA-approved prevents opsonization from the immune system and therefore increases the in vivo circulation time [125-127]. In addition, it has been reported that poly(vinylpyrrolidone) (PVP) and PEG oligomers and may be used as co-adsorbents, which reduce electron recombination by the effective coverage of vacant sites on TiO_2 surfaces that improve the performance of dye-sensitized solar cells [128-129].

^{13}C NMR measurements combined with dispersion-corrected density functional theory (DFT-D2) calculations [130] and classical MD simulations were performed to determine the operating condition that guarantee very high grafting densities of PEG on amorphous TiO_2-NPs, which are desirable in any biomedical application [131]. For TiO_2, a simplified version of the MA FF model [132] was used, while as for water, the TIP3P model was utilized. Polyethylene PEG was described with Generalized Amber Force Field (GAFF). It was shown that classical and popular models of polymer conformation on surfaces failed in determining the mushroom-to-brush transition point and proved that it takes place only at a rather high grafting density value (Fig. 16) [131].
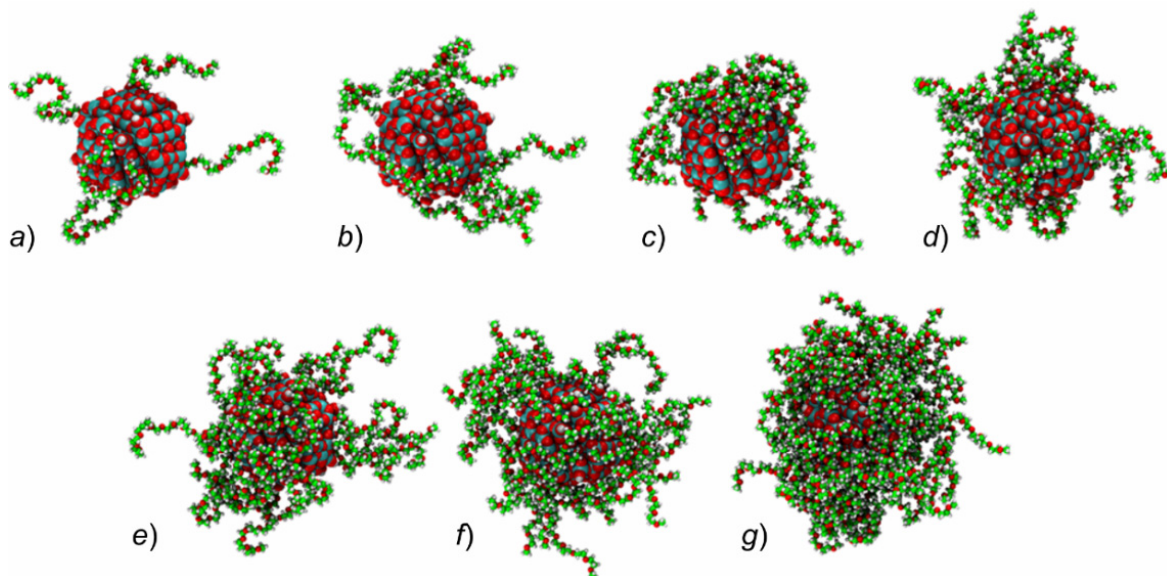
Figure 16. Final MD snapshots for the mPEG$_{500}$-TiO$_2$-NP systems at different coverages (σ in chain/nm^2) in water: (*a*) m=5, σ=0.255, (*b*) m=10, σ=0.440, (*c*) m=15, σ=0.676, (*d*) m=20, σ=0.901, (*e*) m=25, σ=1.126, (*f*) m=30, σ=1.351, (*g*) m=50, σ=2.252, respectively. Adapted from [131]. Copyright © 2019 American Chemical Society.

Modeling of TiO$_2$ in Non-Aqueous Environment

Chemisorption of solvent molecules and ligands onto the TiO_2 surface may strongly affect its electronic structure [133]. For these reasons, growing interest has been focused on modeling and simulation of TiO_2 in the non-aqueous environment [134-139].

Acetonitrile is commonly used as a polar organic solvent for Grätzel DSSCs. Schiffmann and co-workers have studied the structure and dynamics of the anatase(101)-acetonitrile interface by combined *ab initio* and classical MD simulations [134]. The CP2K simulation package and the Gaussian plane wave (GPW) approach were employed to derive the empirical FF for the TiO_2/acetonitrile interactions. A rigid slab of TiO_2 was modeled in contact with neat acetonitrile. It has been found that the strong dipolar interactions between acetonitrile molecules result in pronounced layering of adsorbed molecules propagated further away from the interface to bulk solvent up to seven distinct solvent layers (~12 Å). Each successive layer was characterized by an alternate orientation of the acetonitrile dipoles. Such capability of the solvent to make a strong interaction with the TiO_2 wall rather than with bulk solvent might have several significant practical effects, which, for instance, could lead to passivation of the solar cell surface [134].

Singh *et al.* examined the dynamics of ionic liquids (ILs) inside the nanopores of TiO_2 and suggested that the pore size plays a crucial role in the determination of the macroscopic electrical resistance of IL-bases DSSCs [135]. The object of their study was the interplay of the rutile wall, containing nanopores of various shapes, which were confined with 1-ethyl-3-methylimidazolium *bis*(trifluoromethylsulfonyl)imide [EMIM$^+$] [TFMSI$^-$]. The previously developed all-atom force field parameters [140] were used for modeling the cations [EMIM$^+$] and anions [TFMSI$^-$], respectively. The authors were able to identify major factors, which influence on the interaction TiO_2-IL: the IL density

inside the nanopores, distances of the ions to the pore walls, as well as the effective pore size, pore shape, surface roughness, and the surface density of electrical charges within the pore walls [135].

Recently, particular interest has been paid to studying the interaction mode between TiO_2 and various ILs at the molecular level [136]. Dai *et al.* studied the role of interfacial hydrogen bonding between the TiO_2 slits of different widths and ethylammoinium nitrate (EAN), determining the orientation of nanoconfined IL ions on the (100) rutile surface by combining of MD simulations and vibrational spectroscopy [137]. MD simulations were carried out with the NVT ensemble at T=353K by using the all-atom FF for the EAN IL, developed by Acevedo and Tirado-Rives [141]. It was found out that NH_3^+ is more likely to adsorb to the TiO_2 wall than NO_3^-. However, both NH_3^+ and NO_3^- tend to be closer to the surface than CH_3^+ ions, which could be explained by the hydrophilicity of the TiO_2 slit. Moreover, the orientation of IL ions was depended on the width of TiO_2, which significantly affects the microstructure of the EAN: the smaller is the TiO_2 wall, the stronger is hydrogen bonding of NH_3^+ with the TiO_2 surface that results in lying down of cations along the TiO_2 wall. The increase of the width of the slits leaded to decreasing of the hydrogen bond strength and proportion between IL and TiO_2 and, consequently, to the interfacial reorientation of IL ions [137].

Malali and Foroutan have studied the ionic liquid droplets containing 1-butyl-3-methylimidazolium and fluorophosphate on the rutile (110) surface by MD simulations [142]. Using the OPLS-AA FF customized for ionic liquids [141], it was found that the closest surrounding of IL to the nanosurface could be represented by two differently oriented layers of cations. The imidazolium rings are parallel to the surface in the first layer, and they tend to orient perpendicular to the surface in the second region. Such orientation creates some vacancies and empty spaces between these two layers, making the spherical shape gaps, which favors the IL becomes non-wetting at the upper layers of the droplets [142]. Consequently, such non-wetting behavior depends on the covering with a full layer of cations, but not on the density on the TiO_2 surface and this effect of the interaction energy of the substrate on ionic liquids leads to a circular configuration of ions in the center of the ionic liquid droplet (Fig. 17).
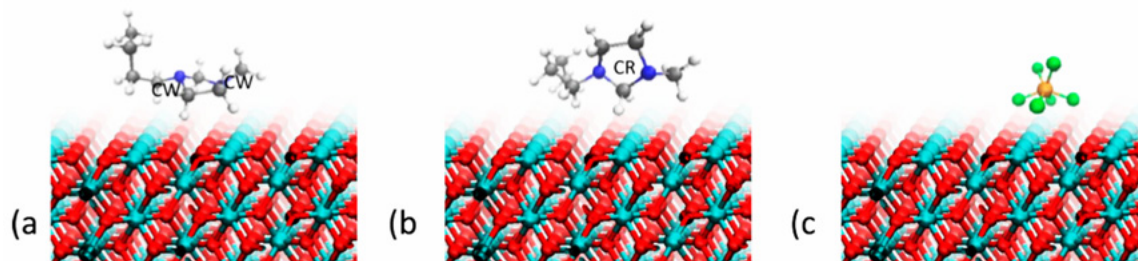
Figure 17. Schematic image of the arrangement of IL ions on the substrate surface: (*a*) placement of a cation parallel to the surface; (*b*) placement of a cation perpendicular to the surface; (*c*) placement of an anion on the surface. Color code is as follows: a fluorine atom is shown in *orange*, phosphorus atoms in *green*; hydrogen atoms in *white*, carbon atoms in *light gray*, nitrogen atoms in *dark blue*, oxygen atoms in *red*, and titanium atoms in *light blue*. Adapted with permission from [142]. Copyright © 2017 American Chemical Society. (For interpretation of the references to color in this figure legend, the reader is referred to the Web version of this article.)

To investigate the electrostatic potential in the vicinity of the TiO_2 surface, Mohammadpour *et al.* have studied two ILs of the hydrophilic nature, 1-butyl-3-methylimidazolium tetrafluoroborate ($[C_4mim][BF_4]$), 1-butyl-3-methylimidazolium chloride ($[C_4mim][Cl]$) and one IL of the hydrophobic nature, 1-butyl-3-methylimidazolium hexafluorophosphate ($[C_4mim][PF_6]$) (Fig. 18*a*), in the aqueous environment confined between of amorphous slit nanopores [143]. The MD simulations have been performed in an NVT ensemble at 300 K by using the GROMACS package. The modified OPLS-AA parameters for $[C_4mim][BF_4]$, $[C_4mim][Cl]$ and $[C_4mim][PF_6]$ ILs were taken from [141].

The authors have found that the behavior of IL ions inside the nanopores differs significantly from the adsorption behavior at the TiO_2 anatase surface so that the extent of an ion-pairing lifetime under such nanoscale confinement is substantially lower than its value found in the bulk solution. The asymmetric distribution of confined IL ions inside amorphous walls was attributed to the formation of ion-pairs (Fig. 18*b-f*), whereas there is a more homogenous-like distribution of cations and anions inside anatase pores. It has been suggested that the ion-pairing decreases in dilute aqueous mixtures of these ILs [143].
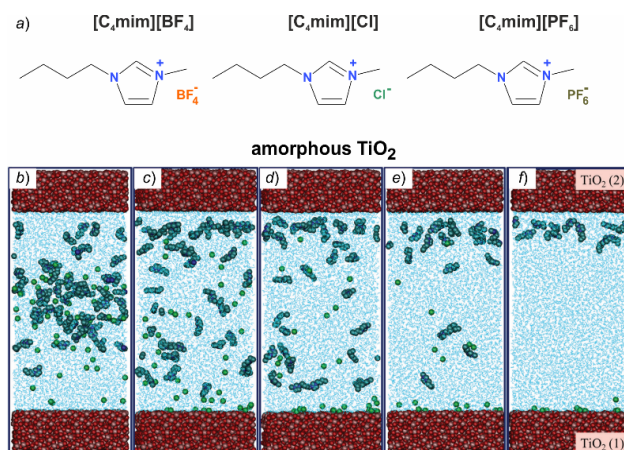
Figure 18. (*a*) Structures of ILs: [C$_4$mim][BF$_4$], [C$_4$mim][Cl], and [C$_4$mim][PF$_6$], respectively. Snapshots of the aqueous mixtures of [C$_4$mim][Cl] with different concentrations confined inside two amorphous TiO$_2$ walls with a 10 nm size pore after 20 ns: (*b*) 50, (*c*) 40, (*d*) 30, (*e*) 20 and (*f*) 10 ion-pairs, respectively. Adapted from [143] with permission from The Royal Society of Chemistry.

Considering the fact that a key element of any DSSC devices is the TiO$_2$/electrolyte interface, Kislenko *et al.* have studied the influence of different electrolytes (lithium ion (Li$^+$), 1,2dimethyl-3-propylimidazolium (DMPIM$^+$), tetrabutylammonium (TBA$^+$) as a cation and iodide ion (I$^-$) as an anion) (Fig. 19) on the formation of the anatase (101) double-layer structure in acetonitrile media [144]. Acetonitrile was described with the model proposed by Nikitin *et al.* [145]. The Amber94 FF was used for the TBA$^+$ cations. FF parameters for DMPIM$^+$ were taken from the work of Liu *et al.* [146], whereas some missing FF parameters were derived by *ab initio* calculations. Finally, the interaction potentials between TiO$_2$, acetonitrile, and IL ions were adapted from the earlier works of Schiffmann *et al.* [134].

It has been found that the physicochemical properties of such systems differ significantly, because of different size, symmetry, rigidity, and adsorptive properties of each cation. In the case of Li$^+$, which is prone to adsorption and intercalation, ions in bulk tend to aggregate in pairs, triplets, and larger clusters, representing chains of alternating Li$^+$ and I$^-$ ions, which leads further to decrease of their diffusion. In the case of DMPIM$^+$, the formation of ion pairs and ion clusters of irregular shapes were observed, while the aggregation of TBA$^+$ ions in bulk was not frequently occurred, because of its low absorptiveness. The acetonitrile molecules form a self-assembled monolayer on the TiO$_2$ surface, preventing adsorption/desorption phenomena for electrolytes. However, it has been pointed out that the adsorbed I$^-$ anions produce local "defects" in the solvent monolayer, which creates adsorption "channels" for Li$^+$ and DMPIM$^+$ cations and results in the formation of the adsorbed ion pairs [144].
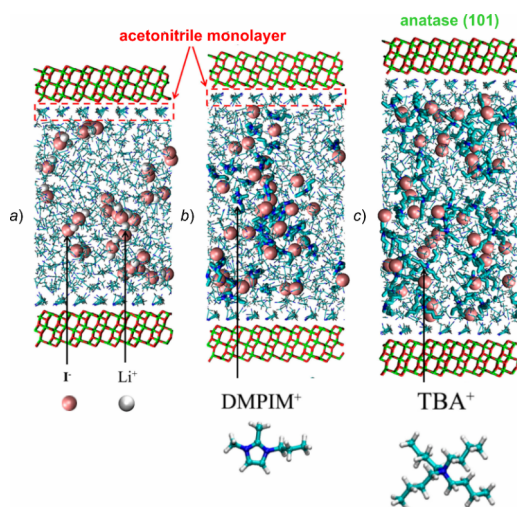
Figure 19. Snapshots of the MD simulation boxes with the electrolytes containing different cations: Li$^+$ (*a*), DMPIM$^+$ (*b*), and TBA$^+$ (*c*). Adapted with permission from [144]. Copyright © 2013 American Chemical Society.

21

MD Simulations of TiO$_2$ Nanoparticles

Amorphous TiO$_2$ Nanoparticles

Despite many advantages and popularity of the MA force-field of TiO$_2$ in material science modeling, its functional form has rather limited transferability to conventional biomolecular MD simulations. The majority of popular MD packages, such as GROMACS, ABMER, NAMD, etc., have well-documented FFs and numerous libraries of interaction parameters customized for describing the van der Waals interaction between atoms by the modified Lennard-Jones (LJ) potential (2). To overcome this difficulty, Zhou and co-workers [132] have re-parameterized the MA FF parameters for TiO$_2$ by fitting of the Buckingham potentials for TiO$_2$ with the Lennard-Jones one (Fig. 20 and Table 2).
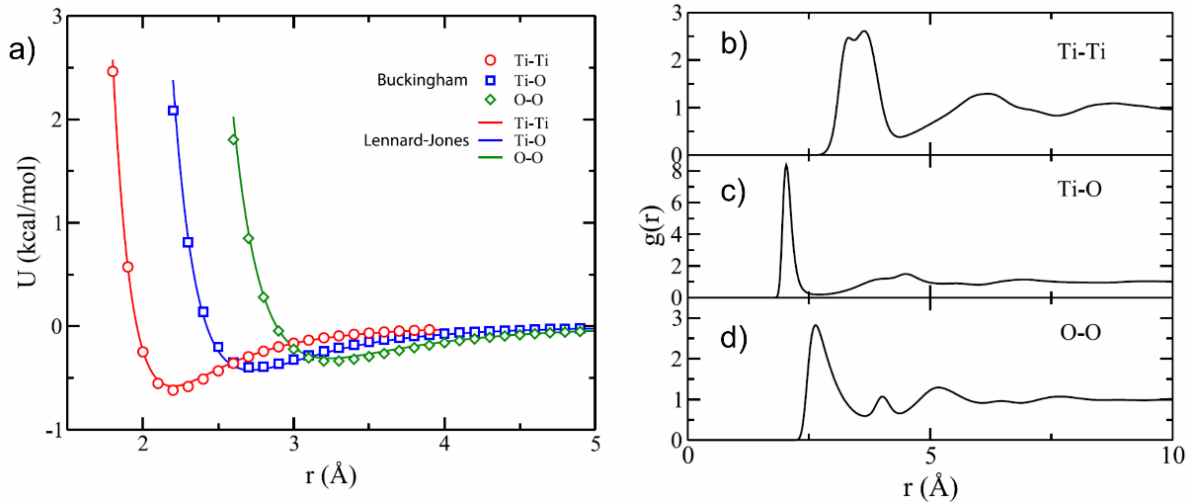
Figure 20. (*a*) Refitting of the Buckingham potential by the Lennard-Jones potential (2) for van der Waals modeling in the TiO$_2$ solid. (*b*)-(*d*) Radial distribution functions $g(r)$ for Ti–Ti (*b*), Ti–O (*c*), and O–O (*d*), respectively. Adapted from [132]. Copyright © 2015 AIP Publishing LLC.

$$V_{LJ}\left(r_{ij}\right) = \varepsilon_{ij}\left(\left(\frac{\sigma_{ij}}{r_{ij}}\right)^{12} - 2\left(\frac{\sigma_{ij}}{r_{ij}}\right)^{6}\right) \qquad r < r_{cutoff}$$

$$V_{LJ}\left(r_{ij}\right) = 0 \qquad r > r_{cutoff} \tag{2}$$

Table 2. Parameters of the Lennard-Jones potential (2) suitable for modeling of amorphous TiO$_2$ [132].

Interaction	ε_{ij} (kJ/mol)	σ_{ij} (nm)
Ti-Ti	2.4244	0.220
Ti-O	1.7723	0.272
O-O	1.2958	0.324

The customized FF parameters, adopted to the LJ form, were tested in MD simulating of the bulk structure of TiO$_2$, water interaction, and the adsorption of the C-terminal (from Met$_{548}$ to Glu$_{556}$) fragment of the human serum albumin (HSA) at a spherical TiO$_2$-NP [132].

Covalently Bound Models of Ti-O Interaction

A bonded FF, based on *ab initio* potentials, has been developed for interactions of water molecules with the (110) surface of rutile TiO$_2$ surface slabs [32]. This FF was suitable for atomistic MD simulations of the interfacial structure of the uncharged surface in contact with liquid SPC/E water and negatively charged surfaces in contact with dissolved electrolyte ions (Rb$^+$, Sr^{2+}, Zn^{2+}, Na$^+$, Ca^{2+}, Cl$^-$) [32-33,147].

TiO₂ Nanoparticles

Recent progress and achievement in MD simulations of physicochemical properties of TiO_2 nano-materials have been reviewed elsewhere [6]. Here, we provide the most significant advances and critical examples in this field.

MD simulations of isolated TiO_2-NPs in the three characteristic morphology (anatase, brookite, and rutile) have been reported, in which FF parameters were developed based on the MA force-field and fine-tuned with simulated X-ray diffraction data [19]. It has been suggested that the Ti-O bond length was found to be dependent on the coordination environment of Ti and independent of morphology and the size of NPs. The equilibrium Ti-O bond length for a titanium ion was assigned to be 0.186 nm for a four-coordinated ion, 0.192 nm for a five-coordinated ion, and 0.194 nm for an octahedral Ti ion, respectively [19]. Fig. 21 shows MD snapshots of 3 nm size NPs of quasi-spherical anatase and rutile NPs, respectively.
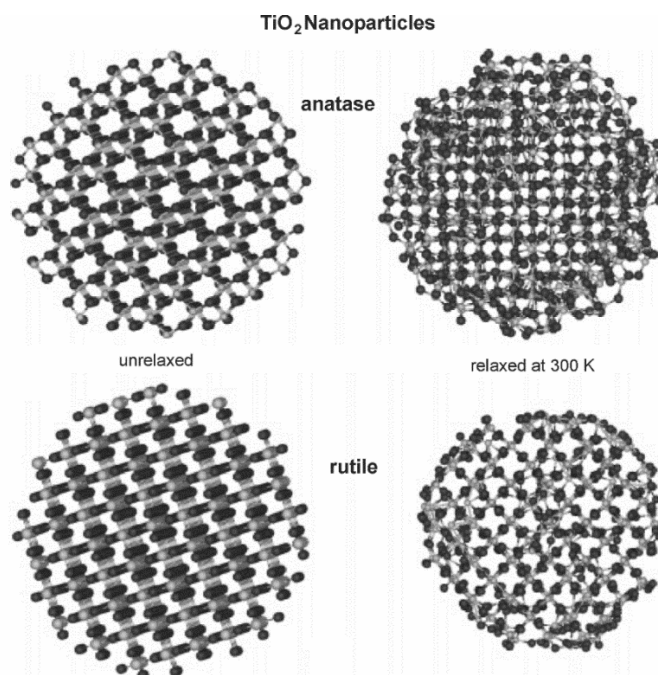
Figure 21. Snapshot of the unrelaxed (*left*) and relaxed at 300 K (*right*) structures of 3 nm anatase and rutile TiO_2-NPs. Adapted with permission from [19]. Copyright © 2005 American Chemical Society.

To get a better understanding of the size TiO_2 nanoparticles below which anatase NPs become more stable than rutile NPs (crossover diameter), MD simulations of TiO_2 nanoparticles were performed based on the MA potential [22]. Sintering-induced phase transformations between various polymorphs, such as anatase and rutile, were considered. It was found that phase transformation between anatase and rutile phases was facilitated by enhanced ionic mobility at temperatures near 1473 K, corresponding to the melting point of the NPs. The final sintering agglomerate transformed to the rutile phase provided one of the sintering NPs was rutile, while sintering of anatase and amorphous nanoparticles resulted in a brookite agglomerate. No such phase transformations were observed at temperatures away from NPs melting temperatures [22].

Alimohammadi and Fichthorn used MD simulations to study the aggregation of various TiO_2 (anatase) nanocrystals in vacuum [24]. They found that the aggregation occurred during the picosecond time-scale (Fig. 22). It was not driven by dipole-dipole interactions so that higher-order multipole moments were suggested as the driving force for the preferential alignment of TiO_2-NPs. These high-order multipole moments originate from under-coordinated O and Ti surface atoms on the edges between nanocrystal facets, which create localized regions of positive and negative charge [24].

MD simulations of the aggregation behavior of amorphous spherical TiO_2 of the size 6 nm were examined at 350 K and 1400 K by using the MA force-field [148]. Some localized atomic rearrangements were found to induce preferential crystallization near the surfaces of the NPs.
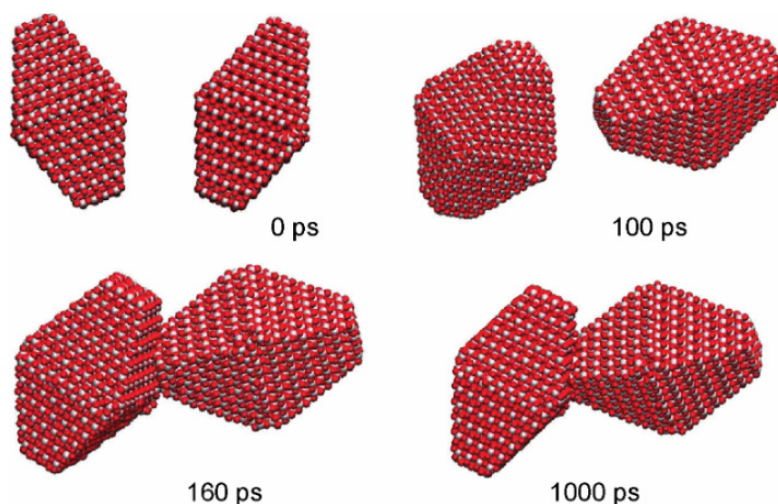
Figure 22. Snapshots of the aggregation of the large symmetric anatase-NPs taken at different simulation times. Adapted with permission from [24]. Copyright © 2009 American Chemical Society.

The deposition of amorphous TiO_2-NP of the size 3 nm onto a flat rigid TiO_2(B) nanocrystal surface was studied by using spatially resolved pulsed laser deposition combined with MD simulations to gain insight into the binding dynamic and the structural behavior of TiO_2-NP [149]. The simulations were based on the MA potential and carried out at discrete temperatures of 673 K, 873 K, and 1073 K, respectively. MD simulations revealed that an amorphous TiO_2-NP was attached to the surface within a picosecond time scale, during which some interdiffusion of its atoms into the topmost layer of the TiO_2(B) crystal occurred. Starting from a metastable amorphous nanoparticle with 8% TiO_6 octahedra, the TiO_2-NP tended to crystallize within the next 2 ns so that the Ti atoms have formed octahedral oxygen bonds [149].

Quantum-Chemical Calculations of Dye-Sensitized TiO_2

Dye-sensitized solar cells (DSSC), which are based on dyes adsorbed (or covalently connected) on the surface of TiO_2, have been intensively studied in recent years [150]. High efficiency of solar energy conversion, low cost of structural elements, and production of solar cells made them attractive for researchers. Many organic dyes have been studied as constituent elements of DSSC and the relationship between chemical structure and performance of corresponding solar cells has been intensively investigated [150]. In the current section, we present a brief description of the operational principle of DSSC. A more detailed overview can be found elsewhere [151-155].

The main constructive elements of DSSC are an organic dye and a TiO_2 semiconductor (Fig. 23). An organic dye (usually π-conjugated system) contains two structural parts connected by a bridge: a donor and an acceptor. The acceptor moiety is linked to the surface of the semiconductor.
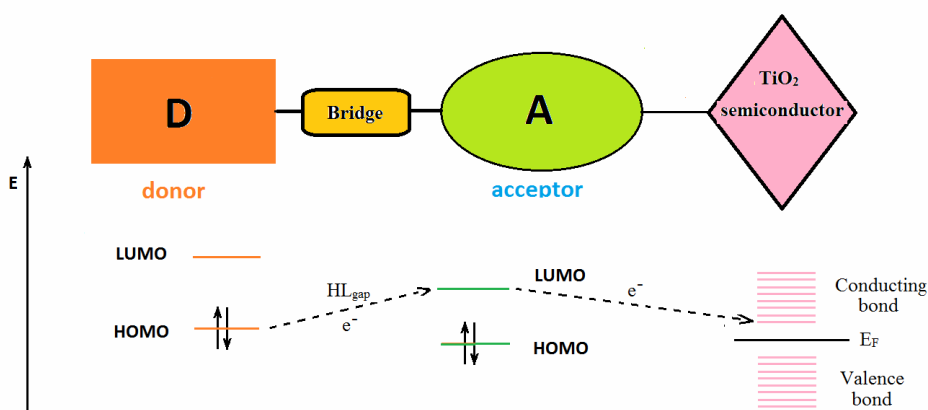
Figure 23. Schematic representation of a donor-acceptor DSSC system.

The generation of photocurrent in DSSC can be described in the following way. An organic dye in the ground state (S) absorbs the solar radiation and generates an electronically excited state (S*).

$$S + h\nu = S^* \tag{3}$$

The photoexcited electron is localized at an acceptor part of a dye. After that, the excited state S* injects the electron into a conduction band of TiO_2.

$$S^* \rightarrow S^+ + e^-, \tag{4}$$

$$e^- + TiO_2 \rightarrow e^-(TiO_2). \tag{5}$$

The oxidized dye (S^+) regenerates the ground state by I^- ion (mediator).

$$S^+ + e^- \rightarrow S. \tag{6}$$
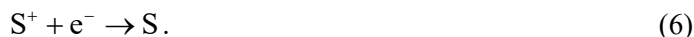
The performance of a DSSC element is characterized by several important parameters. First of all, it is a solar energy-to-electricity conversion yield ($\eta(\%)$)

$$\eta(\%) = \frac{V_{oc}J_{SC}FF}{I_0}, \tag{7}$$

where V_{oc} is open-circuit voltage of the cell (can be obtained as a difference between the Fermi level of semiconductor and a redox potential of a mediator), J_{SC} - photocurrent density at short circuit, FF = (0-1) is a fill factor, and I_0 is the intensity of the incident light.

Another important parameter is IPCE (incident Photon-to-Current conversion efficiency). It is defined as the number of electrons flowing through the external circuit. The IPCE can be calculated in the next way:

$$IPCE(\lambda) = LHE(\lambda) \cdot \Phi_{inj} \cdot \Phi_{coll}, \tag{8}$$

where LHE (light-harvesting efficiency) can be obtained using oscillator strength (f) directly from quantum chemistry calculations of electronic spectra. The Φ_{inj} and Φ_{coll} are measures of the efficiency of electron injection and collection through a photovoltage cycle.

$$LHE = 1 - 10^{-f}. \tag{9}$$

In addition, a lifetime of the excited state (τ_e) can be an important parameter as soon as long-term stability may lead to more effective charge transfer.

$$\tau_e = C/fE^2, \tag{10}$$

where E – the energy of excitation to the target state and C – a constant value.

It is clear that the light conversion efficiency of a DSSC element is heavily influenced by the chemical structure of a dye. It is why quantum chemical calculations play an important role in the investigation and development of high-performance DSSC devices.

During the last decade, the complexes "organic dye–TiO_2" were intensively studied by using different level quantum chemistry (*ab initio*) methods. The main problems of such studies are connected, firstly, with the necessity to consider large and "heavy" systems, and secondly, the study of spectral characteristics usually requires rather sophisticated methods. In recent years, many works have been devoted to the study of the electronic structure, geometry, and effects of energy transfer in "organic system–TiO_2" complexes. In the present review, we consider the essential articles only, in which, besides the actual computational data concerned with specific molecular systems, the general theoretic methodological aspects were discussed as well.

TiO_2 is one of the most investigated single-crystalline systems. The geometrical structure and properties of rutile and anatase surfaces are described in detail in many reviews (see, for instance, [156]). The results of quantum chemical calculations for TiO_2 are presented in a series of articles. Among the most interesting works in this field is the article [157], where the quantum chemical calculations for cluster models $(TiO_2)_n$ (rutile n=20, and anatase n=92) were performed. Different structural and electronic properties were obtained by using several quantum chemistry approaches. Among them, the semiempirical PM6 method, Hartree-Fock (HF), DFT (BLYP, B3LYP, PBE, PBE0, CAM-B3LYP, and ωB97 functionals) approaches. The LANL2DZ basis set was used. The presented data demonstrated significant sensitivity of some critical parameters of the electronic structure to the chosen functional. However, the parameters of the electronic structure demonstrated small sensitivity to the geometrical structure optimization method. For instance, the values of the HOMO-LUMO gap (HL) ob-

tained using the B3LYP functional vary by only 0.08 eV for differently optimized structures (different DFT functionals were used for optimization). Surprisingly, the HL gap, obtained, for instance, with B3LYP and CAM-B3LYP, differs by as much as 2.91 eV! Also, the performance of different exchange-correlation functionals for calculations of rutile and anatase was compared in ref [158].

Another structural aspect of anatase TiO_2 NPs was discussed [159]. In this study, the nanospheres and nanocrystals of various sizes were compared (Fig. 24). The HSE06 functional, which is considered as the best suited to describe semiconductors, was used. The comparison of HSE06 with the standard B3LYP functional was also presented. Faceted and spherical nanoparticles have been cut from the bulk anatase crystal (Fig. 24*a-b*). The initial geometry of anatase was derived from DFT calculation. It was shown that the calculated surface energies for NPs higher than for a regular surface. In general, it was demonstrated that these NPs have essentially different structural and electronic properties.
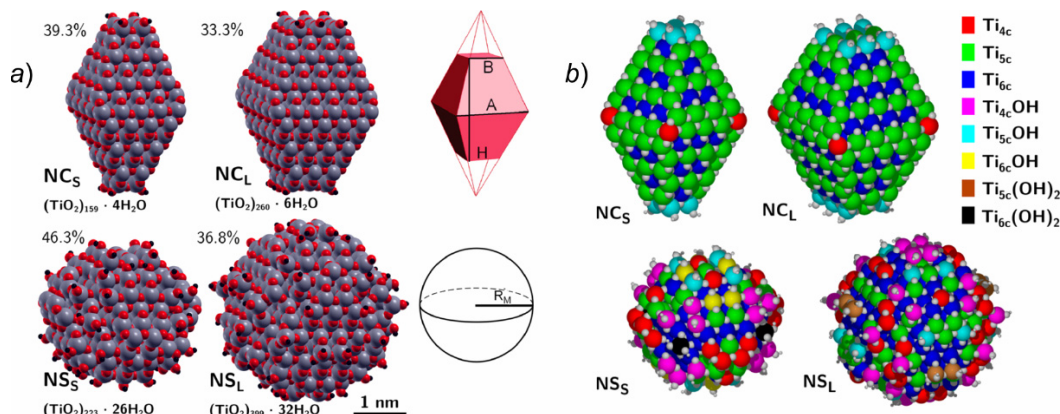
Figure 24. (*a*) *Top*: Space-filling representation of the faceted anatase NPs and the corresponding schematic representation of the Wulff-shape decahedron with its parameters A, B, and H. *Bottom*: Space-filling representation of the spherical anatase NPs and the corresponding schematic representation of the sphere with radius RM. The HSE06 optimized nanostructures are shown. The surface-to-bulk % ratio and the stoichiometry of each NP are indicated on the side of the model. (*b*) The position of the Ti atoms with different coordination spheres within the various NPs is visually shown by the color-coding indicated on the right side. Adapted with permission from [159]. Copyright © 2015 American Chemical Society.

The electron and geometrical structure of TiO_2 nanocrystals with an excess of electrons introduced by defects were investigated in [160]. The spin-polarized variant of the DFT theory and the exchange-correlation functional HSE06 were used to characterize the electronic properties of the nanocrystals. The various oxygen and titanium atom (interstitial) defects were created by removing an O atom (for oxygen vacancy), and Ti was inserted into interstitial location between oxygen atoms (Ti_{int} defect). According to the presented data, the oxygen vacancy demonstrated similar stability at the surface and sub-surface sites, whereas Ti_{int} was more stable at sub-surface sites. In general, the result of the study reveals the possibility of tuning the band structure through defects.

A water–TiO_2 (anatase) interface was investigated in [161-162]. The calculations were performed by using a semiempirical variant of the DFT theory. Namely, the tide binding model, as an approximate DFT method (DFTB), was used for large cluster calculations. The DFTB method is more than a thousand times faster than the conventional B3LYP approach. Thus, the DFTB method can be used to calculate large clusters composed of thousands of atoms. The test calculations that were performed in [161-162] showed a rather good correspondence between the geometric parameters (water molecules and anatase slab cluster) obtained by the DFTB method and those obtained by the DFT/PBE method. In general, it proved that the DFTB set of parameters was able to reproduce the main features of the Ti/(water multilayers) interface with the DFT accuracy. However, it was pointed out that the DFT level of theory is still required when the electron excitations and electron transfer were under investigation. The benchmark study of DFTB against DFT is given in [163].

The accuracy of quantum chemical calculations of excited states was recently discussed in [164]. The results of the time-dependent DFT theory (TD-DFT) were compared with the equation of motion coupled-cluster singles and doubles (EOM-CCSD) data for rather small $(TiO_2)_n$ with *n* varying from 1 up to 13 clusters, respectively. High-quality basis sets were used, such as def2-SV(P),

def2-TZVP, and def2-TZVPP, respectively. According to the computational data of the TD-DFT (with different functionals used) and EOM-CCSD methods demonstrated qualitatively similar results for excitation energies of TiO$_2$ NPs. However, for systems with a significant charge-transfer character, the standard functionals (e. g. B3LYP) demonstrated a rather poor agreement with the exact EOM-CCSD approach [164]. Such a situation can be illustrated by the data presented in Table 3.

Table 3. Excitation energies (in eV) for the four lowest states ((TiO$_2$)$_3$ cluster, C_l symmetry) [164].

№	def2-TZVP			def2-SV(P)	def2-TZVPP
State	B3LYP	CAM- B3LYP	BHLYP	EOM-CCSD	EOM-CCSD
1	3.33	3.78	4.29	3.48	3.69
2	3.49	3.91	4.41	3.59	3.80
3	3.56	4.21	4.57	3.94	4.11
4	3.71	4.33	4.68	4.02	4.20

One can see from Table 3 that the best quantitative agreement between TD-DFT and EOM-CCSD (with the best basis set def2-TZVPP) was achieved for the CAM-B3LYP functional, while B3LYP demonstrated the rather poor accuracy [164].

The results of quantum chemical calculations of dye-sensitized TiO$_2$ complexes are presented in numerous publications [165-170]. The range of dyes used for DSSC elements is amazing with its variety [171-178]. Some selected studied dyes used in solar cells are shown in Fig. 25. Beyond this list, many dyes are continuously designed as donor-acceptor π-conjugated systems based on coumarin, polyene, cyanine, thiophene, indoline, xanthene, perylene, porphyrin, and boron dipyrromethenes (BODIPY), etc. The corresponding reviews of organic dyes used for DSSC can be found elsewhere [151,155,165,179-180].

Some essential structural and electronic criteria, which required (but not sufficient) for a dye to generate a photocurrent upon adsorption on a semiconductor surface, have been suggested as following [165]:

- The anchoring group should be positioned on the electron-accepting group.
- The HOMO and LUMO of the dye should be energetically above the valence band edge (VBE) and the conduction band edge (CBE) of the semiconductor, respectively.
- The absorption spectrum should significantly overlap with the solar spectrum.
- The transition involved in the photoconversion phenomenon should have a high intensity.
- The fluorescence lifetime should be sufficiently high (above the nanosecond time scale) to allow an electronic injection to the semiconductor from the excited state of the dye before quenching of the excited state by radiative decay.
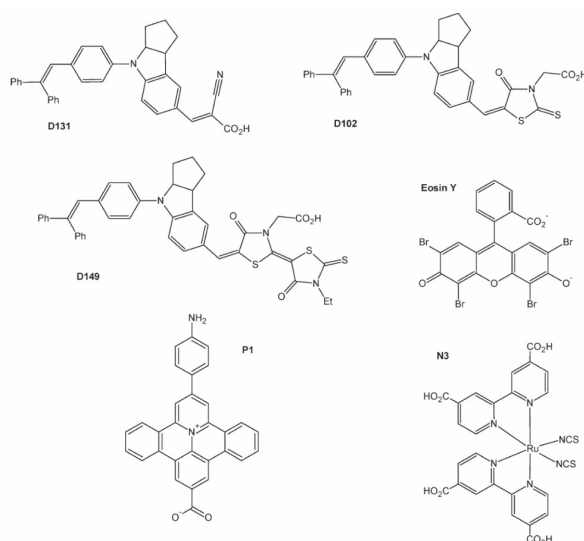
Figure 25. Structures of selected dyes: indolines (D131, D102 [181], and D149) [182], eosin-Y [176], pyridinium-based dye P1 [166], N3 (*cis*-[Ru-(4,4′-COOH-2,2′-bpy)$_2$(NCS)$_2$]) [175], respectively. Adapted with permission from [165]. Copyright © 2012 American Chemical Society.

One of the most interesting works concerned dye-TiO$_2$ complex is the article [183]. Herein indicates that even for rather simple π-systems, the interaction with TiO$_2$ particles may lead to substantial changes in their optical properties. The catechol and dopamine molecules (Fig. 26a) in contact with TiO$_2$-NPs were studied. Three modes of connection with TiO$_2$ were discussed. The bidentate mode corresponds to the connection of the molecule with two Ti sites via two oxygen atoms (Fig. 26b). The chelate mode is a connection of a molecule with a single Ti site via two oxygen sites. The monodentate mode corresponds to the connection of a molecule with a single Ti site, which is realized via a single oxygen site (Fig. 26b). The TD-DFT/CAM-B3LYP/6-311+G* approach was used for an adequate description of charge-transfer excitations. It was demonstrated that the interacting systems show the redshift of the absorption compared to isolated molecules and clusters. The calculation of natural orbits indicates the significant charge-transfer character of the excitations [183].
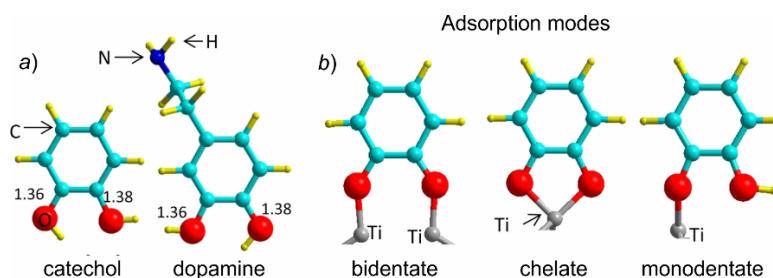
Figure 26. (a) Schematic representation of catechol and dopamine. (b) Possible adsorption modes of catechol. Adapted with permission from [183]. Copyright © 2016 American Chemical Society.

Based on synthesized polycyclic 9,14-dihydro-4H-dithieno[2′,3′:2,3;3′,2′:10,11]-piceno[1,14,13,12-bcdefgh]carbazole (DTPC) the *in silico* analysis and design for suitable electron withdrawing structures was performed [184]. The electronic structure calculations have been performed by using the B3LYP and MPW1K functionals with the 6-311G(d,p) basis set. The molecular structure of investigated systems is typical for a dye used in DSSC elements (Fig. 27). Here the main part of a molecule is electron donor fragment, while **X** is an electron acceptor. The carboxylic acid that was attached to acceptor group **X** is an anchoring group since this group can provide strong dye-TiO$_2$ adsorption [184]. Geometry and electronic structure of the ground and excited states for systems with different **X** (Fig. 27) was predicted by means of the DFT method. The calculated by using functional B3LYP maximum absorption wavelength for parent dye (λ_{max}=596 nm) agreed well with known experimental data (λ_{max}=609 nm) [184].
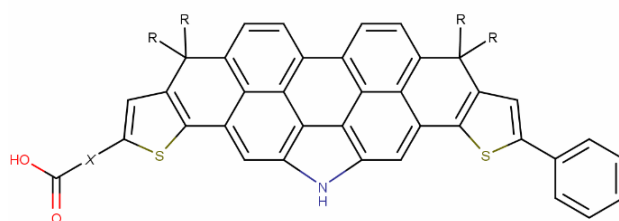
Figure 27. The molecular structure of the parent dye studied in [184].

The most critical parameters that influence the DSSC device performance were calculated. Among them, the LHE (light-harvesting efficiency), the number of injected electrons, the electron-injection lifetime, and the quantum-energy alignment of the adsorbed dye molecule to TiO$_2$ components. The results of work demonstrated that by modifying the acceptor group (**X**) the optical properties of dyes and the energy alignment of dye–TiO$_2$ structure could be tuned [184].

The effects of electron donor group on electronic and optical properties of arylamine-based dyes for DSSC were investigated in [185] (Fig. 28). DFTB optimized geometries of a dye and dye-TiO$_2$ conjugates were used for TD-DFT excited states calculations. The following functionals were used: CAM-B3LYP/3-21G(d), LC-ωPBE/6-31+G(d), and mPWDandHPW91/6-31G(d), respectively. The results show that the functional ωPBE/6-31+G(d) with the damping parameter of 0.175 au^{-1} provides the best agreement with experimental values. New rigid triarylamine based dyes were designed. Some

critical parameters, such as η(%) and LHE, as well as other characteristics, were calculated. It was demonstrated that the investigated optical properties of new systems match with the requirement of an effective sensitizer [185].
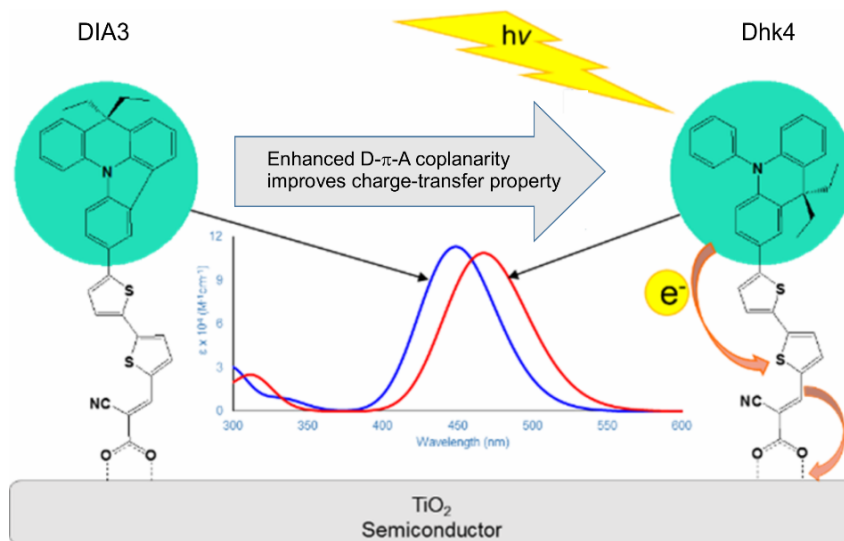
Figure 28. Schematic illustration demonstrating that new dye Dhk4 was designed by modifying the rigidity of its donor moiety via altering the type and position of binding in the donor group. This structure modification leads to distinct planarity of the dyes, which significantly affects its properties so that Dhk4 dye showed more red-shifted and broadened absorption spectra owing to the enhanced coplanarity between its donor and π-bridge moiety, as compared with a parent dye DIA3. Adapted with permission from [185]. Copyright © 2016 American Chemical Society.

In the ref. [186], the effects of various anchoring groups on the electronic coupling of dye-to-TiO$_2$ were investigated by means of *ab initio* and molecular dynamics simulations. The set of anchoring groups includes the following structures: carboxylic acid (–COOH), biscarbodithiolic acid (–CSSH), phosphonic acid (–PO(OH)$_2$), sulfonic acid (–SO$_3$H) and hydrixamic acid (–CONHOH), respectively (Fig. 29*a*). The TD-DFT/PBE0/6-31G(d,p) with the PCM model for tetrahydrofurane solvent was used for excited-state calculations. It was shown that different anchoring groups give noticeably different contributions to LUMO. For instance, the contribution of a CSSH group is more significant than that of the COOH moiety. Hence, the CSSH group is favorable for electron injection from a dye to TiO$_2$. Also, the effect of anchoring groups on an aggregation of a dye was investigated by MD simulations (Fig. 29*b*).
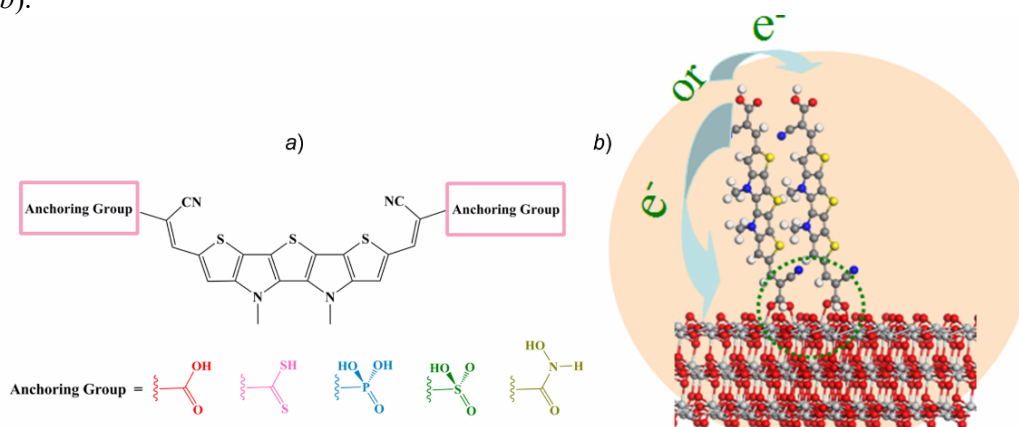
Figure 29. (*a*) Sketch structures of investigated dyes and corresponding anchoring groups. (*b*) A graph of the adsorption configuration of a head-to-head stacking dimer of the dye with the anchoring moiety COOH onto the TiO$_2$(101) surface, indicating two possible routes for electron transfer: (*i*) electron injection from a dye to TiO$_2$ and (*ii*) dye-to-dye electron migration, respectively. Adapted with permission from [186]. Copyright © 2017 American Chemical Society.

In addition, the role of anchoring modes in adsorption of retinoic acid (RA) Fig. 30*a* on TiO$_2$ was studied by DFT calculations [187]. Three anchoring modes of RA, which contains a carboxylic acid group, were considered, as shown in Fig. 30*b*.
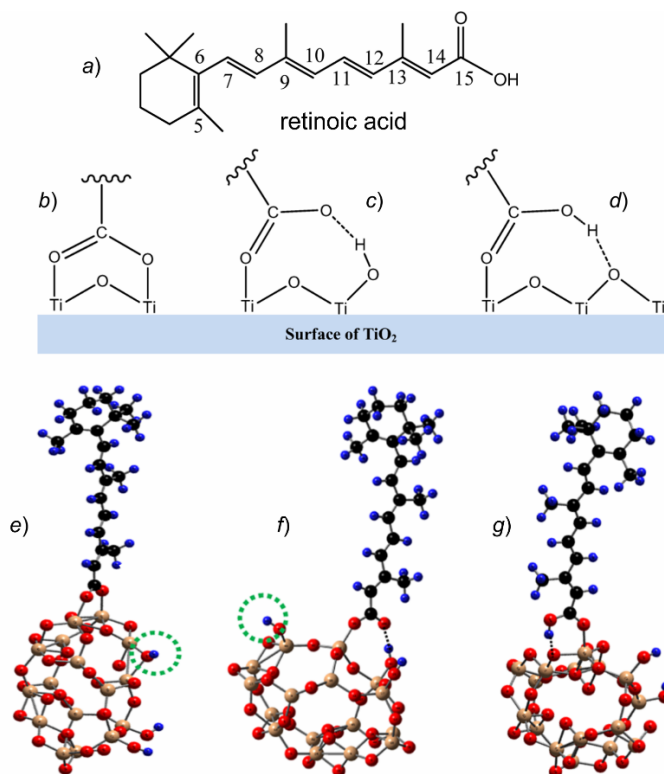
Figure 30. (*a*) Structure of retinoic acid (RA). (*b-d*) Three anchoring modes of a carboxylic acid group of RA on the surface of TiO$_2$: (*b*) the carboxylic acid group loses a proton and forms two coordination bonds with two surface Ti atoms of TiO$_2$; (*c*) the carboxylic acid group loses a proton and forms one coordination bond with one surface Ti atom of TiO$_2$ and one hydrogen bond (H-bond) with a Ti−OH group on the surface of TiO$_2$; (*d*) the carboxylic acid group does not lose a proton and forms one coordination bond with one surface Ti atom of TiO$_2$ and one H-bond due to the interaction between the OH group of the carboxylic acid group and the bridging oxygen atom on the surface of TiO$_2$. Optimized structures of RA adsorbed onto a (TiO$_2$)$_{16}$ cluster by various anchoring modes: (*e*) anchoring mode *b*, (*f*) anchoring mode *c*, and (*g*) anchoring mode *d*, respectively. Adapted with permission from [187]. Copyright © 2019 American Chemical Society.

The analysis of the B3LYP/6-31G(d) optimized structures revealed (Fig. 30*b*) that among the three anchoring modes, the mode *c* involving surface Ti−OH groups was suggested to have the highest driving force for photo-induced electron transfer. In this bound geometry, the mixing between the RA's LUMO and the conduction band states of TiO$_2$ was also the highest. The calculated results were supported by EPR measurements, which showed enhanced light-driven charge separation upon increasing the density of the Ti−OH groups on the surface of TiO$_2$. It was found that the anchoring modes affected the bond length, degree of conjugation, energies of the HOMO and LUMO, and the mixing of the dye's excited states with the conduction band states of a semiconductor (Fig. 30*e-g*).

The influence of the chemical environment at the electrolyte/dye/TiO$_2$ interface on the adsorption geometries and electronic properties of a dye adsorbed on TiO$_2$ was considered by first-principles calculations [188]. Various adsorption modes of a series of organic dyes (Fig. 31*a-b*) on the (101) surface of anatase TiO$_2$ were examined in the absence and the presence of explicitly coadsorbed solvent (water or acetonitrile) molecules. Periodic DFT calculations were carried out within the generalized gradient approximation (GGA) using the PBE exchange-correlation functional [188]. It was found that coadsorbed solvent molecules introduced important modifications on the dye adsorption geometry with respect to the geometry calculated in vacuo (Fig. 31*c-f*). In particular, the bonding distance of the dye from the Ti anchoring atoms increased, whereas the adsorption energy decreased. Moreover, the adsorbed solvent induces the deprotonation of the dye due to the changing the acid/base

properties of the system. Analysis of the electronic properties for the dye-sensitized TiO_2 structures in the presence of coadsorbed solvent molecules revealed an upward shift in the TiO_2 conduction band from 0.5 up to 0.8 eV in acetonitrile [188]. It should also be noticed that a similar shift of the TiO_2 conduction band was estimated for a solvent monolayer on unsensitized TiO_2.
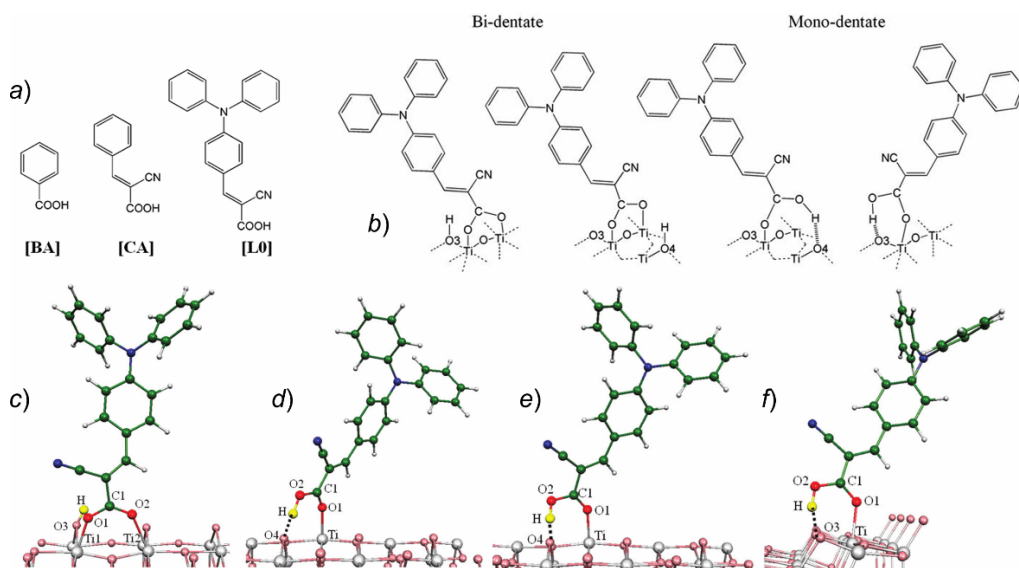
Figure 31. (*a*) Chemical formulae of the investigated molecules: benzoic acid [BA], 2-cyano-3-phenyl-acrylic acid ([CA]), and 4-(diphenylamino)phenylcyanoacrylic acid [L0]. (*b*) Schematic representation of the considered adsorption modes of [L0] on a TiO_2 anatase (101) surface. (*c-f*) DFT optimized adsorption structures of [L0]: bidentate (*c*); molecular monodentate (*d-f*). Adapted with permission from [188]. Copyright © 2012, American Chemical Society.
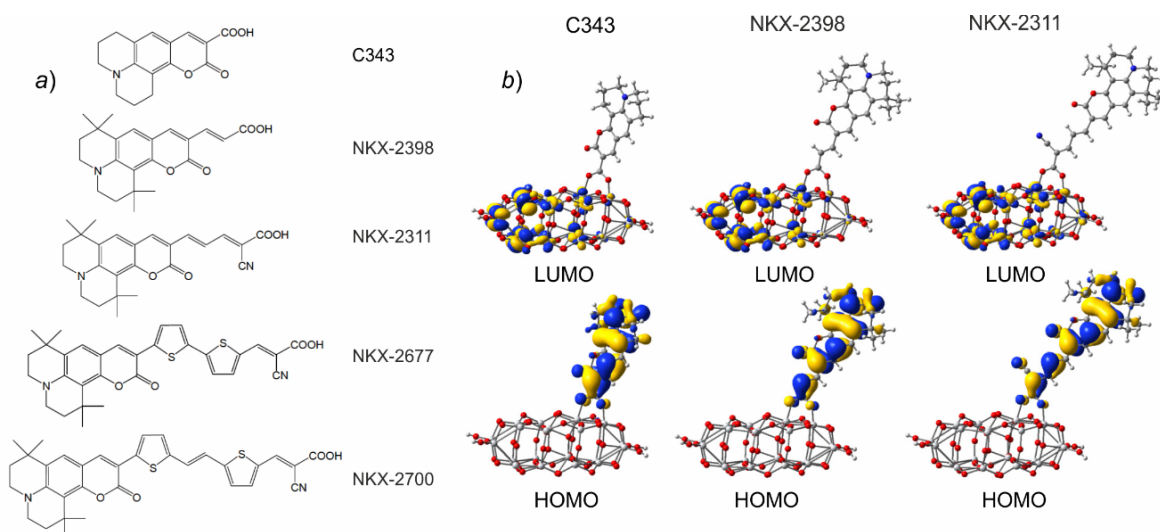
Figure 32. (*a*) Molecular structures of coumarin-based dyes. (*b*) Isodensity surfaces (0.02 e/bohr^3) of the HOMO and LUMO orbitals of the dyes adsorbed on the TiO_2 nanocluster ($Ti_{24}O_{50}H_4$) calculated with the B3LYP functional and a combined basis DZVP/LANL2DZ and modeled in PCM-water. Adapted from [169]. Copyright © 2013 MDPI (Basel, Switzerland).

A joint experimental and computational study of the optical and charge transfer properties of D102 dye in the presence of Li-TFSI and EMIM-TFSI additives, as well as at the dye-sensitized TiO2 interface, was reported [181]. Experimental UV adsorption spectra showed that the spectral shifts of D102 are negligible for the dye in solution. However, upon moving to the TiO_2 film these additives resulted in some slight red-shifts in spectra, accompanied with the appearance of a lower-energy shoulder in the absorption spectrum. B3LYP/6-311G** and PBE0/6-311G** calculations showed the formation of weak dye/additive complexes in solution and also predicted spectral red-shifts. Moreover, the strong

effect of these additives on the electronic coupling between the dye's LUMO and the TiO$_2$ conduction band states, approximated by (TiO$_2$)$_{82}$ (101) two-layer anatase slab [181].

The systematical theoretical study of seven D−A−π−A-based indoline (IND) dyes (Fig. 33a) was comprehensively investigated via quantitative-structure−property relationships to evaluate their prospect of application in DSSCs [195].
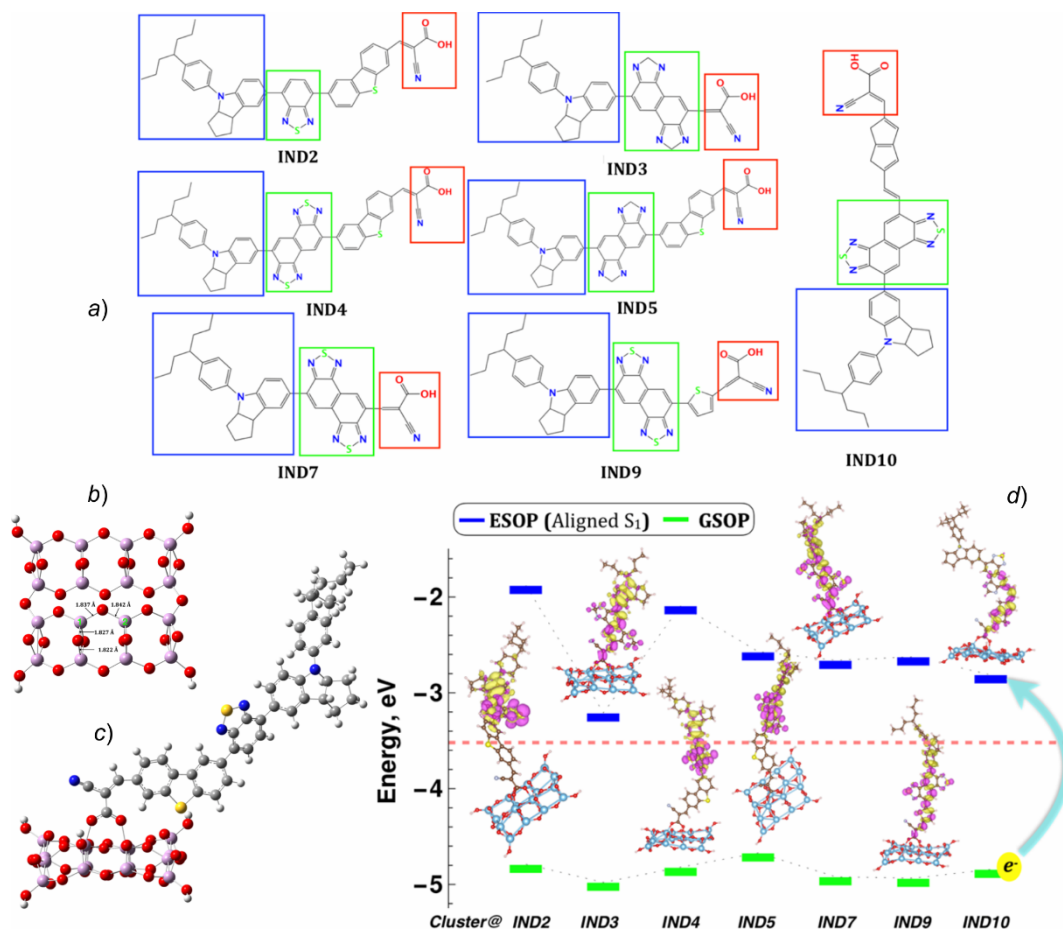
Figure 33. (a) Chemical structures of seven IND dye-sensitizers with D−A−π−A framework. Colored boxes are indicating constituents of the framework. Blue (D), green (A or internal acceptor), red (A or cyanoacrylic acid), and the fragment in between red and green box is the π-spacer, (b-c) Fully relaxed optimized geometry of the model TiO$_2$ cluster (Ti$_{16}$O$_{34}$H$_4$) and the IND2/TiO$_2$-cluster with bridged bidentate mode, (d) Energy alignment of the IND dyes with respect to TiO$_2$ along with the CDD of the dyes/TiO$_2$-cluster complex and CB of TiO$_2$. Adapted with permission from [195]. Copyright © 2019 American Chemical Society. (For interpretation of the references to color in this figure legend, the reader is referred to the Web version of this article.)

Optoelectronic properties of the isolated dye and dyes adsorbed on a TiO$_2$ cluster were explored by DFT (B3LYP and CAM-B3LYP with a combined 6-31G(d,p)/LANL2DZ basis set) and TD-DFT methods (Fig. 33b-c). Light absorption spectra, vertical dipole moment, shift of the conduction band of the semiconductor, excited-state lifetime, a driving force of electron injection, the photostability of the excited state, and exciton binding energy were computed. The authors showed that the presence of an internal acceptor such as pyrido[3,4-b]pyrazine would influence greater the open-circuit voltage (V$_{OC}$), compared to the benzothiadiazole moiety (Fig. 33d). Considering the balance between the V$_{OC}$ and J$_{SC}$ (short circuit current), the IND3, IND5, and IND10 dyes were suggested as the most suited to be utilized as potential candidates for DSSC [195].

Different mechanisms for electron injection in DSSC are discussed in ref. [196]. The aim of work was to investigate structural aspects of a dye, which lead to specific electron injection to TiO$_2$ mechanism. The classification of sensitizers was proposed. Type I of sensitizers corresponds to the indirect mechanism. For these systems, the orbitals involved in excitations mainly localized in the molecule. Type II is characterized by virtual orbitals mostly localized on a dye that appears well into the conduc-

tion band of the semiconductor. These orbitals are formed via the interaction of d_{z^2} orbitals of Ti atom and p-orbitals of the oxygen atom of the dye [196].

A series of Ru(II)-based dyes, labeled as *N* dyes, such as N3 (Fig. 25), N719, N749, etc. have become prototypical benchmark systems for *ab initio* calculations sensitizing effect to TiO$_2$ [197-199]. Earlier computational investigations of the absorption spectrum and the alignment of the ground and excited state energies for an N719 dye, adsorbed on an extended TiO$_2$ anatase slab exposing the majority (101) surface, were carried out by DFT/TDDFT calculations (Fig. 34*a*) [198]. The geometry of the dye-TiO$_2$ conjugate was optimized by using the PBE exchange-correlation functional together with a plane wave basis set and ultrasoft pseudopotentials [199]. TDDFT calculations were performed on the optimized geometries, employing the hybrid B3LYP functional with a 3-21G* basis set. A polarizable continuum model of solvation (C-PCM) was employed to treat the effect of the surrounding water solvent. It was found that the calculated and experimental absorption spectra for the dye-TiO$_2$ conjugate were in excellent agreement with an absorption maximum deviation below 0.1 eV (Fig. 34*b*). The lowest optically active excited state was found to lie ca. 0.3 eV above the lowest TiO$_2$ state. The latter was characterized with a sizable contribution from the dye π^* orbitals, strongly mixed with unoccupied TiO$_2$ states (Fig. 34*c*). Therefore, an ultrafast electron injection component was predicted on the basis of the strong coupling and of the matching of the visible absorption spectrum and density of TiO$_2$ unoccupied states (Fig. 34*d*).
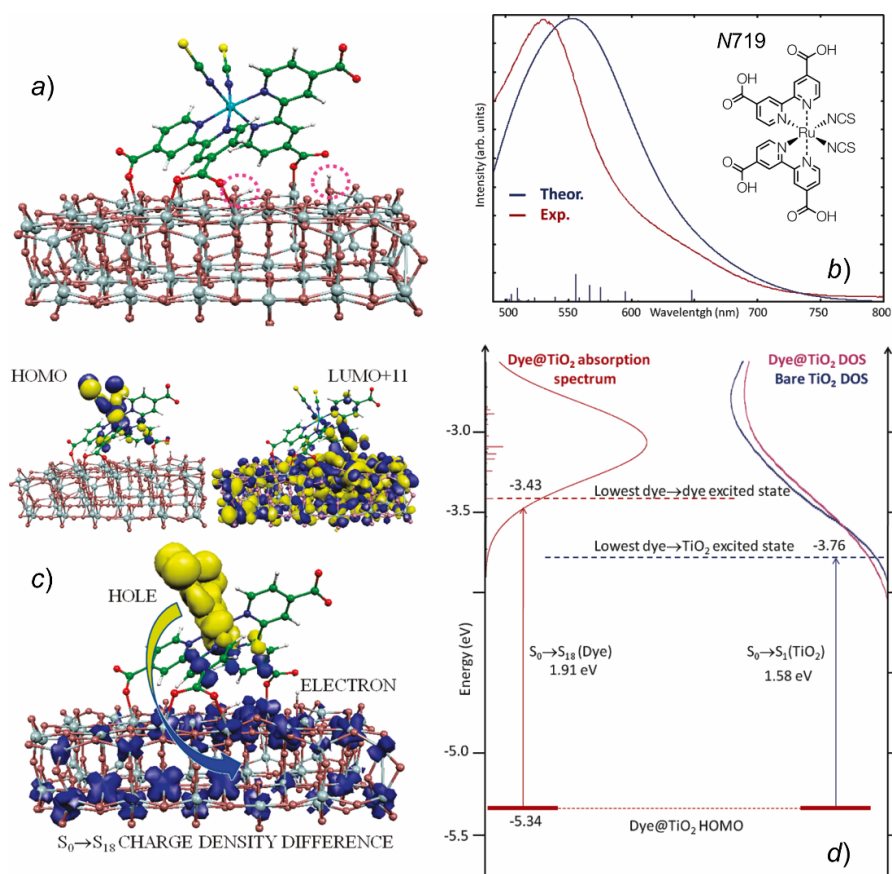
Figure 34. (*a*) Optimized structure of the N719 dye with two protons and no counterions adsorbed on the (TiO$_2$)$_{82}$ slab. The position of the two protons is denoted by the dotted circles. (*b*) Comparison between the experimental (*red*) and calculated (*blue*) absorption spectra of N719 on TiO$_2$. For clarity, the experimental spectrum intensity has been normalized to the calculated absorption maxima. Blue vertical lines represent unbroadened transition wavelengths and oscillator strengths. (*c*) Isodensity plots of the HOMO and LUMO+11 of the N719-TiO$_2$ conjugate. *Bottom*: Charge density difference between the ground state (S$_0$) and the S$_{18}$ excited state. A *blue* (*yellow*) color signifies and increases (decrease) of charge density upon electron excitation. (*d*) *Left*: alignment of the ground and excited-state energy levels for the N719-TiO$_2$ conjugate. *Right*: the calculated density of unoccupied TiO$_2$ states, aligned to the energy of the lowest TiO$_2$ state in the conjugate. Adapted with permission from [198]. Copyright © 2011 American Chemical Society. (For interpretation of the references to color in this figure legend, the reader is referred to the Web version of this article.)

Successes, failures, and challenges of quantum chemical calculations of excited states and alignment of energy levels in dye-sensitized solar cells were critically analyzed in the context of the potential and limitations of current DFT and TDDFT computational methods to model DSCs [197]. Pastore, Fantacci, and De Angelis considered the ground and excited-state properties of both isolated and TiO_2-adsorbed metallorganic and fully organic dyes, relevant to modeling the dye→semiconductor electron injection process. By reviewing previous data from their laboratory, combined with new calculations (Fig. 35a-b), they suggested that ruthenium dyes are typically accurately described by standard DFT approaches [165,197-198]. However, in the case of highly conjugated organic dyes, which are often characterized by strong charge-transfer excited states, some specifically tailored exchange-correlation functionals, such as CAM-B3LYP, are required. It was shown that for donor−acceptor organic dyes, a simple picture based on the dye lowest unoccupied molecular orbital (LUMO) broadening accounts for the different interfacial electronic coupling exhibited by dyes with different anchoring groups. It was also concluded that the explored DFT/TDDFT functionals, such as B3LYP, MPW1K, and CAM-B3LYP, estimate a balanced description of the dye-TiO_2 excited states and of the alignment of the dye excited states with the semiconductor manifold of unoccupied states with different accuracy (Fig. 35c) [197].
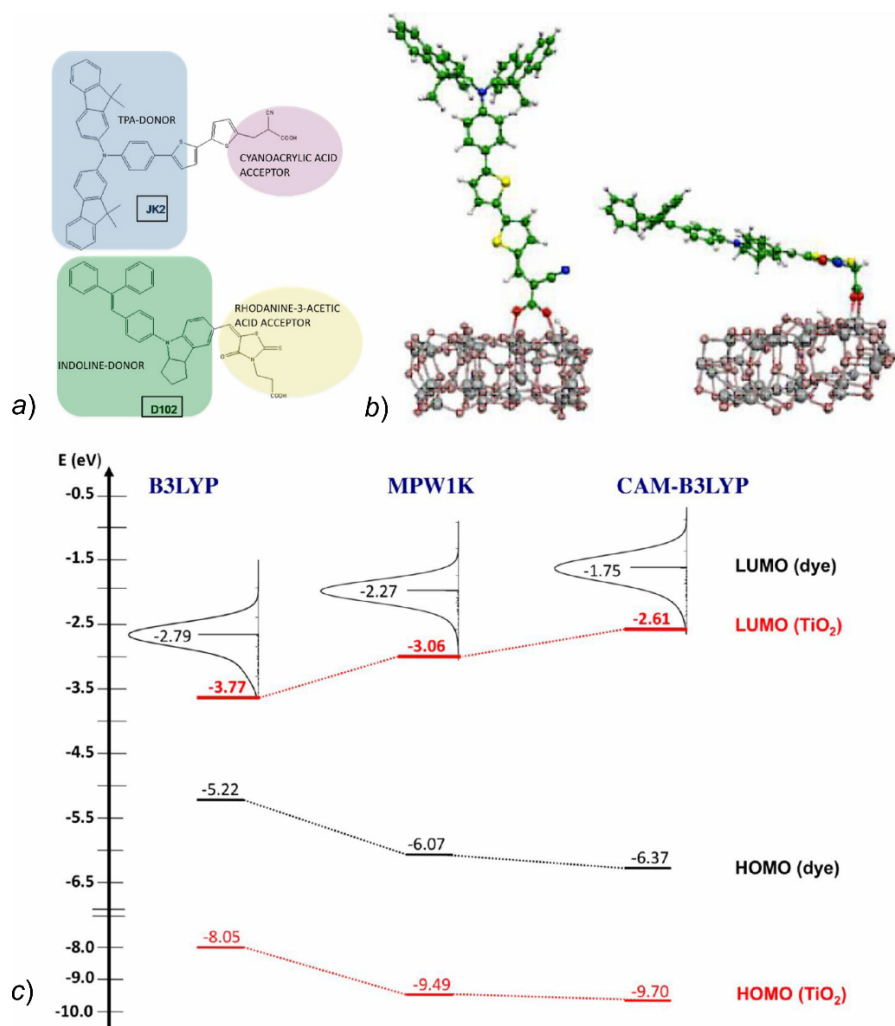
Figure 35. (a) Molecular structures of a JK2 dye, containing a triphenylamine(TPA)-like donor (*N,N*-bis(9,9-dimethylfluorene-2-yl)phenyl) with a cyanoacrylic acid as an anchoring unit, and a D102 dye, containing indoline and rhodanine-3-acetic acid as electron donor and acceptor groups. (b) Optimized geometries of JK2-$(TiO_2)_{38}$ and D102-$(TiO_2)_{38}$. (c) Scheme of the energy levels of the D102-TiO_2 system calculated by the B3LYP, MPW1K, and CAM-B3LYP functionals in the PCM water solution. The dye's LUMO is represented through the dye's projected density of states (PDOS). Adapted with permission from [197]. Copyright © 2013 American Chemical Society.

A fully atomistic computational approach was suggested to capture the differences between direct (type-I) and indirect (type-II) photoinjection mechanisms by a time-dependent density functional tight-binding (TD-DFTB) approach [200-203]. The type-I photoinjection involves two steps (Fig. 36*a*): (*i*) an excitation from the ground state to the excited state of the dye, which is produced by the absorption of a photon, (*ii*) an electron transfer to the conduction band of the semiconductor nanoparticle (NP). Whereas the type-II photoinjection is referred to as the one-step electron injection from the ground state of the dye to the conduction band of the semiconductor upon photoabsorption. It should be noted that, in the type-II mechanism, a new charge-transfer band appears, which characterizes the direct electron excitation into the conduction band and can be observed in the UV−vis absorption spectrum. On the opposite, in the type-I mechanism, no new bands are expected in the UV−vis spectra. A model anatase TiO_2 NP (a 270 atom (90 TiO_2 units)) functionalized with different dyes, such as alizarin, coumarin C343 (C343), catechol, cresol, [Ti(Ph-tetra-*t*-Bu)(catechol-CO_2H)], aniline derivative, and naphthalenediol, was considered. The equilibrium structure of the anatase TiO_2 NP was taken from an equilibrated MD simulation at 300 K by using the MA FF parameters [200-201,203]. It was shown that the nature of the photoabsorption process in the dye-TiO_2 NP can be understood in terms of orbital population dynamics occurring during photoabsorption (Fig. 36*b*) [200]. Fig. 36*c-d* shows that alizarin and coumarin C343 exhibited an indirect (type-I) mechanism for electron injection because no new absorption band was observed in the visible region upon adsorbing the dye onto the TiO_2 NP. The lowest-energy band suffers a redshift for the alizarin−NP, while coumarin C343 shows a slight shift to higher energies. The lack of energy shift in the case of C343 might be understood in terms of the weak electronic coupling between the excited states of the dye and the anatase NP [200].
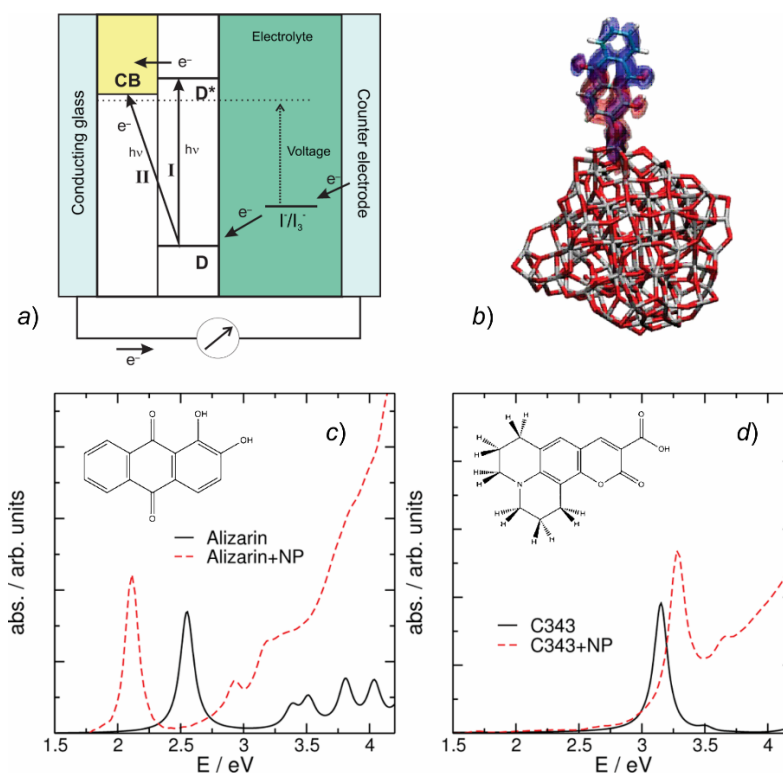
Figure 36. (*a*) Electron injection mechanisms type-I and type-II in a DSSC, where CB is a conduction band of the semiconductor and D is a dye. (*b*) A plot of the HOMO (*red*) and the LUMO (*blue*) of the alizarin−TiO_2 conjugate superimposed on the respective atomic structures. (*c-d*) Superposition of the optical spectra of the free dyes (*black lines*) and dyes anchored to the TiO_2 NP (*red lines*): alizarin (*c*), coumarin C343 (C343) (*d*). Adapted with permission from [200]. Copyright © 2012 American Chemical Society. (For interpretation of the references to color in this figure legend, the reader is referred to the Web version of this article.)

The proton transfer at a dopamine-functionalized TiO_2 interface was investigated by using dispersion-corrected hybrid DFT calculations and DFT tight-binding (DFTB) MD simulations [204]. The adsorption modes, patterns of growth, and configurations of dopamine on the anatase (101) TiO_2 surface were considered with reference to the binding archetype of catechol. It was found that at low cov-

erage, the isolated dopamine molecule prefers to bend toward the surface, coordinating the NH_2 group to a Ti_{5c} ion. Whereas, at high coverage, the packed molecules were succeeded in bending toward the surface only in some monolayer configurations so that a proton transfer from the surface to the ethyl-amino group occurred. It was suggested that improving the probability of dopamine molecules being free to bend toward the surface through thermodynamic versus kinetic growth conditions should lead to the formation of a monolayer of fully protonated dopamine molecules [204].

Self-assembly of organic molecules on semiconductor surfaces is of crucial importance in the performance of DSSC devices. Several computational works were focused on a strong tendency of organic dyes to form molecular aggregates on the TiO_2 surface [204-206].

The optical and electronic properties of dye aggregates of *p*-methyl red on a TiO_2 anatase (101) surface were considered as a function of aggregation order varying from a monomer up to pentameric dyes (Fig. 37) by using dispersion-corrected DFT calculations (PBE functional and ultrasoft pseudo-potentials) [205]. A progressive red-shifting accompanied by the intensity increase toward the visible region in UV−vis absorption spectra were observed from monomeric-to-tetrameric dyes. The calculated density of states (DOS) and partial DOS spectra reveal similar dye···TiO_2 nanocomposite conduction band characteristics; however, different valence band features were revealed. Associated molecular orbital distributions demonstrated dye-to-TiO_2 interfacial charge transfer in all studied aggregates.
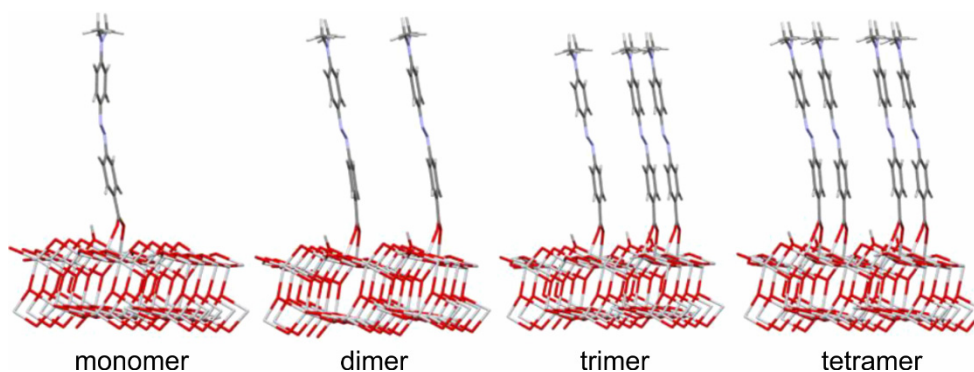
Figure 37. Optimized structural geometries of different adsorbed dye aggregates. Adapted with permission from [205]. Copyright © 2014 American Chemical Society.

Adsorption modes, dynamics, self-aggregation, and optical properties of an indoline D102 dye adsorbed on TiO_2 anatase (101) substrates were studied by reactive MD (ReaxFF) simulations combined with TD-DFT calculations [206]. The morphology and electronic properties of dye-sensitized heterogeneous interfaces were examined at an atomistic level. Extensive MD simulations of the adsorption of D102 dyes on medium/large size TiO_2 anatase slabs allowed to monitor a variety of dye binding modes. It was suggested that the main driving forces toward the formation of ordered surface aggregates of D102 dyes are π stacking and T-shaped interactions between the aromatic rings of the donor moiety of the dyes, as well as the tendency to maximize the anchoring points with the surface. The dye aggregates were found to be organized in domains, which are characterized by a different orientation of the packing units with a certain degree of short-to-medium range order [206].

Finally, at the end of this section, we suggest a few methodological conclusions from the results described above:

1) The results of the electronic structure calculations are insensitive to the geometry optimization method. The tight-binding DFT approach (DFTB) can be a realistic low-cost alternative to regular DFT geometry optimization.
2) The results of calculations are insensitive to the choice of basis set. Probably most of medium size contemporary basis sets (valence double-, triple ζ) can lead to similar results.
3) The results of electronic property calculations are sensitive to the choice of the DFT functional.
4) The TDDFT excited states calculations by using standard exchange-correlation functional (B3LYP) perform well only for local excitations. However, for the excitations with a significant charge-transfer character the CAM-B3LYP (or M06-2X, etc.) is preferable.

Ab initio MD Investigations

In the current section, we are briefly discussing the most interesting papers where *ab initio* MD simulation methods were predominately used for the theoretical investigation of the pristine TiO_2 fragments or TiO_2-based functional materials in the last two decades.

Ab initio (quantum or first principles) MD is the most powerful molecular modeling method for investigating the structure and dynamics of many-body systems in the framework of the condensed matter physics and computation quantum chemistry. The main idea underlying in any first principle MD method is to compute the true forces acting on the nuclei from proper electronic structure calculations that are performed "on the fly" as the MD trajectory is generated [207]. The three basic techniques are traditionally distinguished among an *ab initio* MD simulations: The first one is the conventional MD of nuclei using the quantum chemistry predicted Born-Oppenheimer (BO) potential energy surface (BOMD method). In the second MD technique, that was proposed by Car and Parrinello (CP), instead of solving the electronic structure problem at each new nuclear configuration, the so-called fictitious dynamics for the electronic orbitals (wave functions) is introduced that, as before, allows adiabatic motion of the nuclei (CPMD method) [208-209]. Both mentioned approaches deal with the ground state of an electronic sub-system. The third specific *ab initio* MD technique was designed for the solution of the more complicated non-adiabatic (NA) problems, such as electronic excitation and relaxation or particle collision and scattering (NA or Ehrenfest MD method) [210].

Earlier investigations of the photoinduced electron transfer from a molecular donor to the TiO_2 semiconductor acceptor, using the NAMD simulation method, were carried out in a series of works by Stier and Prezhdo [211-213]. The small systems under study are typically composed of dye-sensitized semiconductor nanomaterials, used in solar cells, photocatalysis, and photoelectrolysis. The electronic structure of a dye-semiconductor system and the adiabatic dynamics were simulated using BOMD, while the NA effects were incorporated by the quantum-classical mean-field approach that neglects the quantum effects of the ionic motion, in particular, the zero-point energy and decoherence effects. A novel procedure separating the NA and adiabatic electron transfer pathways (Fig. 38) was also developed. The simulation provided a detailed picture of the ET process.
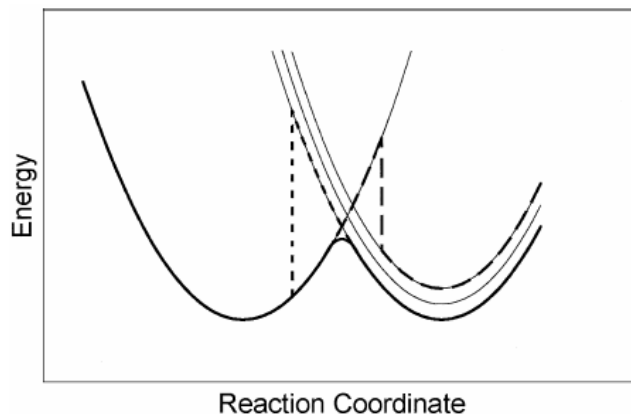
Figure 38. Adiabatic and NA pathways of electron transfer. In adiabatic electron transfer (*solid bold line*) the electron remains in the same adiabatic state throughout the reaction proceeding from the reactant state to the product state through the transition state. In NA electron transfer, the electron proceeds from the reactant state to the product state via a direct transition (*bold dotted* and *dashed lines*). Adapted from [211]. Copyright © 2002 WILEY-VCH Verlag GmbH & Co. KGaA, Weinheim.

It was initially assumed that ground and excited state ion dynamics are similar. So, the change in the quantum force due to the electronic photoexcitation could be neglected and the following analysis might be greatly simplified. An important result was that thermally driven adiabatic transfer is the dominant electron transfer mechanism. Compared to the earlier simulation at 50 K, the rate of NA transfer at 350 K remained almost unchanged, whereas the rate of adiabatic electron transfer increased substantially [211].

In the next two publications, the ultrafast dynamics of the photoinduced electron transfer process occurring between a model organic sensitizer molecule (isonicotinic acid) and a TiO_2 semiconductor surface was simulated and discussed in details (Fig. 39). The model used in simulation exhibited the

key features of the larger real systems studied before experimentally while providing a detailed simulation picture of the electron transfer mechanism [212-213].

Finally, the authors indicated that the NA electron transfer entirely dominated at short times and could occur due to the presence of the strong localized avoided crossing region, as well as the extended region of weaker NA coupling. Although the adiabatic electron transfer contribution accumulated more slowly, it approached that of the NA transfer pathway asymptotically. As a result, the simulation predicted a complex non-single-exponential time dependence of the electron transfer process [213].
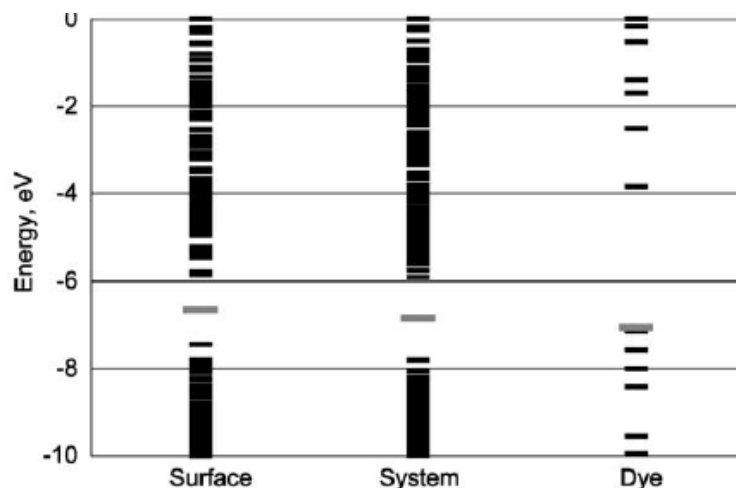
Figure 39. The Kohn–Sham orbital energies of the TiO_2 surface, the isolated dye, and the combined system. The longer gray line indicates the Fermi energy. The HOMO-LUMO gap of the dye equals 3.2 eV and is close to the 3.4 eV energy of the first excited state calculated by the TD-DFT calculations. Adapted from [213]. Copyright © 2003 Elsevier B.V. All rights reserved.

An interesting theoretical investigation in the field of phase transformation mechanisms from anatase to the TiO_2 nanosheets was carried out by Alvarez-Ramirez and Ruiz-Morales [214]. Several *ab initio* MD simulations with the non-self-consistent Harris functional (so-called non-self-consistent BOMD) including (*i*) the Γ-point approximation and (*ii*) the k-points were performed [214]. The three different size wire models of anatase with the periodic conditions along the (0, 1, 0) direction were used and also several different environmental conditions were investigated.

It was found the titanate-type structures are energetically favorable. The transformation (Fig. 40) was followed by monitoring the formation of four-coordinated oxygen atoms, which constituted the characteristic sequence of edge-sharing TiO_6 octahedrons of titanates. In addition, it was shown that the titanate-type structure could be transformed to anatase in a reversed mechanism. An essential factor in the transformation of the anatase-type sections to the TiO_6 octahedrons was the interaction of the (0, 0, ±1) surfaces of the anatase with positive counter ions, which stressed the surface, deforming it and promoting the transformation [214].

Outstanding NAMD investigation of the so-called "wet-electrons" on the TiO_2 surface was carried out by Prezhdo and coworkers [215]. Simulations directly mimicked real time-resolved experiments and revealed the nature of electron transfer in the "wet-electron" system. Earlier, the experimental and theoretical studies were done on the $TiO_2(110)/H_2O$ interface have shown a short-lived state around 2.4 eV above the Fermi level. The electron in this state was localized on the surface and was partially hydrated (Fig. 41). Therefore, it was named the "wet-electron". The time-resolved studies of the "wet-electrons" provide a fundamental understanding of the solvent role in the DSSC processes. The "wet-electron" state is higher in energy than the excited states of the majority of chromophores used in DSSC devices. Therefore, pristine "wet-electron" states are not directly involved in the photovoltaic processes [215].
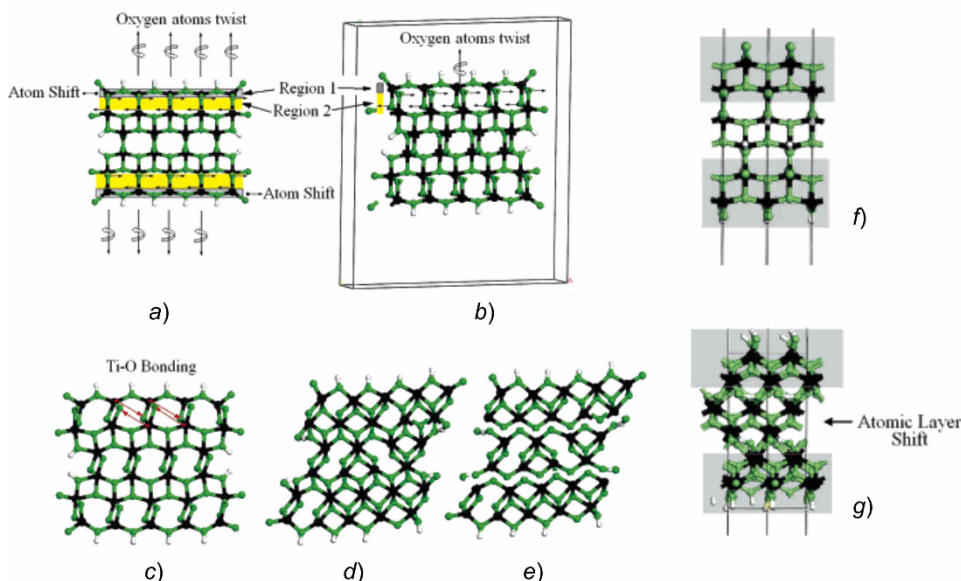
Figure 40. Schematic representation of the different stages in the mechanism of the phase transformation of anatase-to-lepidocrocite-type titanate. Panels *a* and *b* are initial configurations, where the initial atomic shifts and oxygen atom twisting are indicated. Panel *b* is a slightly rotated view of crystal shown in Panel *a*. (c) This panel shows the structure shifted and twisted, where the formation of tetra coordinated (T_h) oxygen atoms is indicated. (*d*) The crystal structure shown after the formation of the T_h oxygen atoms is distorted. Panel *e* is the same as Panel *d*, where the internal bonds were deleted to show that lepidocrocite-type titanate layers are formed. Panels *f* and *g* correspond to side views of the initial anatase structure and the final lepidocrocite structure, respectively. The internal layer dislocation can be observed In Panel *g*. Adapted with permission from [214]. Copyright © 2007, American Chemical Society.

It was shown that thermal phonon motions induced a large fluctuation of the "wet-electron" state energy, generated frequent crossings of the donor and acceptor states, and drove the adiabatic mechanism. The rapid phonon-assisted NA tunneling from the "wet-electron" state to the TiO_2 surface was facilitated by the strong water-TiO_2 electronic interaction. Besides, it was demonstrated that the motions of H_2O molecules had a greater effect on the electron transfer dynamics than the hydroxyl vibrations [215].
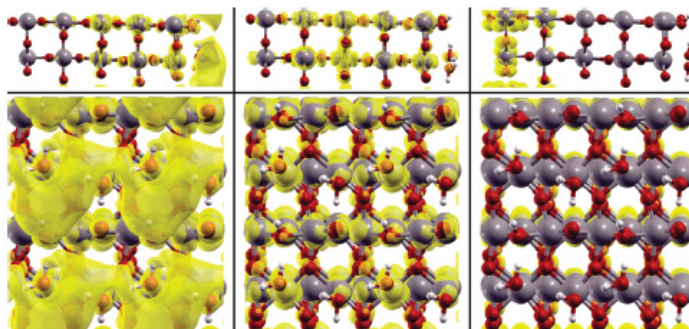
Figure 41. Charge densities for the "wet-electron" state (*left*), the surface state (*middle*), and the bulk state (*right*) of the "wet-electron" system. The charge is transferred sequentially from the "wet-electron" state through the surface state to the bulk state. The large delocalization of charge around the water molecules in the "wet-electron" state is shown, which is due to the dangling hydrogen atoms that help stabilize the electron. Adapted with permission from [215]. Copyright © 2009, American Chemical Society

In order to better understand the electron-hole relaxation of nano-scale TiO_2 structures, it was important to start with an understanding of TiO_2 synthesis building blocks. Such investigation was carried out by Vogel and Kilin [216], in which the $Ti(OH)_4$ complex with tetrahedral coordination was examined. To simulate the electronic properties of the Ti^{IV} ion in solution, the model was surrounded with explicit 27 H_2O molecules (Fig. 42). The model was explored by means of standard DFT BOMD

followed by NA electron dynamics computed with a reduced density matrix approach combined with "on-the-fly coupling" [216].
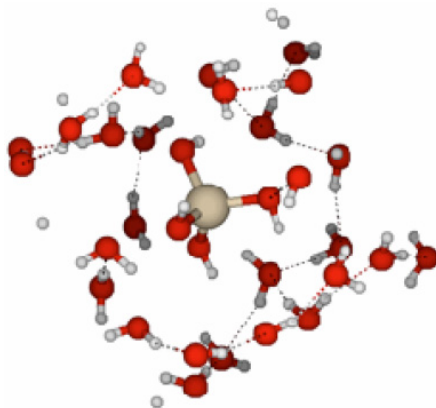
Figure 42. The optimized geometry of the studied Ti(OH)$_4$ model placed in a periodic box of water molecules. The model consists of three elements represented by colored spheres: titanium (*large* and *gray*), hydrogens (*small* and *white*), and oxygens (*small* and *dark*). The *black dotted lines* represent the occurrence of hydrogen bonds. Adopted from [216]. Copyright ©: Materials Research Society 2014. (For interpretation of the references to color in this figure legend, the reader is referred to the Web version of this article.)

According to the MD simulation results [216], the titanium ion is affected by coordination to hydroxyl groups and an explicitly modeled water environment in three ways: First, the crystal field environment stabilizes the oxidation state. Second, the crystal field provides splitting of the titanium ion *d*-orbitals, which is responsible for the density of states in the conduction band range of energies. Third, thermal motion of near hydroxyl ligands and water coordination sphere are responsible for the non-radiative relaxation mechanisms: a photoexcitation in the solvated titanium ion is followed by the energy dissipation from electronic degrees of freedom to thermal motion. Thus, it was found that electrons dissipate energy slower than holes [216].

Chemical and physical adsorption of water on small-sized wet TiO$_2$ nanoparticles was investigated by *ab initio* MD simulations [217]. The wetting behavior of (TiO$_2$)$_{24}$·nH$_2$O (n=0, 1, 3, 8, 15, 30) was studied as a function of water content, ranging from dry nanoparticles to wet nanoparticles with monolayer coverage of water. The simulations were performed with the mixed Gaussian and plane-wave (GPW) method, as implemented in the CP2K code. It was found that the surface reactivity was shown to be a concave function of water content and driven by surface defects [217]. It was suggested that the local coordination number at the defect of TiO$_2$ NPs was identified as the key factor in deciding whether water adsorption proceeds through dissociation or physisorption on the surface.

Hybrid QM-MD Simulations

In the last decade, hydride QM-MM calculations utilizing the DFTB approximation have become an attractive alternative to conventional non-empirical first principle *ab initio* MD simulations. Several examples of such studied are summarized below.

Small TiO$_2$ NPs (anatase, rutile, brookite) have been studied by *ab initio* MD simulations to elucidate chemical and physical adsorption of water molecules on the TiO$_2$–water interface, ranging from dry NPs up to monolayer solvated NPs [217]. QM-MM simulations have been used to model the adsorption of insulin on TiO$_2$ (100) surfaces [218]. Recently, a multistep and multiscale investigation based on hybrid DFT, DFT tight-binding (DFTB), and QM-MM calculations have been applied to consider solvation behavior of curved TiO$_2$-NPs, ranging from vacuum, multilayered solvation and up to the bulk water environment, resulting in an overall stoichiometry of (TiO$_2$)$_{223}$·8958H$_2$O (Fig. 43) [219].

Recently, DFT-based BOMD was carried out by Byrne and English to investigate the effect with which the choice of exchange-correlational functional has on the structural properties of a [BMIM]$^+$[NTF$_2$]$^-$ RTIL solvating an N719 sensitizing dye, adsorbed onto the anatase TiO$_2$(101) surface [220]. The systematic study of an N719 dye, non-solvated and solvated by RTILs, was performed

by comparing the widely used BLYP and PBE functionals, which were utilized with and without D3 dispersion corrections by Grimme [220].
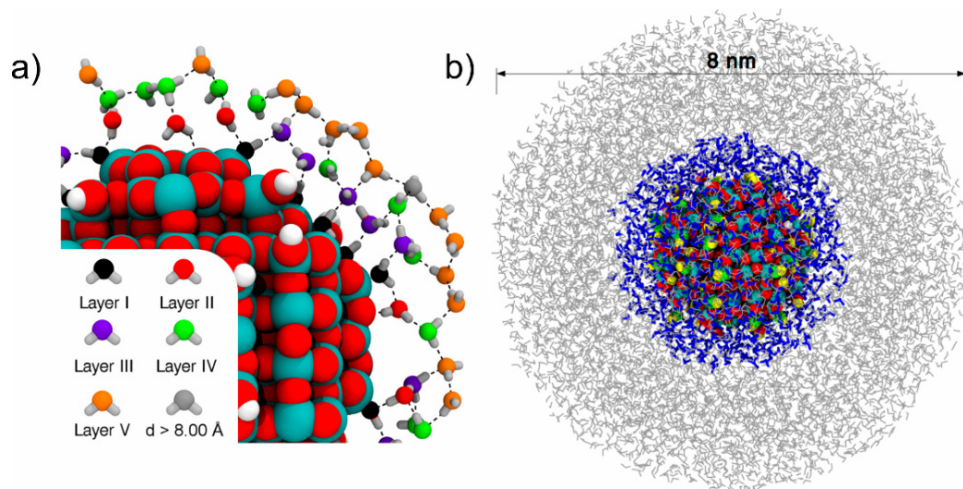
Figure 43. (*a*) A snapshot of the water multilayer on TiO$_2$-NP, as obtained from the DFTB MD simulation. (*b*) Representation of TiO$_2$-NP solvated with a DFTB water multilayer (*in blue*) enclosed in a water droplet flexible (SPC/Fw model) (*in gray*). Adapted with permission from [219]. Copyright © 2018 American Chemical Society. (For interpretation of the references to color in this figure legend, the reader is referred to the Web version of this article.)

The above results show that neither the addition of dispersion corrections nor solvation by the strongly ionic solvent has any noticeable effect on the anatase surface structure. The structure of the surface was stable throughout the MD simulations, as is the carbon backbone of an N719 dye with neither group showing any real differences in their structure upon change of the DFT functional. However, the pair distribution functions (PDFs) for some of the carboxylate oxygens showed that the results obtained with the PBE functional led to some structural peaks shifts by 0.01 nm closer than their position derived by the BLYP functional [220]. The metal complex at the center of the dye was also largely unaffected by utilization of the dispersion correction, variations in the functionals or the presence of the solvent. The structure of the dye was found to be essentially unaffected by solvation with the bipyridine rings and anchoring groups retained their rigid geometry. A comparison of the PDFs, derived from the BLYP and PBE functionals, showed the structure of the anions and cations to be quite similar. On the other hand, some deviation was found between the results of the BLYP-D3 and the PBE-D3 so that the cations and anions are seen to be slightly closer to each other in the case of the PBE-D3 calculation by about 0.02 nm. Moreover, it was suggested that the dispersion corrections also introduced the pronounced effect of an orientational alignment in the liquid, the phenomenon which would be expected for a real liquid [220].

Stable structures and photoexcitation character of adsorption of an N749 dye to TiO$_2$ anatase (101) interface, solvated by explicit acetonitrile (ACN) molecules were considered by DFT-MD simulations [221]. It was found that the adsorption of an N749 dye via its deprotonated carboxylate two anchors (type *d2*) was the most stable at the interface (Fig. 44*a*). However, the adsorption mode with the one protonated carboxyl anchor (type *p1*) was observed to be at the average energy only slightly higher than that of type *d2* (Fig. 44*b*).

Other possible anchoring modes, shown schematically in Fig. 44*c-e* were all higher in energy as compared to those of *p1* and *d2*, respectively. It was suggested that, under equilibrium, the mode *p1* might still coexist with the mode *d2* [221]. These findings were in contrast with the high stability calculated for the mode p1 *in vacuo*. It was proposed that some stabilization of the mode *d2* could be caused by inhomogeneous charge distribution and anchor fluctuation enhanced by ACN solution (Fig. 44*f-g*). The calculated projected densities of states and the photoabsorption spectra supported the conclusions that the mode *d2* has the larger driving force of the electron injection from an N749 dye into the TiO$_2$, whereas the characteristic sensitizer photoabsorption in the wavelength region over 800 nm, was mainly attributed to the mode *p1* even in the bulk ACN solution. It was concluded that the better

performance of a N749 dye in DSSC devices can be regionalized in terms of the co-sensitizer framework of the adsorption modes *d2* and *p1*, respectively [197-198,221].
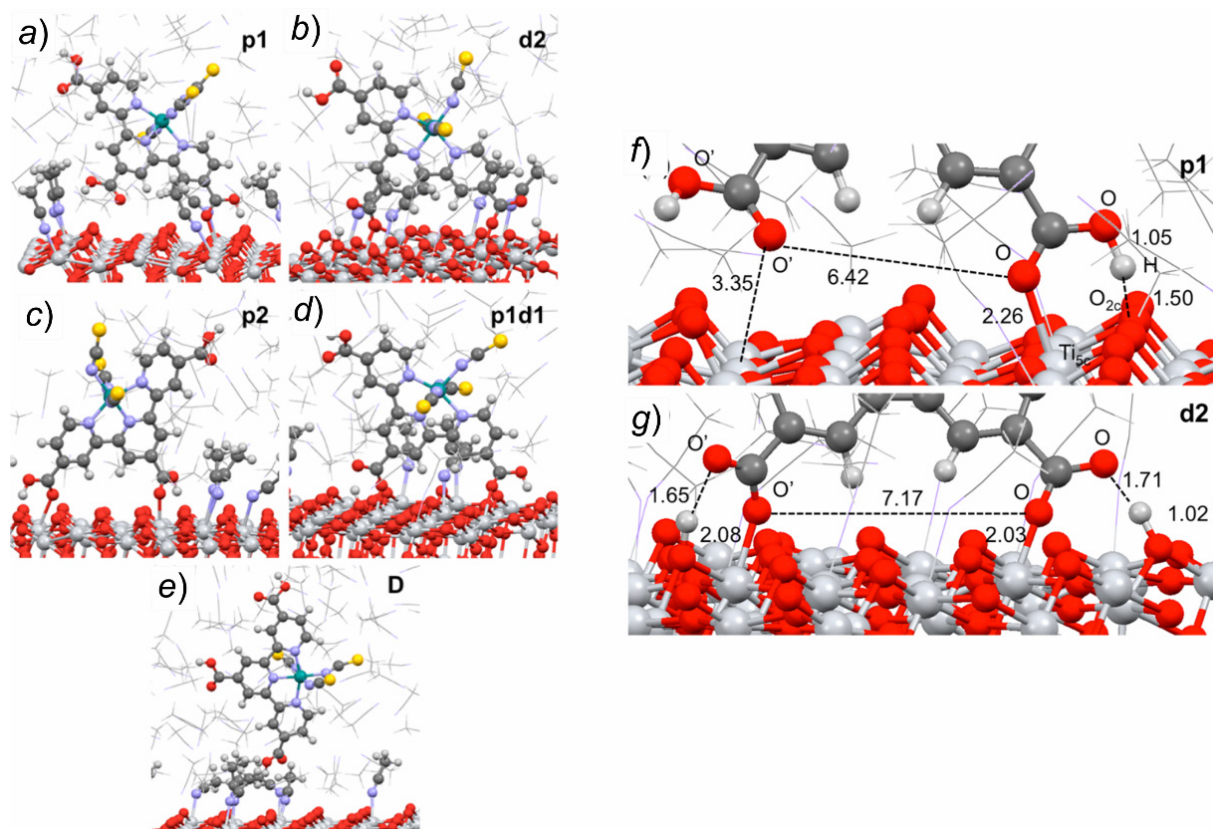
Figure 44. Representative snapshots of the equilibrium trajectories of adsorption of a N749 dye to TiO$_2$ anatase (101)/acetonitrile (ACN) interfaces: (*a*) adsorption with one protonated carboxyl anchor (−COOH), labeled as *p1*, (b) adsorption with two deprotonated (−COO$^-$) anchors, labeled as *d2*, (c) adsorption with two protonated anchors (label *p2*), (d) adsorption with one protonated and one deprotonated anchors (label *p1d1*), and (e) the desorbed state, assigned as *D*. Each trajectory was obtained with DFT-MD simulation with different initial configuration of the dye, which was optimized on the vacuum surface, in advance. (*f-g*) Average structures and distances (*in angstroms*) of the characteristic atoms near the interface in (*f*) the *p1* equilibrium state and (*g*) the *d2* state, respectively. Adapted with permission from [221]. Copyright © 2014, American Chemical Society.

Small TiO$_2$ NPs, functionalized with a supramolecular complex consisting of an entirely organic naphthalene-diimide (NDI) dye covalently bound to a mononuclear Ru-based water oxidation catalyst (Fig. 45*a*) were studied by *ab initio* MD simulations to elucidate the mechanistic insight and microscopic details of water oxidation at the photoanode induced by visible light absorption [222]. The MD nuclear trajectory was calculated through ab initio MD by using the Car−Parrinello MD (CPMD) code. The orthorhombic cell, containing a two-layer anatase slab (TiO$_2$)$_{32}$ functionalized with the NDI1 chromophore, was used together with periodic boundary conditions to model the TiO$_2$ surface. The fast photoinduced electron injection from the NDI into the semiconductor was observed, which provided the driving force for the activation of the Ru catalyst (Fig. 45*b*). The explicit description of the water environment was utilized to elucidate the sub-picosecond time-scale and the nature of the proton-coupled electron transfer of the catalytic reaction path. It was suggested that the explicit water treatment was essential to determine the proton diffusion channel and the free energy change along with the reaction [222].

The above photochemical reaction simulations are a promising example for the computational design and DSSC device optimization with an aim to explore the effect of different anchoring groups, which allow tuning the driving force for the subsequent steps of the catalytic water photo-oxidation cycle and reducing the charge recombination rate [223-225].
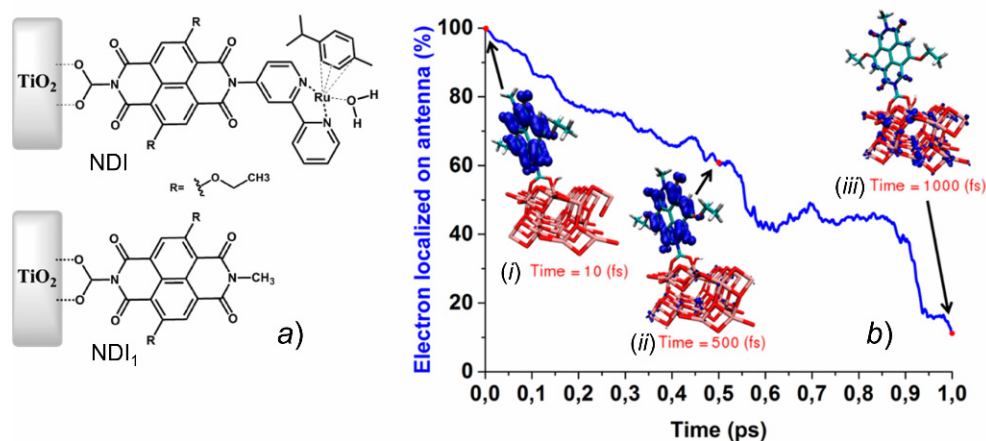
Figure 45. (*a*) Schematic representation of the studied photoanode (NDI) composed of the acceptor semiconductor (TiO$_2$), the molecular chromophore NDI, and the Ru-based water oxidation catalyst; (NDI$_1$) chromophore-semiconductor subsystem employed for the photoinduced electron injection MD simulation. (*b*) Electron injection profile obtained through the time-dependent population analysis of the wavepacket projected only over the dye-TiO$_2$ conjugate (*solid line*). The insets show the distribution of the total wavepacket after initialization (*i*), and along with the time evolution of the MD trajectory (*ii* and *iii*). Adapted with permission from [222]. Copyright © 2016, American Chemical Society.

Conclusions and Outlook

The review describes recent advances in theoretical studies of TiO$_2$ nanomaterials. Particular attention is focused on the MD simulation approaches that are essential for the modeling of bulk TiO$_2$, its interfaces with aqueous and non-aqueous environments, as well as large-scale nanoparticles and their aggregates. Starting from the earlier FF model by Matsui and Akaogi (MA) [14], rapid progress in computational modeling of TiO$_2$ nanomaterials resulted in the development of well-validated FFs for a broad range of TiO$_2$ nanomaterials, ranging from small perfect clusters and up to water/TiO$_2$ interfaces. The applicability of MD simulation tools has currently extended up to about 100 nm size and microseconds, and can further be scaled up by coarse-grain and finite element models to the range of micrometers. However, the critical overview of recent computational models suggested for modeling partially hydroxylated TiO$_2$ surfaces reveals that the existing MA approach still requires further improvements and validation. The main limitation of the MA force-field, developed originally for bulk TiO$_2$, is that it utilizes only two types of atoms, such as Ti and O. However, in realistic TiO$_2$ nanostructures, these atoms are characterized by different coordination numbers so that they can be classified into inner-bulk and outer-surface-exposed atoms. The latter can be further divided into subgroups of corner, edge, or side atoms. Recent *ab initio* MD studies demonstrated that indeed these atoms bear different partial charges and, hence, they should be represented by different atom types in an empirical force field [217]. The different atoms types for Ti and O have already been implemented in some MD simulation studies of TiO$_2$ nanostructures [19,32,84]. Moreover, the development of computational models for some realistic systems with the simultaneous presence of several crystalline facets (100, 110, 111) or different phases, such as rutile and anatase, will enable modeling the adsorption phenomena that may take place at the grain boundary and at their common interface with the outer environment [226].

The understanding of the mechanisms that govern the interaction of biological systems with inorganic materials remains a challenge for both fundamental and applied material science [227-228]. The protein adsorption modulates the formation of biofilms onto surfaces, which is essential for medical implants and dental technologies. The interaction of TiO$_2$ nanomaterials with biomacromolecules is crucial to further response of cells to foreign inorganic materials, such as engineered implants or accidentally entrapped inorganic nanoparticles. Therefore, detailed knowledge of the TiO$_2$/biological interfaces is required for the design of new biocompatible materials. MD simulations of conformation equilibria of biomolecules at perfect, defect-free, and curved interfaces have provided insight into the mechanism, specific recognition, and sequence-relation suggestions to understand their adsorption, binding, and assembly. However, due to the complexity of the configuration space, it remains challenging to explore because of the large number of possible conformations of biomacromolecules.

Therefore, the critical review of MD studies in this field reveals that free, unbiased MD sampling of protein binding and adsorption onto TiO_2 may not guarantee finding of proper binding modes so that the development of some innovative sampling techniques is required. Some recent studies report new promising approaches in this direction, such as the potential mean-force calculations, free-energy umbrella sampling, and replica-exchange MD simulations [229].

In the last decade, significant progress has been achieved in quantum chemical calculations of the structural, electronic, and optical properties of TiO_2 materials in the context of their use as components of dye-sensitized solar cells (DSSC). Successes, failures, and challenges of quantum chemical, DFT, and TDDFT computational methods of dye-TiO_2 conjugates have been critically analyzed elsewhere [1,197,230]. To summarize, we found that the electronic structure calculations are little sensitive to the basis set and DFT functionals used for geometry optimization. Moreover, the tight-binding DFT approach (DFTB) can provide a low-cost alternative to regular CPU-expensive DFT geometry optimization. However, it was found that the results of electronic property calculations are crucially sensitive to the choice of the DFT functional [165,197]. The presented DFT/TDDFT computational models, employing conventional hybrid (B3LYP) and range-separated functional and based on the use of large TiO_2 clusters, PCM-continuum solvation models, allows one to reproduce to a reasonable degree of accuracy the electronic and optical properties of dye-TiO_2 systems. However, for highly conjugated organic dyes, which are often characterized by a high degree of charge-transfer excited states, specifically tailored exchange-correlation functionals, such as CAM-B3LYP or M06-2X, are required [197]. Some efforts have already devoted to solving the shortcomings of current TDDFT methodologies for dye-TiO_2 systems [231].

Finally, our review sheds light on the progress and development of modern computational tools, combining classical FF modeling and high-level *ab initio* MD simulations, which may assist the molecular engineering and rational design of more efficient dye sensitizers and deeper understanding of the electron transfer dynamics in dye-sensitized solar cells.

Acknowledgments

References

1. Bai Y., Mora-Seró I., De Angelis F., Bisquert J., Wang P. Titanium dioxide nanomaterials for photovoltaic applications. *Chem. Rev.* **2014,** *114* (19), 10095-10130.
2. Kapilashrami M., Zhang Y., Liu Y.-S., Hagfeldt A., Guo J. Probing the optical property and electronic structure of TiO_2 nanomaterials for renewable energy applications. *Chem. Rev.* **2014,** *114* (19), 9662-9707.
3. Zhang H., Banfield J. F. Structural characteristics and mechanical and thermodynamic properties of nanocrystalline TiO_2. *Chem. Rev.* **2014,** *114* (19), 9613-9644.
4. Fattakhova-Rohlfing D., Zaleska A., Bein T. Three-dimensional titanium dioxide nanomaterials. *Chem. Rev.* **2014,** *114* (19), 9487-9558.
5. Momma K., Izumi F. VESTA 3 for three-dimensional visualization of crystal, volumetric and morphology data. *J. Appl. Crystall.* **2011,** *44* (6), 1272-1276.
6. YazdanYar A., Aschauer U., Bowen P. Interaction of biologically relevant ions and organic molecules with titanium oxide (rutile) surfaces: A review on molecular dynamics studies. *Colloids Surf. B* **2018,** *161,* 563-577.
7. Liu X., Chu P. K., Ding C. Surface modification of titanium, titanium alloys, and related materials for biomedical applications. *Mater. Sci. Engineer. Reports* **2004,** *47* (3), 49-121.
8. Silva-Bermudez P., Rodil S. E. An overview of protein adsorption on metal oxide coatings for biomedical implants. *Surf. Coatings Technol.* **2013,** *233,* 147-158.
9. Liu K., Cao M., Fujishima A., Jiang L. Bio-inspired titanium dioxide materials with special wettability and their applications. *Chem. Rev.* **2014,** *114* (19), 10044-10094.

10. Casalini T., Limongelli V., Schmutz M., Som C., Jordan O., Wick P., Borchard G., Perale G. Molecular modeling for nanomaterial–biology interactions: Opportunities, challenges, and perspectives. *Frontiers Bioengineer. Biotech.* **2019,** *7,* art. no. 268.

11. Rajh T., Dimitrijevic N. M., Bissonnette M., Koritarov T., Konda V. Titanium dioxide in the service of the biomedical revolution. *Chem. Rev.* **2014,** *114* (19), 10177-10216.

12. Akimov A. V., Neukirch A. J., Prezhdo O. V. Theoretical insights into photoinduced charge transfer and catalysis at oxide interfaces. *Chem. Rev.* **2013,** *113* (6), 4496-4565.

13. Wang Q., Wang M.-h., Wang K.-f., Liu Y., Zhang H.-p., Lu X., Zhang X.-D. Computer simulation of biomolecule–biomaterial interactions at surfaces and interfaces. *Biomedical Materials* **2015,** *10* (3), art. no. 032001.

14. Matsui M., Akaogi M. Molecular dynamics simulation of the structural and physical properties of the four polymorphs of TiO_2. *Mol. Simul.* **1991,** *6* (4-6), 239-244.

15. Limo M. J., Sola-Rabada A., Boix E., Thota V., Westcott Z. C., Puddu V., Perry C. C. Interactions between metal oxides and biomolecules: From fundamental understanding to applications. *Chem. Rev.* **2018,** *118* (22), 11118-11193.

16. Mao Q., Ren Y., Luo K. H., Li S. Sintering-induced phase transformation of nanoparticles: A molecular dynamics study. *J. Phys. Chem. C* **2015,** *119* (51), 28631-28639.

17. Collins D. R., Smith W., Harrison N. M., Forester T. R. Molecular dynamics study of TiO_2 microclusters. *J. Mater. Chem.* **1996,** *6* (8), 1385-1390.

18. R. Collins D., Smith W., M. Harrison N., R. Forester T. Molecular dynamics study of the high temperature fusion of TiO_2 nanoclusters. *J. Mater. Chem.* **1997,** *7* (12), 2543-2546.

19. Naicker P. K., Cummings P. T., Zhang H., Banfield J. F. Characterization of titanium dioxide nanoparticles using molecular dynamics simulations. *J. Phys. Chem. B* **2005,** *109* (32), 15243-15249.

20. Koparde V. N., Cummings P. T. Molecular dynamics simulation of titanium dioxide nanoparticle sintering. *J. Phys. Chem. B* **2005,** *109* (51), 24280-24287.

21. De Angelis F., Di Valentin C., Fantacci S., Vittadini A., Selloni A. Theoretical studies on anatase and less common TiO_2 phases: Bulk, surfaces, and nanomaterials. *Chem. Rev.* **2014,** *114* (19), 9708-9753.

22. Koparde V. N., Cummings P. T. Phase transformations during sintering of titania nanoparticles. *ACS Nano* **2008,** *2* (8), 1620-1624.

23. Buesser B., Gröhn A. J., Pratsinis S. E. Sintering rate and mechanism of TiO_2 nanoparticles by molecular dynamics. *J. Phys. Chem. C* **2011,** *115* (22), 11030-11035.

24. Alimohammadi M., Fichthorn K. A. Molecular dynamics simulation of the aggregation of titanium dioxide nanocrystals: Preferential alignment. *Nano Lett.* **2009,** *9* (12), 4198-4203.

25. Filyukov D. V., Brodskaya E. N., Piotrovskaya E. M., de Leeuw S. W. Molecular-dynamics simulation of nanoclusters of crystal modifications of titanium dioxide. *Rus. J. Gen. Chem.* **2007,** *77* (1), 10-16.

26. Oliver P., Watson G., Kelsey E., Parker S. Atomistic simulation of the surface structure of TiO_2 polymorphs rutile and anatase. *J. Mater. Chem.* **1997,** *7* 563-568.

27. Swamy V., Gale J. D., Dubrovinsky L. S. Atomistic simulation of the crystal structures and bulk moduli of TiO_2 polymorphs. *J. Phys. Chem. Solids* **2001,** *62* (5), 887-895.

28. Bandura A. V., Kubicki J. D. Derivation of force field parameters for TiO_2−H_2O systems from *ab initio* calculations. *J. Phys. Chem. B* **2003,** *107* (40), 11072-11081.

29. Bandura A. V., Sykes D. G., Shapovalov V., Troung T. N., Kubicki J. D., Evarestov R. A. Adsorption of water on the TiO_2 (rutile) (110) surface: A comparison of periodic and embedded cluster calculations. *J. Phys. Chem. B* **2004,** *108* (23), 7844-7853.

30. Carravetta V., Monti S. Peptide−TiO_2 surface interaction in solution by *ab initio* and molecular dynamics simulations. *J. Phys. Chem. B* **2006,** *110* (12), 6160-6169.

31. Skelton A. A., Liang T., Walsh T. R. Interplay of sequence, conformation, and binding at the peptide−titania interface as mediated by water. *ACS Appl. Mater. Interfaces.* **2009,** *1* (7), 1482-1491.

32. Předota M., Bandura A. V., Cummings P. T., Kubicki J. D., Wesolowski D. J., Chialvo A. A., Machesky M. L. Electric double layer at the rutile (110) surface. 1. Structure of surfaces and

interfacial water from molecular dynamics by use of *ab initio* potentials. *J. Phys. Chem. B* **2004,** *108* (32), 12049-12060.

33. Předota M., Zhang Z., Fenter P., Wesolowski D. J., Cummings P. T. Electric double layer at the rutile (110) surface. 2. Adsorption of ions from molecular dynamics and X-ray experiments. *J. Phys. Chem. B* **2004,** *108* (32), 12061-12072.

34. Alimohammadi M., Fichthorn K. A. A force field for the interaction of water with TiO$_2$ surfaces. *J. Phys. Chem. C* **2011,** *115* (49), 24206-24214.

35. Foroutan M., Darvishi M., Mahmood Fatemi S., Hamideh Babazadeh K. Water chain formation on rutile TiO$_2$ (110) nanocrystal: A molecular dynamics simulation approach. *J. Mol. Liq.* **2018,** *250,* 344-352.

36. Jorgensen W. L., Chandrasekhar J., Madura J. D., Impey R. W., Klein M. L. Comparison of simple potential functions for simulating liquid water. *J. Chem. Phys.* **1983,** *79* (2), 926-935.

37. Schneider J., Ciacchi L. C. A classical potential to model the adsorption of biological molecules on oxidized titanium surfaces. *J. Chem. Theory Comput.* **2011,** *7* (2), 473-484.

38. Skelton A. A., Walsh T. R. Interaction of liquid water with the rutile TiO$_2$ (110) surface. *Mol. Simul.* **2007,** *33* (4-5), 379-389.

39. Kavathekar R. S., Dev P., English N. J., MacElroy J. M. D. Molecular dynamics study of water in contact with the TiO$_2$ rutile-110, 100, 101, 001 and anatase-101, 001 surface. *Mol. Phys.* **2011,** *109* (13), 1649-1656.

40. Kavathekar R. S., English N. J., MacElroy J. M. D. Spatial distribution of adsorbed water layers at the TiO$_2$ rutile and anatase interfaces. *Chem. Phys. Lett.* **2012,** *554,* 102-106.

41. English N. J. Dynamical properties of physically adsorbed water molecules at the TiO$_2$ rutile-(110) surface. *Chem. Phys. Lett.* **2013,** *583,* 125-130.

42. Köppen S., Langel W. Simulation of the interface of (100) rutile with aqueous ionic solution. *Surf. Sci.* **2006,** *600* (10), 2040-2050.

43. Senftle T. P., Hong S., Islam M. M., Kylasa S. B., Zheng Y., Shin Y. K., Junkermeier C., Engel-Herbert R., Janik M. J., Aktulga H. M., Verstraelen T., Grama A., van Duin A. C. T. The ReaxFF reactive force-field: Development, applications and future directions. *NPJ: Comput. Mater.* **2016,** *2* (1), art. no. 15011.

44. Monti S., Li C., Ågren H., Carravetta V. Dropping a droplet of cysteine molecules on a rutile (110) interface: Reactive versus nonreactive classical molecular dynamics simulations. *J. Phys. Chem. C* **2015,** *119* (12), 6703-6712.

45. Futera Z., English N. J. Exploring rutile (110) and anatase (101) TiO$_2$ water interfaces by reactive force-field simulations. *J. Phys. Chem. C* **2017,** *121* (12), 6701-6711.

46. Kim S.-Y., Kumar N., Persson P., Sofo J., van Duin A. C. T., Kubicki J. D. Development of a ReaxFF reactive force field for titanium dioxide/water systems. *Langmuir* **2013,** *29* (25), 7838-7846.

47. Nakamura H., Ohto T., Nagata Y. Polarizable site charge model at liquid/solid interfaces for describing surface polarity: Application to structure and molecular dynamics of water/rutile TiO$_2$ (110) interface. *J. Chem. Theory Comput.* **2013,** *9* (2), 1193-1201.

48. Morita A., Kato S. *Ab initio* molecular orbital theory on intramolecular charge polarization: Effect of hydrogen abstraction on the charge sensitivity of aromatic and nonaromatic species. *J. Am. Chem. Soc.* **1997,** *119* (17), 4021-4032.

49. Morita A., Kato S. Molecular dynamics simulation with the charge response kernel: Diffusion dynamics of pyrazine and pyrazinyl radical in methanol. *J. Chem. Phys.* **1998,** *108* (16), 6809-6818.

50. Isegawa M., Kato S. Polarizable force field for protein with charge response kernel. *J. Chem. Theory Comput.* **2009,** *5* (10), 2809-2821.

51. Ohto T., Mishra A., Yoshimune S., Nakamura H., Bonn M., Nagata Y. Influence of surface polarity on water dynamics at the water/rutile TiO$_2$(110) interface. *J. Phys.: Condens. Matter* **2014,** *26* (24), art. no. 244102.

52. Hosseinpour S., Tang F., Wang F., Livingstone R. A., Schlegel S. J., Ohto T., Bonn M., Nagata Y., Backus E. H. G. Chemisorbed and physisorbed water at the TiO$_2$/water interface. *J. Phys. Chem. Lett.* **2017,** *8* (10), 2195-2199.

53. Solute ions at ice/water interface. In *Ionic soft matter: Modern Trends in Theory and Applications*, Henderson, D.; Holovko, M.; Trokhymchuk, A., Eds. Springer Netherlands: Dordrecht, 2005; 418 p.

54. Bryk T., Haymet A. D. J. Ice 1h/water interface of the SPC/E model: Molecular dynamics simulations of the equilibrium basal and prism interfaces. *J. Chem. Phys.* **2002,** *117* (22), 10258-10268.

55. Seitsonen A. P., Bryk T. Melting temperature of water: DFT-based molecular dynamics simulations with D3 dispersion correction. *Phys. Rev. B* **2016,** *94* (18), art. no. 184111.

56. González Solveyra E., de la Llave E., Molinero V., Soler-Illia G. J. A. A., Scherlis D. A. Structure, dynamics, and phase behavior of water in TiO_2 nanopores. *J. Phys. Chem. C* **2013,** *117* (7), 3330-3342.

57. Wei M.-J., Zhou J., Lu X., Zhu Y., Liu W., Lu L., Zhang L. Diffusion of water molecules confined in slits of rutile TiO_2(110) and graphite(0001). *Fluid Phase Equilibria* **2011,** *302* (1), 316-320.

58. Zhu Y., Zhang Y., Shi Y., Lu X., Li J., Lu L. Lubrication behavior of water molecules confined in TiO_2 nanoslits: A molecular dynamics study. *J. Chem. Eng. Data* **2016,** *61* (12), 4023-4030.

59. Cao W., Lu L., Huang L., Dong Y., Lu X. Molecular behavior of water on titanium dioxide nanotubes: A molecular dynamics simulation study. *J. Chem. Eng. Data* **2016,** *61* (12), 4131-4138.

60. Zeydabadi-Nejad I., Zolfaghari N., Mosavi-Mashhadi M., Baniassadi M. Exceptional behavior of anatase TiO_2 nanotubes in axial loading: A molecular dynamics study of the effect of surface wrinkles. *Comput. Mater. Sci.* **2019,** *158,* 307-314.

61. Papavasileiou K. D., Makrodimitri Z. A., Peristeras L. D., Chen J., van der Laan G. P., Rudra I., Kalantar A., Economou I. G. Molecular simulation of *n*-octacosane–water mixture in titania nanopores at elevated temperature and pressure. *J. Phys. Chem. C* **2016,** *120* (43), 24743-24753.

62. Utesch T., Daminelli G., Mroginski M. A. Molecular dynamics simulations of the adsorption of bone morphogenetic protein-2 on surfaces with medical relevance. *Langmuir* **2011,** *27* (21), 13144-13153.

63. Mancardi G., Hernandez Tamargo C., Terranova U., de Leeuw N. H. Calcium phosphate deposition on planar and stepped (101) surfaces of anatase TiO_2: Introducing an interatomic potential for the TiO_2/Ca-PO_4/water interface. *Langmuir* **2018,** *34* (34), 10144-10152.

64. Zheng T., Wu C., Zhang Y., Chen M., Cummings P. T. Molecular investigation of the initial nucleation of calcium phosphate on TiO_2 substrate: The effects of surface nanotopographies. *Cryst. Growth Des.* **2018,** *18* (6), 3283-3290.

65. Zheng T., Wu C., Chen M., Zhang Y., Cummings P. T. Molecular mechanics of the cooperative adsorption of a Pro-Hyp-Gly tripeptide on a hydroxylated rutile TiO_2(110) surface mediated by calcium ions. *Phys. Chem. Chem. Phys.* **2016,** *18* (29), 19757-19764.

66. Monti S., Walsh T. R. Free energy calculations of the adsorption of amino acid analogues at the aqueous titania interface. *J. Phys. Chem. C* **2010,** *114* (50), 22197-22206.

67. Sushko M. L., Gal A. Y., Shluger A. L. Interaction of organic molecules with the TiO_2 (110) surface: *Ab inito* calculations and classical force fields. *J. Phys. Chem. B* **2006,** *110* (10), 4853-4862.

68. Yang L., Tunega D., Xu L., Govind N., Sun R., Taylor R., Lischka H., DeJong W. A., Hase W. L. Comparison of cluster, slab, and analytic potential models for the dimethyl methylphosphonate (DMMP)/TiO_2(110) intermolecular interaction. *J. Phys. Chem. C* **2013,** *117* (34), 17613-17622.

69. Hamad S., Sánchez-Valencia J. R., Barranco A., Mejías J. A., González-Elipe A. R. Molecular dynamics simulation of the effect of pH on the adsorption of rhodamine laser dyes on TiO_2 hydroxylated surfaces. *Mol. Simul.* **2009,** *35* (12-13), 1140-1151.

70. Fortunelli A., Monti S. Simulations of lipid adsorption on TiO_2 surfaces in solution. *Langmuir* **2008,** *24* (18), 10145-10154.

71. Předota M., Vlček L. Comment on parts 1 and 2 of the series "electric double layer at the rutile (110) surface". *J. Phys. Chem. B* **2007,** *111* (5), 1245-1247.

72. Předota M., Cummings P. T., Wesolowski D. J. Electric double layer at the rutile (110) surface. 3. Inhomogeneous viscosity and diffusivity measurement by computer simulations. *J. Phys. Chem. C* **2007,** *111* (7), 3071-3079.

73. Předota M., Machesky M. L., Wesolowski D. J., Cummings P. T. Electric double layer at the rutile (110) surface. 4. Effect of temperature and pH on the adsorption and dynamics of ions. *J. Phys. Chem. C* **2013,** *117* (44), 22852-22866.

74. Předota M., Machesky M. L., Wesolowski D. J. Molecular origins of the Zeta potential. *Langmuir* **2016,** *32* (40), 10189-10198.

75. Biriukov D., Kroutil O., Předota M. Modeling of solid–liquid interfaces using scaled charges: Rutile (110) surfaces. *Phys. Chem. Chem. Phys.* **2018,** *20* (37), 23954-23966.

76. Biriukov D., Kroutil O., Kabeláč M., Ridley M. K., Machesky M. L., Předota M. Oxalic acid adsorption on rutile: Molecular dynamics and *ab initio* calculations. *Langmuir* **2019,** *35* (24), 7617-7630.

77. Machesky M. L., Ridley M. K., Biriukov D., Kroutil O., Předota M. Oxalic acid adsorption on rutile: Experiments and surface complexation modeling to 150 °C. *Langmuir* **2019,** *35* (24), 7631-7640.

78. Nada H., Kobayashi M., Kakihana M. Anisotropy in conformation and dynamics of a glycolate ion near the surface of a TiO_2 rutile crystal between its {001} and {110} planes: A molecular dynamics study. *J. Phys. Chem. C* **2016,** *120* (12), 6502-6514.

79. Nada H., Kobayashi M., Kakihana M. Anisotropy in stable conformations of hydroxylate ions between the {001} and {110} planes of TiO_2 rutile crystals for glycolate, lactate, and 2-hydroxybutyrate ions studied by metadynamics method. *ACS Omega* **2019,** *4* (6), 11014-11024.

80. Costa D., Garrain P.-A., Baaden M. Understanding small biomolecule-biomaterial interactions: A review of fundamental theoretical and experimental approaches for biomolecule interactions with inorganic surfaces. *J. Biomed. Mater. Res.* **2013,** *101A* (4), 1210-1222.

81. Schwaminger S., Blank-Shim S. A., Borkowska-Panek M., Anand P., Fraga-García P., Fink K., Wenzel W., Berensmeier S. Experimental characterization and simulation of amino acid and peptide interactions with inorganic materials. *Engineer. Life Sci.* **2018,** *18* (2), 84-100.

82. Kyrychenko A. NANOGOLD decorated by pHLIP peptide: Comparative force field study. *Phys. Chem. Chem. Phys.* **2015,** *17* (19), 12648-12660.

83. Kyrychenko A., Blazhynska M. M., Kalugin O. N. Protonation-dependent adsorption of polyarginine onto silver nanoparticles. *J. Appl. Phys.* **2020,** *127* (7), art. no. 075502.

84. Brandt E. G., Lyubartsev A. P. Systematic optimization of a force field for classical simulations of TiO_2–water interfaces. *J. Phys. Chem. C* **2015,** *119* (32), 18110-18125.

85. Brandt E. G., Lyubartsev A. P. Molecular dynamics simulations of adsorption of amino acid side chain analogues and a titanium binding peptide on the TiO_2 (100) surface. *J. Phys. Chem. C* **2015,** *119* (32), 18126-18139.

86. Monti S., Walsh T. R. Molecular dynamics simulations of the adsorption and dynamical behavior of single DNA components on TiO_2. *J. Phys. Chem. C* **2011,** *115* (49), 24238-24246.

87. Neria E., Fischer S., Karplus M. Simulation of activation free energies in molecular systems. *J. Chem. Phys.* **1996,** *105* (5), 1902-1921.

88. Sultan A. M., Hughes Z. E., Walsh T. R. Binding affinities of amino acid analogues at the charged aqueous titania interface: Implications for titania-binding peptides. *Langmuir* **2014,** *30* (44), 13321-13329.

89. Shchelokov A., Palko N., Potemkin V., Grishina M., Morozov R., Korina E., Uchaev D., Krivtsov I., Bol'shakov O. Adsorption of native amino acids on nanocrystalline TiO_2: Physical chemistry, QSPR, and theoretical modeling. *Langmuir* **2019,** *35* (2), 538-550.

90. Monti S., Carravetta V., Zhang W., Yang J. Effects due to interadsorbate interactions on the dipeptide/TiO_2 surface binding mechanism investigated by molecular dynamics simulations. *J. Phys. Chem. C* **2007,** *111* (21), 7765-7771.

91. Tirrell M., Kokkoli E., Biesalski M. The role of surface science in bioengineered materials. *Surf. Sci.* **2002,** *500* (1), 61-83.

92. Wu C., Chen M., Guo C., Zhao X., Yuan C. Peptide−TiO_2 interaction in aqueous solution: Conformational dynamics of RGD using different water models. *J. Phys. Chem. B* **2010,** *114* (13), 4692-4701.

93.   Song D.-P., Chen M.-J., Liang Y.-C., Bai Q.-S., Chen J.-X., Zheng X.-F. Adsorption of tripeptide RGD on rutile TiO$_2$ nanotopography surface in aqueous solution. *Acta Biomater.* **2010,** *6* (2), 684-694.

94.   Wu C., Skelton A. A., Chen M., Vlček L., Cummings P. T. Modeling the interaction between integrin-binding peptide (RGD) and rutile surface: The effect of Na$^+$ on peptide adsorption. *J. Phys. Chem. C* **2011,** *115* (45), 22375-22386.

95.   Wu C., Skelton A. A., Chen M., Vlček L., Cummings P. T. Modeling the interaction between integrin-binding peptide (RGD) and rutile surface: The effect of cation mediation on Asp adsorption. *Langmuir* **2012,** *28* (5), 2799-2811.

96.   Wagstaffe M., Hussain H., Taylor M., Murphy M., Silikas N., Thomas A. G. Interaction of a tripeptide with titania surfaces: RGD adsorption on rutile TiO$_2$(110) and model dental implant surfaces. *Mater. Sci. Eng. C* **2019,** *105, art. no.* 110030.

97.   Wu C., Chen M., Skelton A. A., Cummings P. T., Zheng T. Adsorption of arginine–glycine–aspartate tripeptide onto negatively charged rutile (110) mediated by cations: The effect of surface hydroxylation. *ACS Appl. Mater. Interfaces* **2013,** *5* (7), 2567-2579.

98.   Zhang H.-p., Lu X., Leng Y., Watari F., Weng J., Feng B., Qu S. Effects of aqueous environment and surface defects on Arg-Gly-Asp peptide adsorption on titanium oxide surfaces investigated by molecular dynamics simulation. *J. Biomed. Mater. Res., Part A* **2011,** *96A* (2), 466-476.

99.   Liang Y.-C., Song D.-P., Chen M.-J., Bai Q.-S. Adsorption mechanism of Arg-Gly-Asp on rutile TiO$_2$ (110) surface in aqueous solution. *J. Vac. Sci. Technol. B* **2009,** *27* (3), 1548-1554.

100.   Sultan A. M., Westcott Z. C., Hughes Z. E., Palafox-Hernandez J. P., Giesa T., Puddu V., Buehler M. J., Perry C. C., Walsh T. R. Aqueous peptide–TiO$_2$ interfaces: Isoenergetic binding via either entropically or enthalpically driven mechanisms. *ACS Appl. Mater. Interfaces* **2016,** *8* (28), 18620-18630.

101.   Walsh T. R. Pathways to structure–property relationships of peptide–materials interfaces: Challenges in predicting molecular structures. *Acc. Chem. Res.* **2017,** *50* (7), 1617-1624.

102.   Mao C. M., Sampath J., Sprenger K. G., Drobny G., Pfaendtner J. Molecular driving forces in peptide adsorption to metal oxide surfaces. *Langmuir* **2019,** *35* (17), 5911-5920.

103.   Kang Y., Li X., Tu Y., Wang Q., Ågren H. On the mechanism of protein adsorption onto hydroxylated and nonhydroxylated TiO$_2$ surfaces. *J. Phys. Chem. C* **2010,** *114* (34), 14496-14502.

104.   Puddu V., Slocik J. M., Naik R. R., Perry C. C. Titania binding peptides as templates in the biomimetic synthesis of stable titania nanosols: Insight into the role of buffers in peptide-mediated mineralization. *Langmuir* **2013,** *29* (30), 9464-9472.

105.   Sultan A. M., Hughes Z. E., Walsh T. R. Effect of calcium ions on peptide adsorption at the aqueous rutile titania (110) interface. *Biointerphases* **2018,** *13* (6), art. no. 06D403.

106.   Polimeni M., Petridis L., Smith J. C., Arcangeli C. Dynamics at a peptide–TiO$_2$ anatase (101) interface. *J. Phys. Chem. B* **2017,** *121* (38), 8869-8877.

107.   Hogan B. L. M. Bone morphogenetic proteins in development. *Curr. Opin. Gen. Develop.* **1996,** *6* (4), 432-438.

108.   Yang C., Peng C., Zhao D., Liao C., Zhou J., Lu X. Molecular simulations of myoglobin adsorbed on rutile (110) and (001) surfaces. *Fluid Phase Equilibria* **2014,** *362,* 349-354.

109.   Keefe A. D., Pai S., Ellington A. Aptamers as therapeutics. *Nat. Rev. Drug Discovery* **2010,** *9* (7), 537-550.

110.   Habibzadeh Mashatooki M., Rastkar Ebrahimzadeh A., Jahanbin Sardroodi J., Abbasi A. Investigation of TiO$_2$ anatase (101), (100) and (110) facets as immobilizer for a potential anticancer rna aptamer: A classical molecular dynamics simulation. *Mol. Simul.* **2019,** *45* (11), 849-858.

111.   Cölfen H. A crystal-clear view. *Nat. Mater.* **2010,** *9* (12), 960-961.

112.   Nudelman F., Pieterse K., George A., Bomans P. H. H., Friedrich H., Brylka L. J., Hilbers P. A. J., de With G., Sommerdijk N. A. J. M. The role of collagen in bone apatite formation in the presence of hydroxyapatite nucleation inhibitors. *Nat. Mater.* **2010,** *9* (12), 1004-1009.

113.   Zheng T., Wu C., Chen M. Early adsorption of collagen on the reduced rutile (110) surface mediated by water: A molecular dynamics study. *Surf. Sci.* **2013,** *616,* 51-59.

114. Chen M., Zheng T., Wu C., Xing C. Molecular dynamics simulations of collagen adsorption onto grooved rutile surface: The effects of groove width. *Colloids Surf. B* **2014,** *121,* 150-157.

115. Alamdari S., Pfaendtner J. Impact of glutamate carboxylation in the adsorption of the α-1 domain of osteocalcin to hydroxyapatite and titania. *Mol. Syst. Des. Eng.* **2020,** *5* (3), 620-631.

116. Pierschbacher M. D., Ruoslahti E. Cell attachment activity of fibronectin can be duplicated by small synthetic fragments of the molecule. *Nature* **1984,** *309* (5963), 30-33.

117. Guo C., Wu C., Chen M., Zheng T., Chen N., Cummings P. T. Molecular modeling of fibronectin adsorption on topographically nanostructured rutile (110) surfaces. *Appl. Surf. Sci.* **2016,** *384,* 36-44.

118. Gamucci O., Bertero A., Gagliardi M., Bardi G. Biomedical nanoparticles: Overview of their surface immune-compatibility. *Coatings* **2014,** *4* (1), 139-159.

119. Kyrychenko A., Korsun O. M., Gubin I. I., Kovalenko S. M., Kalugin O. N. Atomistic simulations of coating of silver nanoparticles with poly(vinylpyrrolidone) oligomers: Effect of oligomer chain length. *J. Phys. Chem. C* **2015,** *119* (14), 7888-7899.

120. Kyrychenko A., Pasko D. A., Kalugin O. N. Poly(vinyl alcohol) as a water protecting agent for silver nanoparticles: The role of polymer size and structure. *Phys. Chem. Chem. Phys.* **2017,** *19* (13), 8742-8756.

121. Blazhynska M. M., Kyrychenko A., Kalugin O. N. Molecular dynamics simulation of the size-dependent morphological stability of cubic shape silver nanoparticles. *Mol. Simul.* **2018,** *44* (12), 981-991.

122. Kyrychenko A., Blazhynska M. M., Slavgorodska M. V., Kalugin O. N. Stimuli-responsive adsorption of poly(acrylic acid) onto silver nanoparticles: Role of polymer chain length and degree of ionization. *J. Mol. Liq.* **2019,** *276* 243-254.

123. Borodin O., Smith G. D., Bandyopadhyaya R., Byutner O. Molecular dynamics study of the influence of solid interfaces on poly(ethylene oxide) structure and dynamics. *Macromolecules* **2003,** *36* (20), 7873-7883.

124. Melis C., Mattoni A., Colombo L. Atomistic investigation of poly(3-hexylthiophene) adhesion on nanostructured titania. *J. Phys. Chem. C* **2010,** *114* (8), 3401-3406.

125. Jokerst J. V., Lobovkina T., Zare R. N., Gambhir S. S. Nanoparticle pegylation for imaging and therapy. *Nanomedicine* **2011,** *6* (4), 715-728.

126. Mano S. S., Kanehira K., Sonezaki S., Taniguchi A. Effect of polyethylene glycol modification of TiO$_2$ nanoparticles on cytotoxicity and gene expressions in human cell lines. *Int. J. Mol. Sci.* **2012,** *13* (3), 3703-3717.

127. Sun J., Petersen E. J., Watson S. S., Sims C. M., Kassman A., Frukhtbeyn S., Skrtic D., Ok M. T., Jacobs D. S., Reipa V., Ye Q., Nelson B. C. Biophysical characterization of functionalized titania nanoparticles and their application in dental adhesives. *Acta Biomaterialia* **2017,** *53,* 585-597.

128. Lee Y.-G., Park S., Cho W., Son T., Sudhagar P., Jung J. H., Wooh S., Char K., Kang Y. S. Effective passivation of nanostructured TiO$_2$ interfaces with PEG-based oligomeric coadsorbents to improve the performance of dye-sensitized solar cells. *J. Phys. Chem. C* **2012,** *116* (11), 6770-6777.

129. Jung M.-H., Ko K. C., Lee J. Y. Single crystalline-like TiO$_2$ nanotube fabrication with dominant (001) facets using poly(vinylpyrrolidone) for high efficiency solar cells. *J. Phys. Chem. C* **2014,** *118* (31), 17306-17317.

130. Selli D., Valentin C. D. *Ab initio* investigation of polyethylene glycol coating of TiO$_2$ surfaces. *J. Phys. Chem. C* **2016,** *120* (51), 29190-29201.

131. Selli D., Tawfilas M., Mauri M., Simonutti R., Di Valentin C. Optimizing pegylation of TiO$_2$ nanocrystals through a combined experimental and computational study. *Chem. Mater.* **2019,** *31* (18), 7531-7546.

132. Luan B., Huynh T., Zhou R. Simplified TiO$_2$ force fields for studies of its interaction with biomolecules. *J. Chem. Phys.* **2015,** *142* (23), art. no. 234102.

133. Gindri I. M., Frizzo C. P., Bender C. R., Tier A. Z., Martins M. A. P., Villetti M. A., Machado G., Rodriguez L. C., Rodrigues D. C. Preparation of TiO$_2$ nanoparticles coated with ionic liquids: A supramolecular approach. *ACS Appl. Mater. Interfaces* **2014,** *6* (14), 11536-11543.

134. Schiffmann F., Hutter J., VandeVondele J. Atomistic simulations of a solid/liquid interface: A combined force field and first principles approach to the structure and dynamics of acetonitrile near an anatase surface. *J. Phys.: Cond. Mat.* **2008,** *20* (6), art. no. 064206.

135. Singh R., Rajput N. N., He X., Monk J., Hung F. R. Molecular dynamics simulations of the ionic liquid [EMIM$^+$][TFMSI$^-$] confined inside rutile (110) slit nanopores. *Phys. Chem. Chem. Phys.* **2013,** *15* (38), 16090-16103.

136. Yan T., Wang S., Zhou Y., Cao Z., Li G. Adsorption of CO_2 on the rutile (110) surface in ionic liquid. A molecular dynamics simulation. *J. Phys. Chem. C* **2009,** *113* (45), 19389-19392.

137. Dai Z., Shi L., Lu L., Sun Y., Lu X. Unique structures and vibrational spectra of protic ionic liquids confined in TiO_2 slits: The role of interfacial hydrogen bonds. *Langmuir* **2018,** *34* (44), 13449-13458.

138. Weber H., Salanne M., Kirchner B. Toward an accurate modeling of ionic liquid–TiO_2 interfaces. *J. Phys. Chem. C* **2015,** *119* (45), 25260-25267.

139. Weber H., Bredow T., Kirchner B. Adsorption behavior of the 1,3-dimethylimidazolium thiocyanate and tetracyanoborate ionic liquids at anatase (101) surface. *J. Phys. Chem. C* **2015,** *119* (27), 15137-15149.

140. Kelkar M. S., Maginn E. J. Effect of temperature and water content on the shear viscosity of the ionic liquid 1-ethyl-3-methylimidazolium bis(trifluoromethanesulfonyl)imide as studied by atomistic simulations. *J. Phys. Chem. B* **2007,** *111* (18), 4867-4876.

141. Sambasivarao S. V., Acevedo O. Development of OPLS-AA force field parameters for 68 unique ionic liquids. *J. Chem. Theory Comput.* **2009,** *5* (4), 1038-1050.

142. Malali S., Foroutan M. Study of wetting behavior of BMIM$^+$/PF$_6^-$ ionic liquid on TiO_2 (110) surface by molecular dynamics simulation. *J. Phys. Chem. C* **2017,** *121* (21), 11226-11233.

143. Mohammadpour F., Heydari Dokoohaki M., Zolghadr A. R., Ghatee M. H., Moradi M. Confinement of aqueous mixtures of ionic liquids between amorphous TiO_2 slit nanopores: Electrostatic field induction. *Phys. Chem. Chem. Phys.* **2018,** *20* (46), 29493-29502.

144. Kislenko S. A., Amirov R. H., Samoylov I. S. Effect of cations on the TiO_2/acetonitrile interface structure: A molecular dynamics study. *J. Phys. Chem. C* **2013,** *117* (20), 10589-10596.

145. Nikitin A. M., Lyubartsev A. P. New six-site acetonitrile model for simulations of liquid acetonitrile and its aqueous mixtures. *J. Comput. Chem.* **2007,** *28* (12), 2020-2026.

146. Liu Z., Huang S., Wang W. A refined force field for molecular simulation of imidazolium-based ionic liquids. *J. Phys. Chem. B* **2004,** *108* (34), 12978-12989.

147. Zhang Z., Fenter P., Cheng L., Sturchio N. C., Bedzyk M. J., Předota M., Bandura A., Kubicki J. D., Lvov S. N., Cummings P. T., Chialvo A. A., Ridley M. K., Bénézeth P., Anovitz L., Palmer D. A., Machesky M. L., Wesolowski D. J. Ion adsorption at the rutile–water interface: Linking molecular and macroscopic properties. *Langmuir* **2004,** *20* (12), 4954-4969.

148. Yildirim H., Greeley J. P., Sankaranarayanan S. K. R. S. Localized order–disorder transitions induced by Li segregation in amorphous TiO_2 nanoparticles. *ACS Appl. Mater. Interfaces* **2014,** *6* (21), 18962-18970.

149. Mahjouri-Samani M., Tian M., Puretzky A. A., Chi M., Wang K., Duscher G., Rouleau C. M., Eres G., Yoon M., Lasseter J., Xiao K., Geohegan D. B. Nonequilibrium synthesis of TiO_2 nanoparticle "building blocks" for crystal growth by sequential attachment in pulsed laser deposition. *Nano Lett.* **2017,** *17* (8), 4624-4633.

150. Hagfeldt A., Boschloo G., Sun L., Kloo L., Pettersson H. Dye-sensitized solar cells. *Chem. Rev.* **2010,** *110* (11), 6595-6663.

151. Ooyama Y., Harima Y. Molecular designs and syntheses of organic dyes for dye-sensitized solar cells. *Eur. J. Org. Chem.* **2009,** *2009* (18), 2903-2934.

152. Beljonne D., Cornil J. *Multiscale modelling of organic and hybrid photovoltaics*. Springer Berlin Heidelberg: Berlin, Heidelberg, 2014; Vol. 352, 394 p.

153. Würfel P. *Physics of solar cells. From principles to new concepts*. Wiley-VCH Verlag: London, 2005; 186 p.

154. Luque A., Hegedus S. *Handbook of photovoltaic science and engineering*. John Wiley & Sons, Ltd: London, 2003; 1138 p.

155. Sharma K., Sharma V., Sharma S. S. Dye-sensitized solar cells: Fundamentals and current status. *Nanoscale Res. Lett.* **2018,** *13* (1), art. no. 381.

156. Diebold U. The surface science of titanium dioxide. *Surf. Sci. Rep.* **2003,** *48* (5), 53-229.

157. Gałyńska M., Persson P. Quantum chemical calculations of the structural influence on electronic properties in TiO$_2$ nanocrystals. *Mol. Phys.* **2017,** *115* (17-18), 2209-2217.

158. Labat F., Baranek P., Domain C., Minot C., Adamo C. Density functional theory analysis of the structural and electronic properties of TiO$_2$ rutile and anatase polytypes: Performances of different exchange-correlation functionals. *J. Chem. Phys.* **2007,** *126* (15), 154703.

159. Fazio G., Ferrighi L., Di Valentin C. Spherical versus faceted anatase TiO$_2$ nanoparticles: A model study of structural and electronic properties. *J. Phys. Chem. C* **2015,** *119* (35), 20735-20746.

160. Morita K., Yasuoka K. Density functional theory study of atomic and electronic properties of defects in reduced anatase TiO$_2$ nanocrystals. *AIP Advances* **2018,** *8* (3), art. no. 035119.

161. Selli D., Fazio G., Seifert G., Di Valentin C. Water multilayers on TiO$_2$ (101) anatase surface: Assessment of a DFTB-based method. *J. Chem. Theory Comput.* **2017,** *13* (8), 3862-3873.

162. Selli D., Fazio G., Di Valentin C. Using density functional theory to model realistic TiO$_2$ nanoparticles, their photoactivation and interaction with water. *Catalysts* **2017,** *7* (12), art. no. 357.

163. Selli D., Fazio G., Di Valentin C. Modelling realistic TiO$_2$ nanospheres: A benchmark study of SCC-DFTB against hybrid DFT. *J. Chem. Phys.* **2017,** *147* (16), 164701.

164. Berardo E., Hu H.-S., Shevlin S. A., Woodley S. M., Kowalski K., Zwijnenburg M. A. Modeling excited states in TiO$_2$ nanoparticles: On the accuracy of a TD-DFT based description. *J. Chem. Theory Comput.* **2014,** *10* (3), 1189-1199.

165. Labat F., Le Bahers T., Ciofini I., Adamo C. First-principles modeling of dye-sensitized solar cells: Challenges and perspectives. *Acc. Chem. Res.* **2012,** *45* (8), 1268-1277.

166. Le Bahers T., Labat F., Pauporté T., Lainé P. P., Ciofini I. Theoretical procedure for optimizing dye-sensitized solar cells: From electronic structure to photovoltaic efficiency. *J. Am. Chem. Soc.* **2011,** *133* (20), 8005-8013.

167. Duncan W. R., Prezhdo O. V. Theoretical studies of photoinduced electron transfer in dye-sensitized TiO$_2$. *Ann. Rev. Phys. Chem.* **2007,** *58* (1), 143-184.

168. Oprea I. C., Gîrţu A. M. Structure and electronic properties of TiO$_2$ nanoclusters and dye–nanocluster systems appropriate to model hybrid photovoltaic or photocatalytic applications. *Nanomaterials* **2019,** *9* (3), art. no. 357.

169. Oprea I. C., Panait P., Cimpoesu F., Ferbinteanu M., Gîrţu A. M. Density functional theory (DFT) study of coumarin-based dyes adsorbed on TiO$_2$ nanoclusters—applications to dye-sensitized solar cells. *Materials* **2013,** *6* (6), 2372-2392.

170. O'Rourke C., Bowler D. R. DSSC anchoring groups: A surface dependent decision. *J. Phys.: Condens. Matter.* **2014,** *26* (19), art. no. 195302.

171. Mowbray D. J., Migani A. Optical absorption spectra and excitons of dye-substrate interfaces: Catechol on TiO$_2$(110). *J. Chem. Theory Comput.* **2016,** *12* (6), 2843-2852.

172. Feng J., Jiao Y., Ma W., Nazeeruddin M. K., Grätzel M., Meng S. First principles design of dye molecules with ullazine donor for dye sensitized solar cells. *J. Phys. Chem. C* **2013,** *117* (8), 3772-3778.

173. De Angelis F., Fantacci S., Selloni A., Nazeeruddin M. K., Grätzel M. Time-dependent density functional theory investigations on the excited states of Ru(II)-dye-sensitized TiO$_2$ nanoparticles: The role of sensitizer protonation. *J. Am. Chem. Soc.* **2007,** *129* (46), 14156-14157.

174. Labat F., Adamo C. Bi-isonicotinic acid on anatase (101): Insights from theory. *J. Phys. Chem. C* **2007,** *111* (41), 15034-15042.

175. Labat F., Ciofini I., Hratchian H. P., Frisch M. J., Raghavachari K., Adamo C. Insights into working principles of ruthenium polypyridyl dye-sensitized solar cells from first principles modeling. *J. Phys. Chem. C* **2011,** *115* (10), 4297-4306.

176. Labat F., Ciofini I., Hratchian H. P., Frisch M., Raghavachari K., Adamo C. First principles modeling of eosin-loaded ZnO films: A step toward the understanding of dye-sensitized solar cell performances. *J. Am. Chem. Soc.* **2009,** *131* (40), 14290-14298.

177. Jungsuttiwong S., Tarsang R., Sudyoadsuk T., Promarak V., Khongpracha P., Namuangruk S. Theoretical study on novel double donor-based dyes used in high efficient dye-sensitized solar

cells: The application of TDDFT study to the electron injection process. *Org. Electron.* **2013,** *14* (3), 711-722.

178. Zheng J., Zhang K., Fang Y., Zuo Y., Duan Y., Zhuo Z., Chen X., Yang W., Lin Y., Wong M. S., Pan F. How to optimize the interface between photosensitizers and TiO$_2$ nanocrystals with molecular engineering to enhance performances of dye-sensitized solar cells? *ACS Appl. Mater. Interfaces* **2015,** *7* (45), 25341-25351.

179. Hara K., Sato T., Katoh R., Furube A., Ohga Y., Shinpo A., Suga S., Sayama K., Sugihara H., Arakawa H. Molecular design of coumarin dyes for efficient dye-sensitized solar cells. *J. Phys. Chem. B* **2003,** *107* (2), 597-606.

180. Liu H., Li B., Xue B., Liu E. Theoretical design of high-performance boron dipyrromethenes dyes by introducing heterocyclics to tune photoelectric properties. *J. Phys. Chem. C* **2019,** *123* (43), 26047-26056.

181. Agrawal S., Leijtens T., Ronca E., Pastore M., Snaith H., De Angelis F. Modeling the effect of ionic additives on the optical and electronic properties of a dye-sensitized TiO$_2$ heterointerface: Absorption, charge injection and aggregation. *J. Mater. Chem. A* **2013,** *1* (46), 14675-14685.

182. Le Bahers T., Pauporté T., Scalmani G., Adamo C., Ciofini I. A TD-DFT investigation of ground and excited state properties in indoline dyes used for dye-sensitized solar cells. *Phys. Chem. Chem. Phys.* **2009,** *11* (47), 11276-11284.

183. Luppi E., Urdaneta I., Calatayud M. Photoactivity of molecule–TiO$_2$ clusters with time-dependent density-functional theory. *J. Phys. Chem. A* **2016,** *120* (27), 5115-5124.

184. Yang Z., Liu C., Li K., Cole J. M., Shao C., Cao D. Rational design of dithienopicenocarbazole-based dyes and a prediction of their energy-conversion efficiency characteristics for dye-sensitized solar cells. *ACS Appl. Mater. Interfaces* **2018,** *1* (4), 1435-1444.

185. Estrella L. L., Balanay M. P., Kim D. H. The effect of donor group rigidification on the electronic and optical properties of arylamine-based metal-free dyes for dye-sensitized solar cells: A computational study. *J. Phys. Chem. A* **2016,** *120* (29), 5917-5927.

186. Wen Y., Yang H., Zheng D., Sun K., Wang L., Zhang J. First-principles and molecular dynamics on A–D(π)–A type sensitizers for dye-sensitized solar cells: Effects of various anchoring groups on electronic coupling and dye aggregation. *J. Phys. Chem. C* **2017,** *121* (26), 14019-14026.

187. Gao Y., Lockart M., Kispert L. D., Bowman M. K. Photoinduced charge separation in retinoic acid on TiO$_2$: Comparison of three anchoring modes. *J. Phys. Chem. C* **2019,** *123* (40), 24634-24642.

188. Mosconi E., Selloni A., De Angelis F. Solvent effects on the adsorption geometry and electronic structure of dye-sensitized tio$_2$: A first-principles investigation. *J. Phys. Chem. C* **2012,** *116* (9), 5932-5940.

189. Seo K. D., Choi I. T., Park Y. G., Kang S., Lee J. Y., Kim H. K. Novel D–A–π–A coumarin dyes containing low band-gap chromophores for dye-sensitised solar cells. *Dyes and Pigments* **2012,** *94* (3), 469-474.

190. Hara K., Sayama K., Ohga Y., Shinpo A., Suga S., Arakawa H. A coumarin-derivative dye sensitized nanocrystalline TiO$_2$ solar cell having a high solar-energy conversion efficiency up to 5.6%. *Chem. Commun.* **2001,** (6), 569-570.

191. Hara K., Miyamoto K., Abe Y., Yanagida M. Electron transport in coumarin-dye-sensitized nanocrystalline TiO$_2$ electrodes. *J. Phys. Chem. B* **2005,** *109* (50), 23776-23778.

192. Wang Z. S., Cui Y., Hara K., Dan-oh Y., Kasada C., Shinpo A. A high-light-harvesting-efficiency coumarin dye for stable dye-sensitized solar cells. *Adv. Mater.* **2007,** *19* (8), 1138-1141.

193. Wang Z.-S., Cui Y., Dan-oh Y., Kasada C., Shinpo A., Hara K. Thiophene-functionalized coumarin dye for efficient dye-sensitized solar cells: Electron lifetime improved by coadsorption of deoxycholic acid. *J. Phys. Chem. C* **2007,** *111* (19), 7224-7230.

194. Zhang X., Zhang J.-J., Xia Y.-Y. Molecular design of coumarin dyes with high efficiency in dye-sensitized solar cells. *J. Photochem. Photobiol. A* **2008,** *194* (2), 167-172.

195. Roy J. K., Kar S., Leszczynski J. Electronic structure and optical properties of designed photo-efficient indoline-based dye-sensitizers with D–A−π–A framework. *J. Phys. Chem. C* **2019,** *123* (6), 3309-3320.

196. Sánchez-de-Armas R., Oviedo J., San Miguel M. Á., Sanz J. F. Direct vs indirect mechanisms for electron injection in dye-sensitized solar cells. *J. Phys. Chem. C* **2011,** *115* (22), 11293-11301.

197. Pastore M., Fantacci S., De Angelis F. Modeling excited states and alignment of energy levels in dye-sensitized solar cells: Successes, failures, and challenges. *J. Phys. Chem. C* **2013,** *117* (8), 3685-3700.

198. De Angelis F., Fantacci S., Mosconi E., Nazeeruddin M. K., Grätzel M. Absorption spectra and excited state energy levels of the N719 dye on TiO_2 in dye-sensitized solar cell models. *J. Phys. Chem. C* **2011,** *115* (17), 8825-8831.

199. De Angelis F., Fantacci S., Selloni A., Nazeeruddin M. K., Grätzel M. First-principles modeling of the adsorption geometry and electronic structure of Ru(II) dyes on extended TiO_2 substrates for dye-sensitized solar cell applications. *J. Phys. Chem. C* **2010,** *114* (13), 6054-6061.

200. Oviedo M. B., Zarate X., Negre C. F. A., Schott E., Arratia-Pérez R., Sánchez C. G. Quantum dynamical simulations as a tool for predicting photoinjection mechanisms in dye-sensitized TiO_2 solar cells. *J. Phys. Chem. Lett.* **2012,** *3* (18), 2548-2555.

201. Negre C. F. A., Fuertes V. C., Oviedo M. B., Oliva F. Y., Sánchez C. G. Quantum dynamics of light-induced charge injection in a model dye–nanoparticle complex. *J. Phys. Chem. C* **2012,** *116* (28), 14748-14753.

202. Negre C. F. A., Young K. J., Oviedo M. B., Allen L. J., Sánchez C. G., Jarzembska K. N., Benedict J. B., Crabtree R. H., Coppens P., Brudvig G. W., Batista V. S. Photoelectrochemical hole injection revealed in polyoxotitanate nanocrystals functionalized with organic adsorbates. *J. Am. Chem. Soc.* **2014,** *136* (46), 16420-16429.

203. Marquez D. M., Sánchez C. G. Quantum efficiency of the photo-induced electronic transfer in dye–TiO_2 complexes. *Phys. Chem. Chem. Phys.* **2018,** *20* (41), 26280-26287.

204. Ronchi C., Selli D., Pipornpong W., Di Valentin C. Proton transfers at a dopamine-functionalized TiO_2 interface. *J. Phys. Chem. C* **2019,** *123* (13), 7682-7695.

205. Zhang L., Cole J. M. Adsorption properties of *p*-methyl red monomeric-to-pentameric dye aggregates on anatase (101) titania surfaces: First-principles calculations of dye/TiO_2 photoanode interfaces for dye-sensitized solar cells. *ACS Appl. Mater. Interfaces* **2014,** *6* (18), 15760-15766.

206. Monti S., Pastore M., Li C., De Angelis F., Carravetta V. Theoretical investigation of adsorption, dynamics, self-aggregation, and spectroscopic properties of the D102 indoline dye on an anatase (101) substrate. *J. Phys. Chem. C* **2016,** *120* (5), 2787-2796.

207. Marx D., Hutter J. *Ab initio molecular dynamics: Basic theory and advanced methods.* Cambridge University Press: Cambridge, 2009; 567 p.

208. Car R., Parrinello M. Unified approach for molecular dynamics and density-functional theory. *Phys. Rev. Lett.* **1985,** *55* (22), 2471-2474.

209. Tuckerman M. E., Parrinello M. Integrating the Car–Parrinello equations. I. Basic integration techniques. *J. Chem. Phys.* **1994,** *101* (2), 1302-1315.

210. Doltsinis N. L., Marx D. First pprinciples molecular dynamics involving excited states and nonadiabatic transitions. *J. Theory Comput. Chem.* **2002,** *01* (02), 319-349.

211. Stier W., Prezhdo O. V. Thermal effects in the ultrafast photoinduced electron transfer from a molecular donor anchored to a semiconductor acceptor. *Isr. J. Chem.* **2002,** *42* (2-3), 213-224.

212. Stier W., Prezhdo O. V. Nonadiabatic molecular dynamics simulation of light-induced electron transfer from an anchored molecular electron donor to a semiconductor acceptor. *J. Phys. Chem. B* **2002,** *106* (33), 8047-8054.

213. Stier W., Prezhdo O. V. Non-adiabatic molecular dynamics simulation of ultrafast solar cell electron transfer. *J. Mol. Struct.: Theochem.* **2003,** *630* (1), 33-43.

214. Alvarez-Ramirez F., Ruiz-Morales Y. *Ab initio* molecular dynamics calculations of the phase transformation mechanism for the formation of TiO_2 titanate-type nanosheets from anatase. *Chem. Mater.* **2007,** *19* (12), 2947-2959.

215. Fischer S. A., Duncan W. R., Prezhdo O. V. *Ab initio* nonadiabatic molecular dynamics of wet-electrons on the TiO_2 surface. *J. Am. Chem. Soc.* **2009,** *131* (42), 15483-15491.

216. Vogel D. J., Kilin D. S. Electron dynamics of solvated $Ti(OH)_4$. *MRS Proceedings* **2014,** *1647,* art. no. mrsf13-1647-gg08-07.

217. Brandt E. G., Agosta L., Lyubartsev A. P. Reactive wetting properties of TiO$_2$ nanoparticles predicted by *ab initio* molecular dynamics simulations. *Nanoscale* **2016,** *8* (27), 13385-13398.

218. Dubot P., Boisseau N., Cenedese P. Large scale full qm-md investigation of small peptides and insulin adsorption on ideal and defective TiO$_2$ (100) surfaces. Influence of peptide size on interfacial bonds. *Appl. Surf. Sci.* **2018,** *440* 614-626.

219. Fazio G., Selli D., Ferraro L., Seifert G., Di Valentin C. Curved TiO$_2$ nanoparticles in water: Short (chemical) and long (physical) range interfacial effects. *ACS Appl. Mater. Interfaces* **2018,** *10* (35), 29943-29953.

220. Byrne A., English N. J. A systematic study via *ab-initio* MD of the effect solvation by room temperature ionic liquid has on the structure of a chromophore-titania interface. *Comput. Mater. Sci.* **2018,** *141* 193-206.

221. Tateyama Y., Sumita M., Ootani Y., Aikawa K., Jono R., Han L., Sodeyama K. Acetonitrile solution effect on Ru N749 dye adsorption and excitation at TiO$_2$ anatase interface. *J. Phys. Chem. C* **2014,** *118* (30), 16863-16871.

222. Monti A., de Ruiter J. M., de Groot H. J. M., Buda F. A dynamic view of proton-coupled electron transfer in photocatalytic water splitting. *J. Phys. Chem. C* **2016,** *120* (40), 23074-23082.

223. Mathew S., Yella A., Gao P., Humphry-Baker R., Curchod B. F. E., Ashari-Astani N., Tavernelli I., Rothlisberger U., Nazeeruddin M. K., Grätzel M. Dye-sensitized solar cells with 13% efficiency achieved through the molecular engineering of porphyrin sensitizers. *Nat. Chem.* **2014,** *6* (3), 242-247.

224. Ambrosio F., Martsinovich N., Troisi A. What is the best anchoring group for a dye in a dye-sensitized solar cell? *J. Phys. Chem. Lett.* **2012,** *3* (11), 1531-1535.

225. Zhang L., Cole J. M. Anchoring groups for dye-sensitized solar cells. *ACS Appl. Mater. Interfaces* **2015,** *7* (6), 3427-3455.

226. Smith J. L. On the simultaneous staining of neutral fat and fatty acid by oxazine dyes. *J. Pathol. Bacteriol.* **1908,** *12* (1), 1-4.

227. Heinz H. Adsorption of biomolecules and polymers on silicates, glasses, and oxides: Mechanisms, predictions, and opportunities by molecular simulation. *Curr. Opin. Chem. Engineer.* **2016,** *11* 34-41.

228. Heinz H., Ramezani-Dakhel H. Simulations of inorganic-bioorganic interfaces to discover new materials: Insights, comparisons to experiment, challenges, and opportunities. *Chem. Soc. Rev.* **2016,** *45* (2), 412-448.

229. Liu J., Wang Z., Zeng J., Heinz H. Molecular structure and assembly of peptide-derived nanomaterials. *Curr. Opin. Green Sustainable Chem.* **2018,** *12* 38-46.

230. De Angelis F. Modeling materials and processes in hybrid/organic photovoltaics: From dye-sensitized to perovskite solar cells. *Acc. Chem. Res.* **2014,** *47* (11), 3349-3360.

231. Casida M. E., Huix-Rotllant M. Progress in time-dependent density-functional theory. *Annu. Rev. Phys. Chem.* **2012,** *63* (1), 287-323.

М.М. Блажинская†, А.В. Кириченко†, Д.С. Степанюк†, А.Н. Корсун†, С.Н. Коваленко†, В.В. Иванов†, Ф.-А. Мьяне‡, А. Идрисси‡, О.Н. Калугин†. Новые достижения в теоретическом исследовании наноматериалов на основе диоксида титана. Обзор.

† Харьковский национальный университет имени В.Н. Каразина, химический факультет, пл. Свободы, 4, Харьков, 61022, Украина
‡ Университет Лилля UMR8516, 59655, Вильнёв-д'Аск, Сендекс, Франция.

Диоксид титана (TiO$_2$) является одним из наиболее широко используемых наноматериалов во многих новых областях материаловедения, включая конверсию солнечной энергии и биомедицинскую имплантацию. Настоящий обзор посвящен рассмотрению и анализу прогресса и последних достижений в области теории и компьютерного моделирования физико-химических свойств небольших кластеров TiO$_2$, наночастиц среднего размера, а также границы раздела жидкость-твердое вещество. Дан исторический обзор и

разработка эмпирических силовых полей для классической молекулярной динамики (МД) различных полиморфов TiO_2, таких как рутил, анатаз и брукит. Исследовано адсорбционное поведение молекул растворителя, ионов, малых органических лигандов и биомакромолекул на поверхности TiO_2 с целью понимания движущих сил и механизмов, которые управляют связыванием и распознаванием между адсорбатом и поверхностями. Обсуждено влияние кристаллических форм, кристаллографических плоскостей, поверхностных дефектов и сред растворителей на процесс адсорбции. Рассмотрены структурные детали и динамика адсорбционных явлений, происходящих на границах раздела жидкость-твердое тело, начиная с ранних эмпирических моделей потенциала до недавнего реактивного ReaxFF МД моделирования, способного улавливать диссоциативную адсорбцию молекул воды. Эффективность различных теоретических методов варьировалась от квантово-механических (QM) расчетов (*ab initio* и теории функционала плотности) до классического силового поля и гибридного моделирования MM/QM. Кроме того, обсужден недавний прогресс в вычислительной химии индуцированных светом электронных процессов, лежащих в основе структуры, динамики и функционирования молекулярных и гибридных материалов, с особым вниманием к применению солнечной энергии в сенсибилизированных красителем солнечных элементах (DSSC), которые в настоящее время находятся в стадии разработки. Кроме того, проанализированы принципы конструирования красителей, роль закрепления фрагмента и агрегации красителя в характеристиках DSSC. Наконец, очерчены перспективы и проблемы дальнейшего прогресса в исследованиях и многообещающие направления в разработке точных вычислительных инструментов для моделирования взаимодействий между неорганическими материалами с неидеальными структурами и природными биомакромолекулами в физиологических условиях.

Ключевые слова: диоксид титана, рутил, анатаз, брукит, сенсибилизация красителем, наночастица, граница раздела жидкость-твердое вещество, молекулярно-динамическое моделирование, *ab initio* молекулярная динамика.

М.М. Блажинська[†], О.В. Кириченко[†], Д.С. Степанюк[†], О.М. Корсун[†], С.М. Коваленко[†], В.В. Іванов[†], Ф.-О. М'яне[‡], А. Ідріссі[‡], О.М. Калугін[†]. Новітні досягнення у теоретичному дослідженні наноматеріалів на основі діоксиду титану. Огляд.

[†] Харківський національний університет імені В.Н. Каразіна, хімічний факультет, майдан Свободи, 4, Харків, 61022, Україна

[‡] Університет Лілля UMR8516, 59655, Вільньов-д'Аск, Сендекс, Франція

Діоксид титану (TiO_2) є одним з найбільш широко використовуваних наноматеріалів в багатьох нових областях матеріалознавства, включаючи конверсію сонячної енергії і біомедичну імплантацію. Огляд присвячено прогресу і останнім досягненням в області теорії і комп'ютерного моделювання фізико-хімічних властивостей невеликих кластерів TiO_2, наночастинок середнього розміру, а також кордону розділу рідина-тверда речовина. Подано історичний огляд і розробка емпіричних силових полів для класичної молекулярної динаміки (МД) різних поліморфів TiO_2, таких як рутил, анатаз і брукіт. Досліджено адсорбційну поведінку молекул розчинника, іонів, малих органічних лігандів і біомакромолекул на поверхні TiO_2 досліджується з метою розуміння рушійних сил і механізмів, які керують зв'язуванням і розпізнаванням між адсорбатом і поверхнями. Обговорено вплив кристалічних форм, кристалографічних площин, поверхневих дефектів і середовищ розчинників на процес адсорбції. Розглянуті структурні деталі і динаміка адсорбційних явищ, що відбуваються на кордонах розділу рідина-тверде тіло, починаючи з ранніх емпіричних моделей потенціалу до недавнього реактивного ReaxFF МД моделювання, здатного вловлювати дисоціативну адсорбцію молекул води. Ефективність різних теоретичних методів варіювалася від квантово-механічних (QM) розрахунків (*ab initio* і теорії функціонала густини) до класичного силового поля і гібридного моделювання MM/QM. Крім того, розглянуто недавній прогрес в обчислювальній хімії індукованих світлом електронних процесів, що лежать в основі структури, динаміки і функціонування молекулярних і гібридних матеріалів з особливою увагою до застосуванні сонячної енергії в сенсибілізованих барвником сонячних елементах (DSSC), які в даний час знаходяться в стадії розробки. Крім того, були проаналізовані принципи конструювання барвників, роль закріплення фрагмента і агрегації барвника в характеристиках DSSC. Нарешті, окреслені перспективи і проблеми подальшого прогресу в дослідженнях і багатообіцяючі напрямки в розробці точних обчислювальних інструментів для моделювання взаємодій між неорганічними матеріалами з недосконалими структурами і природними біомакромолекул в фізіологічних умовах.

Ключові слова: діоксид титану, рутил, анатаз, брукіт, сенсибілізація барвником, наночастинка, межа поділу рідина-тверда речовина, молекулярно-динамічне моделювання, *ab initio* молекулярна динаміка.

NITROXYL SPIN PROBE IN IONIC MICELLES: A MOLECULAR DYNAMICS STUDY

V.S. Farafonov [a], A.V. Lebed [b]

V.N. Karazin Kharkiv National University, School of Chemistry, 4 Svobody sqr., 61022 Kharkiv, Ukraine

a) ✉ *farafonov@karazin.ua*　　　　　　　　 *https://orcid.org/0000-0003-0785-9582*
b) ✉ *alebed@karazin.ua*　　　　　　　　　　 *https://orcid.org/0000-0001-5175-816X*

The compounds containing nitroxyl radical (NO˙) are actively used as spin probes to examine colloid systems, including lipid membranes and micelles. Their electron paramagnetic resonance spectrum provides information about the composition of the medium, in particular, the content of water there. Yet, the proper treatment of the measurement results demands understanding the microscopic characteristics of the molecular probe. In the present paper, we extend our previous studies on the microscopic state of acid-base and solvatochromic probes in surfactant micelles to the field of spin probes. We report the results of molecular dynamics simulation of a common spin probe, methyl-5-doxylstearate, in micelles of anionic (sodium *n*-dodecyl sulfate, SDS) and cationic (*n*-dodecyltrimethylammonium bromide, DTAB) surfactants. The localization of the molecule within the micelles, its shape, composition of the local environment, hydration were quantified and compared with the available relevant experimental data. No significant dissimilarity was found in the characteristics of the probe molecule in both kinds of micelles. However, the characteristics of the O˙ atom carrying the unpaired electron are pronouncedly different, namely, in DTAB micelles it is less hydrated and forms less hydrogen bonds with water. Similar situation was observed for the COO group. The main reason was found to be the interactions with cationic surfactant headgroups, which screen the O˙ atom and COO group from water. These findings allowed revisit the point of view that the surface layer of DTAB micelles as a whole is less hydrated in comparison to that of the SDS ones.

Keywords: methyl-5-doxylstearate, sodium dodecyl sulfate, dodecyltrimethylammonium bromide, localization, conformation, hydration, hydrogen bond.

Introduction

The structure of micelles of ionic surfactants and their surface layers is an area of active research by modern experimental methods. While some information may be obtained directly, estimating many important properties demands using molecular probes. In the latter case, a compound called molecular probe is added to the micellar solution, and the change of its properties (with respect to its pure water solution) is experimentally registered. The properties include fluorescence spectrum (for fluorescence probes), apparent acidity constant (for acid-base probes), UV/vis absorption spectrum (for solvatochromic probes) and electron paramagnetic resonance spectrum (for spin probes). This change may be then related to such micelle properties as microviscosity, electrostatic potential, polarity, hydration, respectively [1–6]. However, to establish this relation, the knowledge of the state of the molecular probe in the micelle is necessary. It is usually obtained by means of nuclear magnetic resonance spectroscopy; yet, the method provides only rather general insight to the probe localization [7,8]. More detailed localization information is inaccessible for it.

Recently, the computational methods have been involved to the research, as well. Among them, the molecular dynamics (MD) simulations method became particularly popular because of its ability to capture both structural and dynamic properties of these objects. It allows direct observation of the microscopic details of the system, which are unachievable for most experimental means. Hence, the MD method was actively applied firstly to individual micelles [9,10], and then to micelles with solubilized molecular probes, including the fluorescent [11], acid-base [12], and solvatochromic [13,14] ones. Yet, for the group of spin probes such studies still are rather scarce [15–17], albeit they are numerous for lipid bilayers [18,19] and proteins [20,21].

In this work, we extend our studies on the microscopic state of solvatochromic and acid-base probes in micellar solutions to the field of spin probes. Their particular feature is the ability to estimate the water fraction (*i.e.* hydration) in the medium. The principle is based on an established linear correlation between i) the measured hyperfine splitting in electron paramagnetic resonance (EPR) spectrum of the probe and ii) the concentration of O–H dipoles in medium [22]. For solutions of surfactants,

which are not hydrogen bond donors, the latter equals to concentration of water. The result of measurement is usually presented as the ratio H between water concentrations in the medium and in pure water.

Among the variety of probes, we choose a rather popular representative methyl-5-doxylstearate (MDS, Fig 1). Its spin label is the nitroxyl radical NO· containing the O atom with unpaired electron. The presence of the long hydrocarbon chain assures incorporation of the probe to the examined lipid bilayer or micelle. Particularly, it was previously employed to assess the water content in the surface layer of sodium *n*-dodecyl sulfate (SDS) and *n*-dodecyltrimethylammonium bromide (DTAB) micelles, Fig. 1: the former ones were found to have larger H and, thus, be hydrated stronger [5,6]. MDS has been already simulated in zwitterionic micelles of *N*-dodecyl-*N,N*-dimethyl-3-ammonio-1-propanesulfonate [17]. In this work we examine the microscopic localization and hydration of MDS molecule in SDS and DTAB micelles by means of MD simulation.
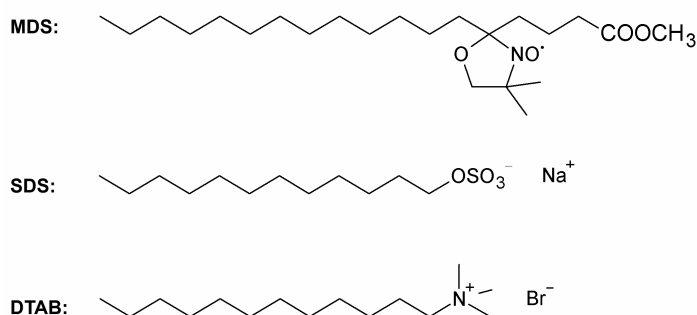
Figure 1. Structure formulas of the spin probe and surfactants considered in this work.

Simulation methodology

The simulations were carried out at standard conditions, maintained by means of Berendsen thermostat and barostat. The 3D periodic boundary conditions were imposed, time step equaled 2 fs. Electrostatic interactions were computed with the PME method, while van der Waals interactions were cut-off at 1 nm. GROMACS 5.0 software was employed.

The initial configurations were micelles of 60 monomers with an MDS molecule placed inside. This number corresponds to the aggregation numbers of these surfactants [23]. Three different initial configurations were prepared for each system. Simulations were run for 40 ns, the first 10 ns of the resulting trajectories were treated as equilibration and not used in calculations. The multistage procedure of preparation of initial configurations is described in detail in our previous papers [13]. Three 11 ns simulations in pure water were also performed, the first 1 ns was omitted in calculations as equilibration.

The potential models for compounds were derived in the framework of the OPLS-AA force field. SDS and DTAB models previously developed by us were taken [10,14]; water was described with the SPC model. The model for MDS was built following the accepted in OPLS-AA protocol. The atom types were assigned manually from the set available in the OPLS-AA. The atoms of ester group and the most of hydrocarbon radical were attributed with the respective built-in charges in the force field. Oppositely, the atomic charges in the doxyl moiety were computed *ab initio* because they are not present in OPLS-AA. At the first stage, the quantum-chemical computation of the electrostatic potential around the doxyl moiety including four adjacent CH_2 groups was performed (the parameters were: Hartree-Fock level of theory, 6-31G(d) basis set, vacuum medium). At the second stage, the potential was fitted with a set of point charges placed on atoms. To facilitate the process, the RED Server was employed: it automatically performs both steps for a specified molecule, providing the final point charges [24]. The produced potential model is shown in Appendix, Fig. A1.

Results and discussion

The first point of the study is understanding the location of the probe molecule. As a quantitative measure we used the distribution function of the distance (DFD) $p(r)$ defined as a time-averaged probability p to observe the chosen distance equal to r during MD. The DFD's were computed between the

micelle center of mass (COM) and indicative atoms of the probe molecule: the O˙ atom and the C atom of carboxyl group (C_{COO}). The DFD's between micelle COM and S or N atoms of the surfactant headgroups were also plotted to outline the location of the micelle surface. The graphs are shown in Fig. 2.

The positioning of the indicative atoms differs rather little: the peaks of C_{COO} and O˙ atoms are shifted by +0.15 nm upon going from DTAB micelles to the SDS ones. In both cases, C_{COO} is ~0.15 nm advanced towards water. To provide visual understanding, the typical configurations of MDS in micelles are shown in Appendix, Fig. A2.
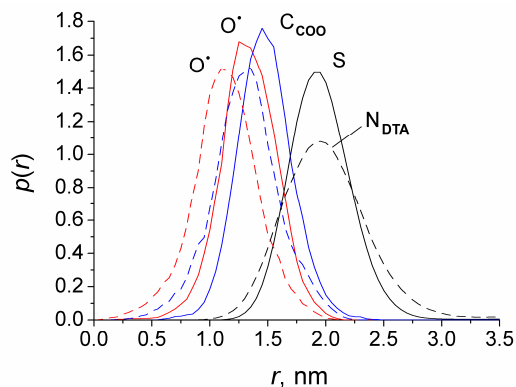
Figure 2. Distribution functions of distances micelle COM – O˙ (red), micelle COM – C in COO group (blue), micelle COM – surfactant S or N (black). Solid curves are for SDS micelles, dashed curves are for the DTAB ones.

The doxyl moiety is attached to a long hydrocarbon chain (17 C atoms). It is known that such chains tend to adopt a bent conformation because the straight conformation is statistically rather improbable. Further, the chain is longer than that in surfactant molecules (12 C atoms). It is interesting now to inspect the average curvature of the MDS molecule. We described it in terms of DFD between the C_{COO} atom and the C atom in the terminal CH_3 group, Fig. 3A. Small values indicate strong bend of the molecule and *vice versa*. According to the used potential model, the maximum value (that corresponds to the *anti* conformation of all C–C bonds) equals 2.0 nm. The calculated distribution functions are shown in Fig. 3B.

The distance mostly lies within 1.4–1.8 nm range, its preferable value is 1.6 nm indicating rather limited bend. No significant difference is present between the two surfactant solutions.

A	**B**
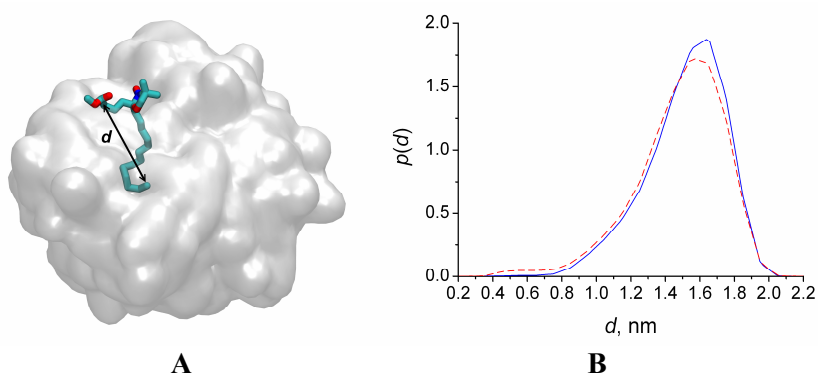
Figure 3. A: Definition of the distance *d* that characterizes the bend of MDS molecule (the gray surface represents the micelle hydrocarbon core); **B:** Distribution functions of *d* in SDS (blue solid curve) and DTAB (red dashed curve) micelles.

The investigated molecule is used to probe the water content in micelles. Therefore, the central point of our study is the inspection of composition of the solution located in the immediate vicinity of the MDS molecule, which is its microenvironment. We chose to inspect not only the microenvironment of the whole molecule, but also that of the COO moiety and the O˙ atom carrying the unpaired electron. The previously developed approach was used: for each time moment, the solution atoms

located within the 0.4 nm vicinity of any atom of the examined moiety were found and distributed into 3 groups depending on their kind (micelle hydrocarbon core, surfactant headgroups, and water). The time-averaged number of atoms in each group characterizes the medium the moiety is situated in. For convenience we converted these numbers to molar fractions. The latter are depicted in Fig. 4A.
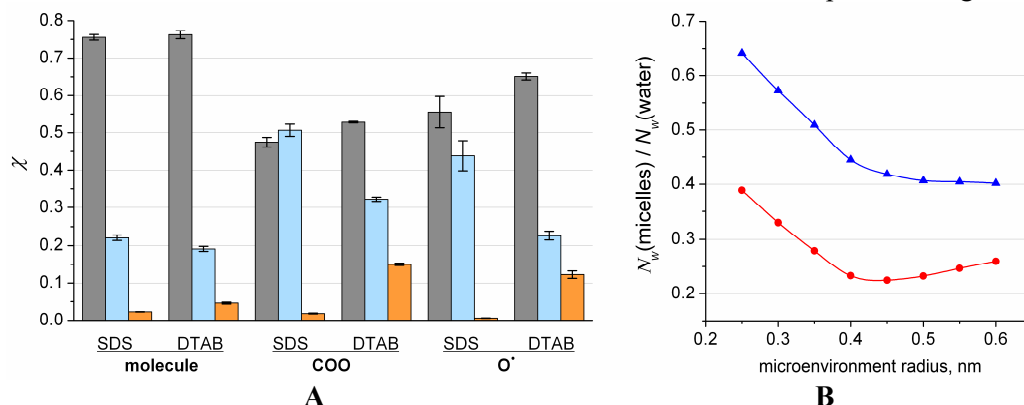
Figure 4. A: Microenvironment composition of the whole molecule and COO, O˙ moieties in micelles. The bars in triples correspond to (left to right): the micelle core atoms (gray), the water atoms (blue), the headgroup atoms (orange). **B:** The amount of water in the microenvironment of the O˙ atom in SDS (blue triangles) and DTAB (red circles) micelles relative to the pure water solution, calculated at different values of microenvironment radius.

The local environment of the whole molecule almost does not change upon going from one surfactant to another, the water content in it reaches ~20%. This is reasonable because the molecule contains only few atoms, which are expected to interact differently with cationic and anionic surfactants: the COO group and the two O atoms in doxyl moiety, all carrying high fractional charge ($|\delta| \sim 0.35–0.5$). For the COO group the difference becomes more pronounced: the water fraction in DTAB micelles is 19% lower than in SDS ones, mostly due to the increased fraction of headgroups (by 13%). The COO group in total is negatively charged, hence, it repels anionic headgroups and attracts the cationic ones. This effect was previously observed by us for acid-base and solvatochromic probes [12–14], where hydroxyl and carboxyl groups in neutral and, even more, anionic protolytic forms were strongly screened by cationic headgroups and, thus, had limited amount of water molecules around. The remaining 6% of the difference correspond to the increased fraction of hydrocarbon, which consequently is attributed to the slightly deeper immersion into micelles (Fig. 2A).

The situation for the O˙ atom is rather similar to that of the COO group. Because it is of a particular interest, we performed a more detailed analysis of its hydration. Firstly, we repeated counting water atoms around O˙ at the values of microenvironment radius other than 0.4 nm (namely, 0.25–0.6 nm). The results, N_w(micelle), were then related to the ones in pure water solution, N_w(water), Fig. 4B. Secondly, we determined the average number of O˙–water hydrogen bonds, n_{hb}. It equals 1.07±0.01 for pure water solution, 0.74±0.03 for the SDS one, and 0.46±0.03 for the DTAB one. This data proves much more aqueous environment of O˙ in the anionic surfactant than in the cationic one. This is caused firstly by the screening with the cationic headgroups (their fraction reaches 12% in DTAB) and secondly by the larger fraction of hydrocarbon around due to somewhat deeper localization in DTAB micelles (Fig. 2A).

Now we can consider the results of experimental measurements of SDS and DTAB solutions made using MDS in the light of the presented information about the microscopic state of this molecular probe. Specifically, in the works of Lebedeva *et al.* [5,6] the EPR spectrum of MDS was found to correspond to the molar concentration of water in the medium (relative to pure water) H equal to 0.68 and 0.44 in SDS and DTAB micelles, respectively. These values were then attributed to the whole surface layer of these micelles.

Matching these results with the data in Fig. 4B and n_{hb} values shows that they agree well with the values n_{hb}(micelle) / n_{hb}(water), which equal 0.69 for SDS and 0.43 for DTAB. Good match is also observed with the ratios N_w(micelle) / N_w(water) values of O˙ at microenvironment radius 0.25 nm: 0.64 for SDS and 0.39 for DTAB. These observations shed light on the microscopic reason of the O˙ EPR signal charge in micellar solutions. The effect of hydrogen bonding was assumed [22], but it was

not quantitatively shown in terms of the number of such bonds made by the probe with water. Further, the fact of almost quantitative agreement proves the adequacy of used model in the context of discussed problem.

On the other hand, attributing the measured H values to the entire surface layer appears to be unjustified. The localization of the molecule is similar in both micelles, its shape is similar, too (Fig. 2, 3). Given these conditions, its microenvironment should be much more hydrated in SDS micelles, if their surface layer actually contains more water. However, no considerable difference is observed (Fig. 4A). This allows suppose the overall similarity of water fractions in the surface layers of SDS and DTAB micelles, with the variations present in the local vicinity of the spin label only.

Conclusions

MD simulations of a spin probe methyl-5-doxylstearate in micelles of ionic surfactants sodium *n*-dodecyl sulfate and *n*-dodecyltrimethylammonuim bromide were performed. The localization of the molecule was examined and the hydration of the molecule and its moieties was calculated by counting water atoms in their microenvironments and counting hydrogen bonds made with water molecules. The molecule was found to be slightly deeper immersed into micelles of DTAB compared to SDS. The curvature and hydration of the molecule is also similar in both micelles. At the same time, the O˙ atom in nitroxyle radical is much better hydrated in SDS micelles than in the DTAB ones. This is caused mostly by its screening from water by cationic headgroups of DTAB and slightly deeper localization in the micelles. Therefore, it is concluded that the experimentally measured hydration values likely correspond not to the complete surface layer, but to the local environment of the spin label only. Importantly, the hydration values of the O˙ atom calculated in such a way quantitatively agree with the experiment. This proves the adequacy and usefulness of the approach and the model used for investigating local environments of molecular probes in micellar solutions.

Acknowledgements

Appendix
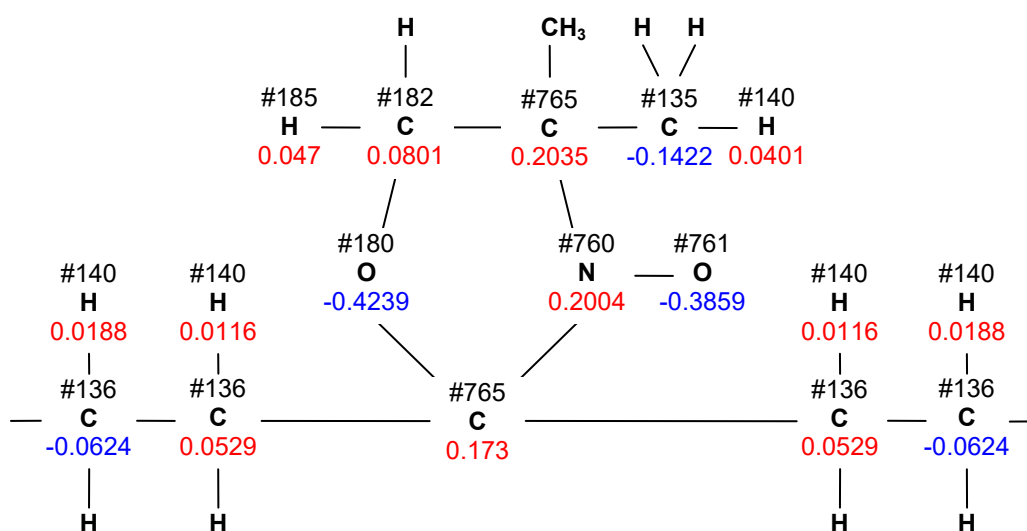
Figure A1. Atomic charges and types used in the potential model of MDS radical. The part with non-standard parameters is shown only.
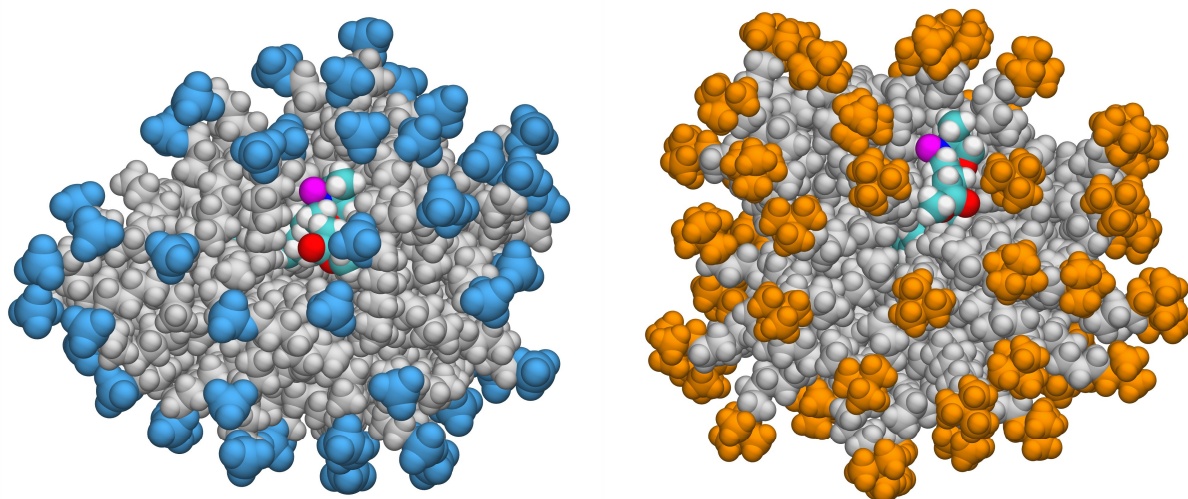
Figure A2. Snapshots from MD trajectories showing typical MDS localization in SDS (left) and DTAB (right) micelles. For micelles, hydrocarbon core is colored gray and the headgroups are colored light blue or orange. The O˙ atom with unpaired electron is highlighted with pink.

References

1. Bahri M. A., Hoebeke M., Grammenos A., Delanaye L., Seret A. Investigation of SDS, DTAB and CTAB Micelle Microviscosities by Electron Spin Resonance. // Colloids Surf. A 2006. Vol.290, No.1–3. P.206–212.

2. Mchedlov-Petrossyan N. O., Vodolazkaya N. A., Yakubovskaya A. G., Grigorovich A. V., Alekseeva V. I., Savvina L. P. A Novel Probe for Determination of Electrical Surface Potential of Surfactant Micelles: N,N'-Di-n-Octadecylrhodamine. // J. Phys. Org. Chem. 2007. Vol.20, No.5. P.332–344.

3. Mchedlov-Petrossyan N. O. Protolytic equilibrium in lyophilic nanosized dispersions: differentiating influence of the pseudophase and salt effects. // Pure Appl. Chem. 2008. Vol.80, No.7. P.1459–1510.

4. Machado V. G., Stock R. I., Reichardt C. Pyridinium *N*-phenolate betaine dyes. // Chem. Rev. 2014. Vol.114, No. 20. P.10429–10475.

5. Lebedeva N., Bales B. L. Location of Spectroscopic Probes in Self-Aggregating Assemblies. I. The Case for 5-Doxylstearic Acid Methyl Ester Serving as a Benchmark Spectroscopic Probe to Study Micelles. // J. Phys. Chem. B 2006. Vol.110, No.20. P.9791–9799.

6. Lebedeva N., Zana R., Bales B. L. A Reinterpretation of the Hydration of Micelles of Dodecyltrimethylammonium Bromide and Chloride in Aqueous Solution. // J. Phys. Chem. B 2006. Vol.110, No.20. P.9800–9801.

7. Plieninger P., Baumgärtel H. A. 1H NMR Investigation Concerning the Insertion of Pyridinium N-Phenoxide Betaines into Micelles. // Liebigs Ann. Chem. 1983. Vol.5. P.860–875.

8. Tada E. B., Novaki L. P., El Seoud O. A. Solvatochromism in Cationic Micellar Solutions: Effects of the Molecular Structures of the Solvatochromic Probe and the Surfactant Headgroup. // Langmuir 2001. Vol.17, No.3. P.652–658.

9. Rakitin A. R., Pack G. R. Molecular Dynamics Simulations of Ionic Interactions with Dodecyl Sulfate Micelles. // J. Phys. Chem. B 2004. Vol.108, No.8. P.2712–2716.

10. Farafonov V. S., Lebed A. V. Developing and validating a set of all-atom potential models for sodium dodecyl sulfate. // J. Chem. Theory Comput. 2017. Vol.13, No.6. P.2742−2750.

11. Gao F., Yan H., Yuan S. Fluorescent Probe Solubilised in Cetyltrimethylammonium Bromide Micelles by Molecular Dynamics Simulation. // Mol. Simul. 2013. Vol.39, No.13. P. 1042–1051.

12. Mchedlov-Petrossyan N. O., Farafonov V. S., Cheipesh T. A., Shekhovtsov S. V., Nerukh D. A., Lebed A. V. In search of an optimal acid-base indicator for examining surfactant micelles: Spectrophotometric studies and molecular dynamics simulations. // Coll. Surf. A 2019. Vol.565. P.97–107.

Spectrophotometric studies and molecular dynamics simulations. // Coll. Surf. A 2019. Vol.565. P.97–107.

13. Farafonov V. S., Lebed A. V., Mchedlov-Petrossyan N. O. An MD simulation study of Reichardt's betaines in surfactant micelles: Unlike orientation and solvation of cationic, zwitterionic, and anionic dye species within the pseudophase. // Kharkiv Univ. Bull., Chem. Ser. 2018. Vol.30, No.53. P.27–35. https://doi.org/10.26565/2220-637X-2018-30-03

14. Farafonov V. S., Lebed A. V., Mchedlov-Petrossyan N. O. Examining solvatochromic Reichardt's dye in cationic micelles of different size via molecular dynamics. // Vopr. Khim. Khim. Tekhnol. 2018. Vol.5. P.62–68.

15. Mathias E. V., Liu X., Franco O., Khan I., Ba Y., Kornfield J. A. Model of Drug-Loaded Fluorocarbon-Based Micelles Studied by Electron-Spin Induced 19F Relaxation NMR and Molecular Dynamics Simulation. // Langmuir 2008. Vol.24, No.3. P.692–700.

16. Aliaga C., Bravo-Moraga F., Gonzalez-Nilo D., Márquez S., Lühr S., Mena G., Rezende M. C. Location of TEMPO derivatives in micelles: subtle effect of the probe orientation. // Food Chemistry 2016. Vol.192. P.395–401.

17. Giampaolo A. D., Cerichelli G., Chiarini M., Daidone I., Aschi M. Structure and solvation properties of aqueous sulfobetaine micelles in the presence of organic spin probes: a Molecular Dynamics simulation study. // Struct. Chem. 2013. Vol.24. P.945–953.

18. Kyrychenko A., Ladokhin A. S. Molecular Dynamics Simulations of Depth Distribution of Spin-Labeled Phospholipids within Lipid Bilayer. // J. Phys. Chem. B 2013. Vol.117, No.19. P.5875–5885.

19. Laudadio E., Galeazzi R., Mobbili G., Minnelli C., Barbon A., Bortolus M., Stipa P. Depth Distribution of Spin-Labeled Liponitroxides within Lipid Bilayers: A Combined EPR and Molecular Dynamics Approach. // ACS Omega 2019. Vol.4, No.3. P.5029–5037.

20. Stoica I. Force field impact and spin-probe modeling in molecular dynamics simulations of spin-labeled T4 lysozyme. // J. Mol. Model. 2005. Vol.11. P.210–225.

21. Oganesyan V. S., Chami F., White G. F., Thomson A. J. A combined EPR and MD simulation study of a nitroxyl spin label with restricted internal mobility sensitive to protein dynamics. // J. Magn. Reson. 2017. Vol.274. P.24–35.

22. Mukerjee P., Ramachandran C., Pyterl R. A. Solvent Effects on the Visible Spectra of Nitroxides and Relation to Nitrogen Hyperfine Splitting Constants. Nonempirical Polarity Scales for Aprotic and Hydroxylic Solvents. // J. Phys. Chem. 1982. Vol.86, No.16. P.3189–3197.

23. Grieser F., Drummond C. J. The Physicochemical Properties of Self-Assembled Surfactant Aggregates As Determined by Some Molecular Spectroscopic Probe Techniques. // J. Phys. Chem. 1988. Vol.92, No.20. P.5580−5593.

24. Vanquelef E., Simon S., Marquant G., Garcia E., Klimerak G., Delepine J. C., Cieplak P., Dupradeau F.-Y. R.E.D. Server: a web service for deriving RESP and ESP charges and building force field libraries for new molecules and molecular fragments. // Nucleic Acids Res. 2011. Vol.39. P.511–517.

В.С. Фарафонов, А.В. Лебедь. Нитроксильный спиновый зонд в ионных мицеллах: Молекулярно-динамическое моделирование.

Харьковский национальный университет имени В.Н. Каразина, химический факультет, пл. Свободы, 4, Харьков, 61022, Украина

Соединения с нитроксильным радикалом (NO˙) активно используются в качестве спиновых зондов для изучения организованных растворов, в том числе липидных мембран и мицелл. Их спектры электронного парамагнитного резонанса предоставляют информацию о составе среды, в частности, о содержании воды в ней. Однако, корректная интерпретация результатов измерений требует понимания микроскопических характеристик молекулярного зонда. В данной статье мы распространяем наши прежние исследования микроскопического состояния кислотно-основных и сольватохромных зондов на спиновые зонды. Мы сообщаем результаты молекулярно-динамического моделирования распространенного спинового зонда, метил-5-доксилстеарата, в мицеллах анионного (*н*-додецилсульфат натрия, ДСН) и катионного (*н*-додецилтриметиламмония бромид, ДТАБ) поверхностно-активных веществ. Локализация молекулы в

зонда в мицеллах обоих видов значительной разницы не выявлено, однако характеристики атома О˙ с неспаренным электроном существенно различаются: в частности, в мицеллах ДТАБ он менее гидратирован и образует меньше водородных связей с водой. Подобная ситуация наблюдается и для группы СОО. Главной причиной этого установлено взаимодействие с катионными головными группами, которые экранируют атом О˙ и группу СОО от воды. Эти наблюдения позволили пересмотреть точку зрения, что поверхностный слой мицелл ДТАБ в целом является менее гидратированным, чем таковой мицелл ДСН.

Ключевые слова: метил-5-доксилстеарат, додецилсульфат натрия, бромид додецилтриметиламмония, локализация, конформация, гидратация, водородная связь.

В.С. Фарафонов, О.В. Лебідь. Нітроксильний спіновий зонд в іонних міцелах: Молекулярно-динамічне дослідження.

Харківський національний університет імені В.Н. Каразіна, хімічний факультет, майдан Свободи, 4, Харків, 61022, Україна

Сполуки з нітроксильним радикалом (NO˙) активно використовуються як спінові зонди для дослідження організованих розчинів, у тому числі ліпідних мембран та міцел. Їх спектри електронного парамагнітного резонансу надають інформацію щодо складу середовища, зокрема, про вміст води в ньому. Втім, коректна інтерпретація результатів вимірювань потребує розуміння мікроскопічних характеристик молекулярного зонда. У даній статті ми поширюємо наші попередні дослідження мікроскопічного стану кислотно-основних та сольватохромних зондів в міцелах поверхнево-активних речовин на спінові зонди. Ми доповідаємо результати молекулярно-динамічного моделювання поширеного спінового зонда, метил-5-доксилстеарата, в міцелах аніонної (*н*-додецилсульфат натрію, ДСН) та катіонної (*н*-додецилтриметиламонію бромід, ДТАБ) поверхнево-активних речовин. Локалізація молекули в міцелах, її форма, склад локального оточення, гідратованість були обчислені та порівняні з наявними відповідними експериментальними даними. Між характеристиками молекулярного зонда в міцелах обох видів значної різниці не знайдено, проте характеристики атома О˙ з неспареним електроном є суттєво відмінними: зокрема, у міцелах ДТАБ він є менш гідратованим та утворює менше водневих зв'язків із водою. Подібна ситуація спостерігається і для групи СОО. Головною причиною цього визначено взаємодію з катіонними головними групами, які екранують атом О˙ та групу СОО від води. Ці знахідки дозволили переглянути точку зору, що поверхневий шар міцел ДТАБ в цілому є менш гідратованим, ніж такий міцел ДСН.

Ключові слова: метил-5-доксилстеарат, додецилсульфат натрію, бромід додецилтриметиламонію, локалізація, конформація, гідратація, водневий зв'язок.

УДК 547.1'128:(542.913+543.42)

SYNTHESIS OF DIETHYL 2-{[3-(TRIETHOXYSILYL)PROPYL]AMINO}ETHYLPHOSPHONATE

Yu.I. Chuyko [a], Yu.V. Kholin [b], M.A. Kolosov [c]

V.N. Karazin Kharkiv National University, School of Chemistry, 4 Svobody sqr., 61022 Kharkiv, Ukraine

a) ✉ chuyko@karazin.ua   https://orcid.org/0000-0002-1552-2106
b) ✉ kholin@karazin.ua   http://orcid.org/0000-0003-1369-741X
c) ✉ kolosov@karazin.ua   http://orcid.org/0000-0002-6714-0513

Diethyl 2-{[3-(triethoxysilyl)propyl]amino}ethylphosphonate is promising reagent for the modification of silica surface and thus for the creation of chelate adsorbents for extraction of *d*-metals ions from water media.

Diethyl 2-{[3-(triethoxysilyl)propyl]amino}ethylphosphonate was synthesized by alkylation of 3-aminopropyltriethoxysilane (APTES) with diethyl vinylphosphonate under quick neat heating. The possible alternative approaches to the synthesis of this compound were investigated (alkylation of APTES and N-acetylAPTES) as well as behavior of APTES towards heating in absolute ethanol and THF. APTES was shown to be not stable in absolute ethanol, that is caused by polycondensation processes. Because of this fact, previously reported protocol of diethyl 2-{[3-(triethoxysilyl)propyl]amino}ethylphosphonate synthesis in ethanol turned to be impossible.

Keywords: 3-aminopropyltriethoxysilane (APTES), alkylation, polycondensation, surface modification.

Introduction

3-Aminopropyltriethoxysilane (APTES) is a widely used agent for development of robust hydrophobic coatings on glass surface [1, 2] and, in general, for obtaining of 3-(aminopropylsilyl)modified surfaces [3–6].

Two general pathways are used for the synthesis of 3-(aminopropylsilyl)modified silica: grafting and sol-gel synthesis. Grafting process consists of reaction of silanol groups on the surface of silica and APTES [7–9], while the sol-gel procedure is the simultaneous hydrolytic condensation of APTES with tetraethoxysilane (TEOS) [10–12]. Moreover, 3-aminopropyl groups on the surface may be further functionalized [13, 14]. However, such "double grafting" on the surface inevitably leads to uneven filling of the surface layer with both modified and unchanged amino and silanol groups, and the control of this process is quite difficult.

We have lately proposed a general strategy for *N*-modified 3-(aminopropyl)silica synthesis, which consisted of *N*-prefunctionalization of APTES with hydrolytically, air and time stable functional groups and further synthesis of surface-modified silica on the base of the latter precursor. In our previous work we worked up the synthesis of diethyl {[3-(triethoxysilyl)propyl]amino}-methylphosphonates, which after grafting of SiO$_2$ surface and further hydrolysis should produce sorption material with five-membered chelate binding structure [15].

The purpose of the present work is to obtain, starting from APTES, diethyl 2-{[3-(triethoxysilyl)propyl]amino}ethylphosphonate **1** which after a grafting of SiO$_2$ or sol-gel synthesis in reaction with TEOS should create a layer of the uniform substituted 2-(phosphonatoethyl)amino groups on the silica surface, producing after the stage of acidic hydrolysis a promising six-membered chelate binding structures (Figure 1).
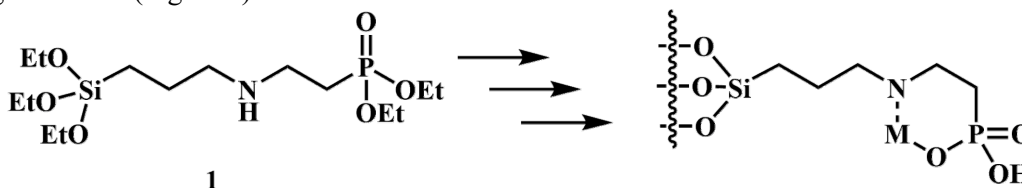
Figure 1. Structure of the target diethyl 2-{[3-(triethoxysilyl)propyl]amino}ethylphosphonate **1** and estimated structure of chelate complexes.

Results and discussion

The synthesis of the compound **1** is described in literature, but full characterization is given in the only article [16] while the other publications contain incomplete spectral data [17–19] or information about mixtures obtaining [20]. The synthesis reported by the authors [16] consisted of simple heating of APTES with diethyl vinylphosphonate **2** in absolute EtOH for 24 h. (Scheme 1).
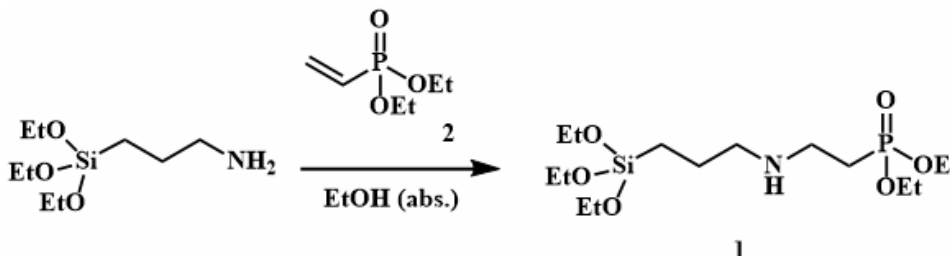
Scheme 1. Reported pathway of compound **1** synthesis [16].

First we reproduced the protocol, cited in ref. [16]. Starting APTES was commercially available, and diethyl vinylphosphonate **2** was obtained in two stages, starting from commercially available triethyl phosphite and 1,2-dibromoethane through the synthesis of intermediate diethyl 2-bromoethylphosphonate **3** (analogously to data [21–25]), Scheme 2.
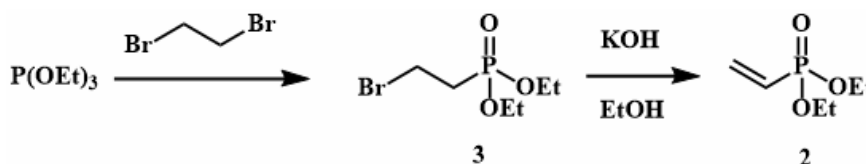
Scheme 2. Synthesis of diethyl vinylphosphonate **2**.

However, it turned out that the samples of the reaction mixture, taken sequentially during heating (according to Scheme 1), indicate not only the formation of the target product **1**, but the gradual disappearance of EtO-groups near the silicon atom, indicating the polycondensation of APTES and/or reaction product **1** (Figure 2).
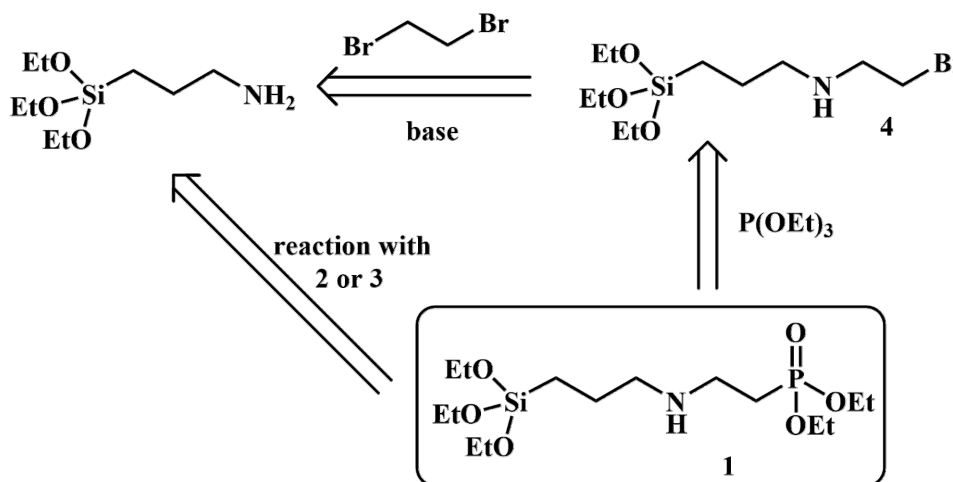
Scheme 3. Retrosynthetic analysis of the compound **1** as secondary amine (starting from APTES).

We assumed that such a process should occur spontaneously in absolute EtOH as in a proton donor solvent. We tested our hypothesis by heating APTES at a bath temperature of 70°C a) in absolute THF (dried over molten potassium); b) in absolute EtOH (dried under activated zeolites). It turned out that in absolute EtOH after 13 h. of heating the processes that indicate polycondensation of APTES took place (decreasing of EtO-groups signals intensity in ^{1}H NMR spectrum). In contrast, according to

^{1}H NMR spectrum, no changes happened with the original APTES after heating it in absolute THF for 24 h. and removal of the solvent.

This, unfortunately, testified about the unreliability of the publication data [16] and the need to develop a protocol for the synthesis of compound **1** from the beginning.

The obvious common pathways for the synthesis of the compound **1** as secondary amine starting from APTES (primary amine) are shown on the Scheme 3 (retrosynthetic scheme is given), Scheme 3.
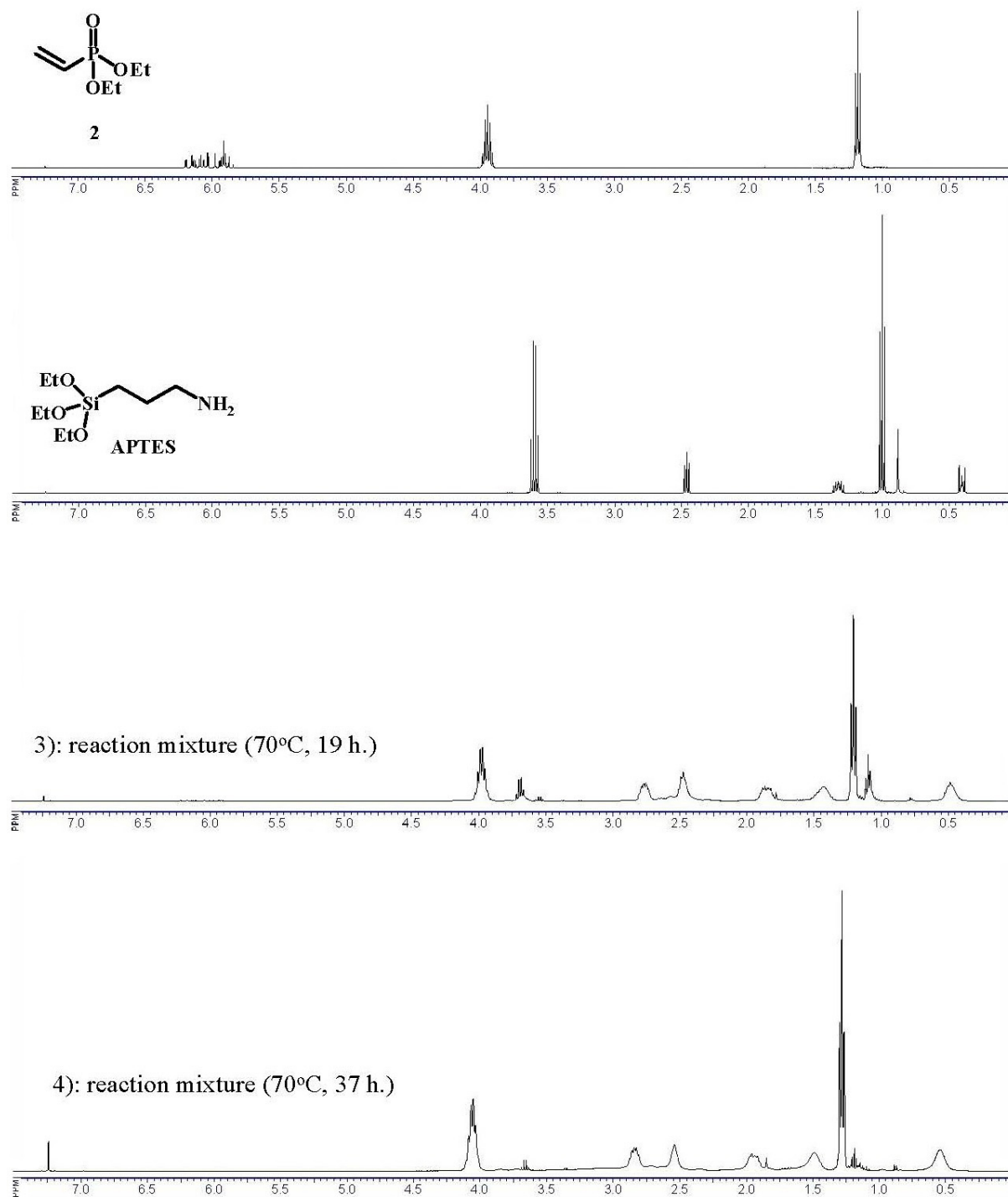
Figure 2. ^{1}H NMR spectra (CDCl$_3$): 1) diethyl vinylphosphonate **2**; 2) APTES; 3) the reaction mixture (ethanol was removed by vacuum distillation) after 19 h. of heating at 70°C under argon; 4) the reaction mixture (ethanol was removed by vacuum distillation) after 37 h. of heating at 70°C under argon.

Noteworthy, that the most obvious drawback of these pathways is possible poly-*N*-alkylation of APTES with 1,2-dibromoethane, ethyl vinylphosphonate **2** or diethyl 2-bromoethylphosphonate **3**.

That is why we also considered the alkylation of compound **5** (obtained by APTES acetylation) by compound **2** or **3** as a synthetic route of the nearest precursor of compound **1** – substance **6** (Scheme 4).
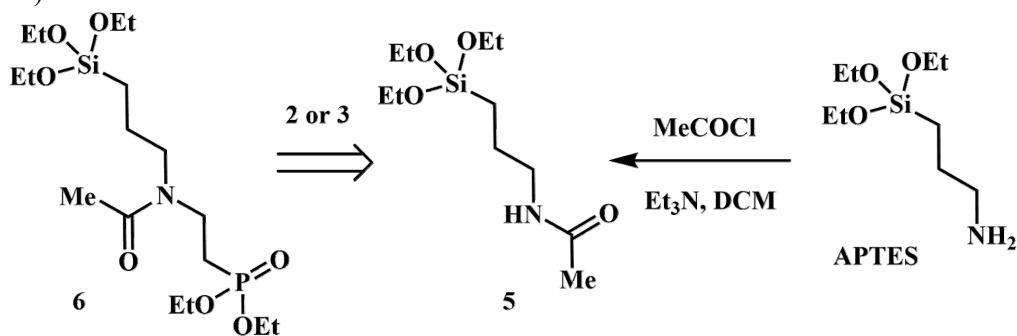
Scheme 4. Retrosynthetic analysis of the compound **6**.

N-Acetyl group of compound **6** should be completely removed after grafting on the surface of SiO_2 and subsequent acid hydrolysis, so compounds **1** and **6** are synthetically equivalent in the case of surface-modified silica obtaining. Generally, the pathway of the synthesis of secondary amine derivatives starting from secondary amides seemed more selective and convenient, comparing with the synthesis of compounds **1** and **4** by direct alkylation of APTES.

We studied the interaction of compound **5** with diethyl 2-bromoethylphosphonate **3** in systems traditionally used for *N*-alkylation of amides: a) $CHCl_3$, NEt_3 (r. t.); b) K_2CO_3, methyl ethyl ketone (reflux); c) NaH, THF (r. t.). After treatment of the reaction mixtures it was found that alkylation of compound **6** did not occur in any case (established by ^{1}H NMR ($CDCl_3$)), and the only new component of the mixtures was ethyl vinylphosphonate **2**, which was apparently formed by the elimination of HBr from compound **3**.

Since the side formation of ethyl vinylphosphonate **2** was obvious because of using diethyl 2-bromoethylphosphonate **3** in basic media, we performed model alkylations of compound **5** with available bromides, which are unable to eliminate HBr under mild basic conditions, in different media (Table 1). Absolute solvents were used, syntheses were performed in an inert atmosphere.

Table 1. Model alkylation of compound **5**.
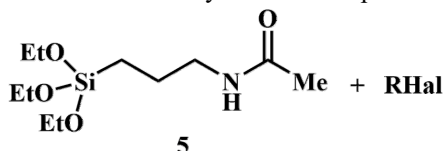
RHal	Reaction conditions
n-BuBr	K_2CO_3, methyl ethyl ketone, 90ºC
n-BuBr	NaH, THF, 25ºC
n-BuBr	NaH, DMF, 25ºC
1-Bromo-3-chloropropane	NaH, THF, 25ºC
1-Bromo-3-chloropropane	NaH, DMF, 25ºC
Diethyl 3-chloropropylphosphonate (**7**)	K_2CO_3, DMF (50ºC, 2 h.; then 80ºC, 2 h.; then 100ºC, 2 h.; then 120ºC, 2 h.)

Unfortunately, in any case the result was negative, and the starting compound **5** was returned back in the amount of 50–70 %.

We attribute such a passivity of amide **5** in the basic media to the formation of an anion, which is stabilized by intramolecular complexation by the silicon atom (due to the reversibility of the process after work-up of the reaction mixtures the starting material is regenerated, Scheme 5).
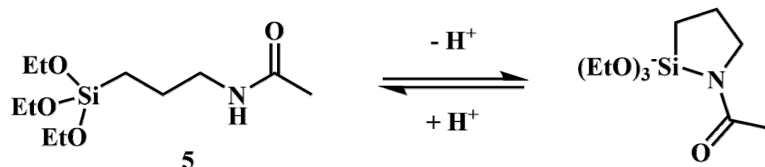
Scheme 5. Possible explanation of the stability of *N*-anion of amide **5**.

As we previously expected, attempts to obtain the *N*-butyl derivatives of APTES by its direct alkylation in K_2CO_3/THF and K_2CO_3/DMF systems at reflux also failed due to the formation of complex mixtures of reaction products.

Thus, the only reaction we still counted on was alkylation (Michael addition) of APTES with diethyl vinylphosphonate **2**, but the reaction conditions had to be investigated, keeping in mind the negative result of the process in absolute ethanol.

We expected, that the positive result should consist primarily of the quantitative (90 % or more) yield of the target compound **1**, because the formation of a significant number of possible impurities (e.g., products of *N*,*N*-dialkylation of APTES) should lead to extreme difficult purification of compound **1** by vacuum distillation (its estimated boiling point is about 170ºC at 0.1 mm Hg). Purification of the target compound **1** by recrystallization was definitely not possible (viscous oil at room temperature), and the use of chromatographic methods was impossible due to the interaction of compound **1** with the surface of the sorbent. More, compound **1** was assumed to be hydrolytically unstable, and this fact caused additional inconvenience to work with it. Additionally, the obvious disadvantage of using DMAP as organic base (instead of DIPEA) was the difficulty of its removal by vacuum/distillation from the reaction mixture because of involatility, which should cause the presence of inevitable and undesirable impurities. Noteworthy, that ^{1}H NMR spectra of all the synthesized compounds and reaction mixtures were measured in $CDCl_3$, because APTES and its derivatives are hydrolyzed even by water, containing in $(CD_3)_2SO$.

The results of the experiments are summarized in Table 2. The conditions and the result of the most successful experiment are highlighted in bold.

Interestingly, that the most convenient approach to the successful synthesis of the target compound **1** turned out to be instant immersion of the flask with the stirred mixture of the reagents without any catalyst in hot oil bath.

^{1}H NMR spectrum of the target compound **1** is given in the Figure 3.
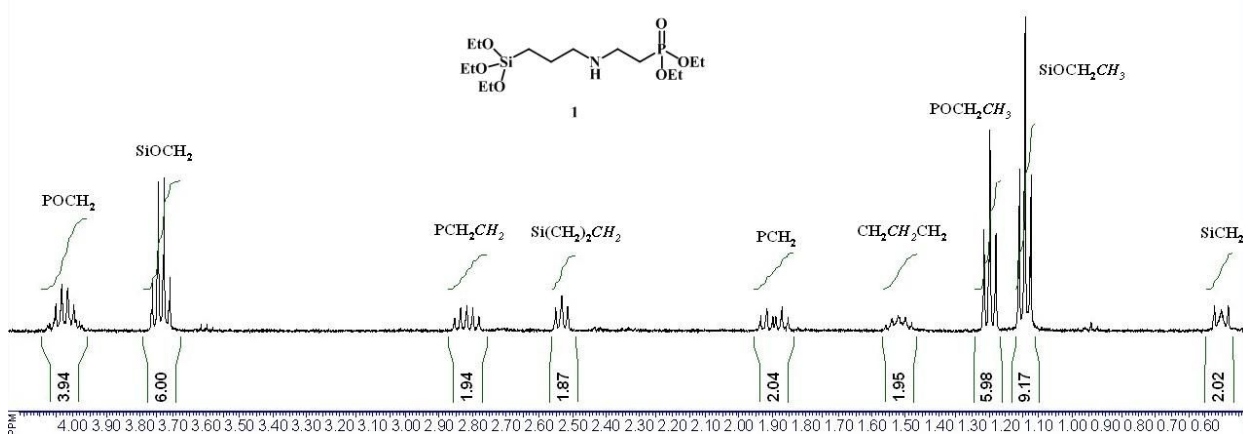
Figure 3. ^{1}H NMR spectrum of the target compound **1** ($CDCl_3$).

The ^{1}H NMR spectrum of the compound **1** contains signals of EtO-groups of both ester fragments and separate signals of each of the five CH_2-groups (see Figure 3 and Experimental part). Noteworthy, that the signals of protons of PCH_2- and $POCH_2$-groups are multiplets due to the spin-spin coupling of the corresponding protons and ^{31}P nuclei.

Compound **1** is a viscous liquid, sensitive to water. However, compound **1** is stable over time (at least for several months) in the absence of moisture and in an inert atmosphere, as evidenced by identical ^{1}H NMR spectra of samples taken immediately after its synthesis and after prolonged storage.

Table 2. Interaction of APTES with diethyl vinylphosphonate **2**.
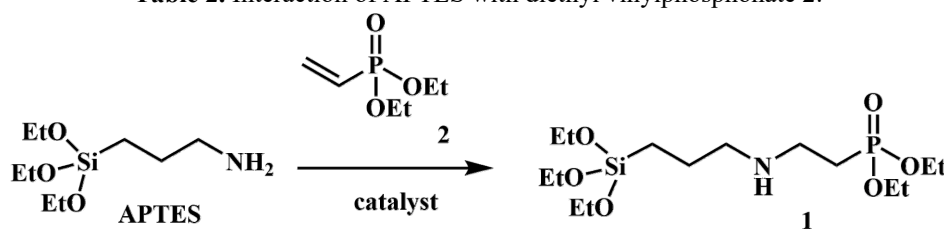
№	Molar ratio APTES : 2	Catalyst, 10 mol. % (if any)	Time, min.	Temperature of the bath, ºC	Time of reaching the temperature, min.	Purity of compound 1 after vacuum distillation, %	Amount of compound 1 in the reaction mixture (according to ^{1}H NMR data, $CDCl_3$, mol. %)
1	1:1	–	60	100	10	–	traces
2	1:1	–	120	100	10	–	64
3	1:1	–	240	100	10	–	64
4	1:1	–	180	100	10	85[3]	65
5	3:1	–	660	100	10	–	58
6	1:1	DMAP[1]	120	100	10	–	55
7	1:1	DMAP[1]	480	100	10	–	30
8	1:1	DIPEA[2]	120	100	10	85[3,4]	45
9	1:1	DIPEA[2]	480	70	7	85[3,4]	60
10	1.5:1	DIPEA[2]	120	100	10	85[3,4]	47
11	1:1.5	DIPEA[2]	120	100	10	85[3,4]	55
12	1:1	DIPEA[2]	120	20	0	–	0[5]
13	1:1	DIPEA[2]	240	20	0	–	5[5]
14	1:1	DIPEA[2]	360	20	0	–	10[5]
15	1:1	DIPEA[2]	120	40	4	–	0[5]
16	1:1	DIPEA[2]	120	60	6	–	8[5]
17	1:1	DIPEA[2]	120	80	8	–	12[5]
18	1:1	DIPEA[2]	120	100	10	–	16[5]
19	**1:1**	**–**	**120**	**100**	**instantly[6]**	**97**	**85**

[1] DMAP – 4-dimethylaminopyridine. [2] DIPEA – di(*i*-propyl)ethylamine. [3] 170ºC, 0.1 mm Hg (see Experimental). [4] Yield after distillation of combined samples (entries 8–11). [5] As mixture with starting compounds. [6] Immersion of a flask with the stirred reaction mixture in an oil bath of a given temperature.

Conclusion

As a result, we proposed a suitable protocol of the synthesis of diethyl 2-{[3-(triethoxysilyl)propyl]amino}ethylphosphonate by alkylation of APTES with diethyl vinylphosphonate under quick heating and further mixing at 100ºC in neat. Additionally, the impossibility of carrying out the processes with APTES derivatives in absolute EtOH due to their polycondensation was shown.

Experimental

^{1}H NMR spectra were registered in $CDCl_3$ (δ_H = 7.26 ppm) and in $(CD_3)_2SO$ (δ_H = 2.50 ppm) at 400 MHz using Varian MR-400 spectrometer with $Si(CH_3)_4$ as an internal standard, chemical shifts are given in ppm, coupling constants are given in Hz. Resonance multiplicity was described as s (singlet), t (triplet), q (quartet), m (multiplet) and br (broad signal). Syntheses with APTES derivatives were performed in argon (99.993 %) atmosphere. Starting APTES, acetyl chloride, 1,2-dibromoethane, triethyl phosphite, DMAP, DIPEA, triethylamine, 1-bromo-3-chloropropane, inorganic reagents and solvents were commercially available. Silica of 400–230 mesh (40–60 μm) by Swambe Chemicals was used. APTES was distilled under reduced pressure before use and stored under argon. Acetyl chloride was distilled under atmospheric pressure before use and stored under argon. All the solvents for the synthesis with APTES (except hexane) were dried over active zeolites. Activation of zeolites (CaA and NaA from «Reakhim») was performed by 400ºC during 3 h., then cooling in

desiccator over KOH. THF was dried over KOH and distilled over molten potassium before use. Dichloromethane (DCM) was dried over K_2CO_3. Triethylamine was dried over KOH. K_2CO_3 was activated by heating at 400ºC for 3 h., then cooled in desiccator over KOH. Ethanol was dried over K_2CO_3, then over active zeolites and stored over active zeolites. Diethyl 2-bromoethylphosphonate **3** was obtained as shown elsewhere [22–24], diethyl vinylphosphonate **2** was obtained analogously to been reported [21, 25].

3-(*N*-Acetylamino)propyltriethoxysilane 5. A solution of CH_3COCl (7.8 g, 99 mmol) in 40 ml of dry CH_2Cl_2 was added under cooling (ice/water) during 5 min. to the solution of APTES (20 g, 90 mmol) and NEt_3 (12.0 g, 119 mmol) in 200 ml of dry CH_2Cl_2. The resulting mixture was stirred for 12 h., then washed 5 times with 120 ml of water, 250 ml of 1% water solution of HCl, 250 ml of saturated water solution of $NaHCO_3$ and twice with 100 ml of saturated water solution of NaCl. Organic phase was dried over Na_2SO_4. After filtration and evaporation of the solvent 19.5 g (82 %) of colorless oil **5** was obtained. ^1H NMR ($CDCl_3$), δ, ppm (*J*, Hz): 6.02 (1H, br. s, NH), 3.76 (6H, q, *J* = 7.2, OCH_2), 3.13–3.21 (2H, m, CH_2N), 1.91 (3H, s, $COCH_3$), 1.51–1.62 (2H, m, *CH₂*CH_2N), 1.16 (3H, t, *J* = 7.2, *CH₃*CH_2), 0.55–0.61 (2H, m, CH_2Si).

Diethyl 3-chloropropylphosphonate 7. A mixture of triethyl phosphite (20.0 g, 0.12 mol) and 1-bromo-3-chloropropane (38.0 g, 0.24 mol) was heated to reflux with Dean-Stark trap during 5 h. The mixture was cooled and distilled under 15 mm Hg. The fraction with boiling point of 140–150ºC was collected and 11.1 g (43 %) of colorless liquid **7** were obtained. ^1H NMR ((CD_3)$_2$SO), δ, ppm (*J*, Hz): 3.90–4.08 (4H, m, $POCH_2$), 3.52–3.70 (2H, m, CH_2Cl), 1.60–2.20 (4H, m, $(CH_2)_2P$), 1.19 (6H, t, *J* = 7.2, CH_3).

Diethyl 2-{[3-(triethoxysilyl)propyl]amino}ethylphosphonate 1. A well-stirred homogeneous mixture of APTES (7.0 g, 31.6 mmol) and diethyl vinylphosphonate **2** (5.19 g, 31.6 mmol) was quickly immersed in preheated (100ºC) oil bath. Stirring and heating continued during 2 h. Reaction mixture was cooled and distilled at 0.1 mm Hg. The fraction with boiling point of 163–171 ºC was collected and 7.80 g (64 %) of viscous colorless oil **1** was obtained. ^1H NMR ($CDCl_3$), δ, ppm (*J*, Hz): 3.95–4.09 (4H, m, $POCH_2$), 3.74 (6H, q, *J* = 7.2, $SiOCH_2$), 2.77–2.87 (2H, m, *CH₂*CH_2P), 2.53 (2H, t, *J* = 7.2, $Si(CH_2)_2CH_2$), 1.83–1.96 (2H, m, CH_2P), 1.47–1.57 (2H, m, CH_2*CH₂*CH_2), 1.25 (6H, t, *J* = 7.2, *CH₃*CH_2OP), 1.14 (9H, t, *J* = 7.2, *CH₃*CH_2OSi), 0.51–0.59 (2H, m, CH_2Si).

References

1. Dey T., Naughton D. Cleaning and anti-reflective (AR) hydrophobic coating of glass surface: a review from materials science perspective. *J. Sol-Gel Sci. Technol.* **2016**, 77, 1–27.
2. Hossain Md. M., Trinh Q. H., Nguyen D. B., Sudhakaran M. S. P., Mok Y. S. Robust hydrophobic coating on glass surface by an atmospheric-pressure plasma jet for plasma-polymerisation of hexamethyldisiloxane conjugated with (3-aminopropyl) triethoxysilane. *Surf. Eng.* **2019**, 35, 466–475.
3. Panteleimonov A., Tkachenko O., Baraban A., Benvenutti E., Gushikem Y., Kholin Y. Probing silica-organic hybrid materials using small probes: Simulation of adsorption equilibria influenced by cooperativity effects. *Adsorpt. Sci. Technol.* **2013**, 67(1), 145–154.
4. Delafosse G., Patrone L., Goguenheim D. J. Functionalization of Silicon Dioxide Surface with 3-Aminopropyltrimethoxysilane for Fullerene C_{60} Immobilization. *J. Nanosci. Nanotechnol.* **2011**, 11, 9310–9315.
5. Howarter J. A., Youngblood J. P. Optimization of silica silanization by 3-aminopropyltriethoxysilane. *Langmuir* **2006**, 22, 11142–11147.

6. Buszewski B., Jezierska M., Wełniak M., Kaliszan R. Cholesteryl-silica stationary phase for liquid chromatography: Comparative study of retention behavior and selectivity. *J. Chromatogr. A*. **1999**, 845, 433–445.
7. Zaitsev V. N., Vasilik L. S., Evans J., Brough A. Synthesis and structure of the grafted layer on silicas chemically modified by aminophosphonic acids. *Russ. Chem. Bull*. **1999**, 48, 2315–2320.
8. Zhu M., Lerum M. Z., Chen W. How To Prepare Reproducible, Homogeneous, and Hydrolytically Stable Aminosilane-Derived Layers on Silica. *Langmuir* **2012**, 28, 416–423.
9. Vrancken K. C., Possemiers K., Van Der Voort P., Vansant E. F. Surface modification of silica gels with aminoorganosilanes. *Coll. Surf. A*. **1995**, 98, 235–241.
10. Chen S., Hayakawa S., Shirosaki Y., Fujii E., Kawabata K., Tsuru K., Osaka A. Sol–Gel Synthesis and Microstructure Analysis of Amino-Modified Hybrid Silica Nanoparticles from Aminopropyl-triethoxysilane and Tetraethoxysilane. *J. Am. Ceram. Soc.* **2009**, 92, 2074–2082.
11. Zhi K., Wang L., Zhang Y., Jiang Y., Zhang L., Yasin A. Influence of Size and Shape of Silica Supports on the Sol–Gel Surface Molecularly Imprinted Polymers for Selective Adsorption of Gossypol. *Materials* **2018**, 11, E777.
12. Lecoq E., Duday D., Bulou S., Frache G., Hilt F., Maurau R., Choquet P. Plasma Polymerization of APTES to Elaborate Nitrogen Containing Organosilicon Thin Films: Influence of Process Parameters and Discussion About the Growing Mechanisms. *Plasma Process. Polym.* **2013**, 10, 250–261.
13. Nomura A., Yamada J., Tsunoda K. Acylation of Aminopropyl-Bonded Silica Gel for Liquid Chromatography. *Anal. Sci.* **1987**, 3, 209–212.
14. Silveira G. Q., Ronconi C. M., Vargas M. D., San Gil R. A. S., Magalhães A. Modified silica nanoparticles with an Aminonaphthoquinone. *J. Braz. Chem. Soc.* **2011**, 22(5), 961–967.
15. Kolosov M. A., Chuyko Yu. I., Kulyk O. G., Mazepa A. V., Zavarzin V. V., Kholin Yu. V. α-Aminophosphonate derivatives of triethoxysilane for the synthesis of surface-modified silica *Synth. Commun.* **2020**, 50, 123–128.
16. Schmider M., Mu1 E., Klee J. E., Mülhaupt R. A Versatile Synthetic Route to Phosphonate-Functional Monomers, Oligomers, Silanes, and Hybrid Nanoparticles. *Macromolecules* **2005**, 38, 9548–9555.
17. Bugerenko Ye. F., Petukhova A. S., Chernyshev Ye. A. Sintez kremniyfosforsoderzhashih soedineniy prisoedineniem po dvoynoy uglerod-uglerodnoy svyazi. *Zhurn. Obsh. Khim*. **1970**, 40, 606–609.
18. Chernyshev Ye. A., Bugerenko Ye. F., Petukhova A. S. Pat. of USSR 242168 (1969).
19. Klee J. E., Lehmann U., Walz U. Int. pat. WO 03/070198 A1 (2003).
20. Jain R., Rimer J. D. Seed-Assisted zeolite synthesis: The impact of seeding conditions and inter-zeolite transformations on crystal structure and morphology. *Micropor. Mesopor. Mat*. **2020**, 300, 110174.
21. Fourgeaud P., Midrier C., Vors J.-P., Volle J.-N., Pirat J.-L., Virieux D. Oxaphospholene and oxaphosphinene heterocycles via RCM using unsymmetrical phosphonates or functional phosphinates. *Tetrahedron* **2010**, 66, 758–764.
22. Tang Xi., Zhong Q., Xu J., Li H., Xu S., Cui X., Wei B., Ma Y., Yuan R. $Co(II)_4Gd(III)_6$ phosphonate grid and cage as molecular refrigerants. *Inorg. Chim. Acta* **2016**, 442, 195–199.
23. Cichowicz N. R., Nagorny P. Synthesis of Conjugated Polyenes via Sequential Condensation of Sulfonylphosphonates and Aldehydes. *Org. Lett*. **2012**, 14, 1058–1061.
24. Li X., Chen X., Yuan J., Liu Y., Li P., Qu L., Zhao Y. An Efficient Synthesis of 1,2,3-Triazole Bridge-Connected Phosphonate Derivatives of Coumarin. *Phosphorus Sulfur Silicon Relat. Elem.* **2015**, 190, 961–971.
25. Lukáč M., Garajová M., Mrva M., Devínsky F., Ondriska F, Kubincová J. Novel fluorinated dialkylphosphonatocholines: Synthesis, physicochemical properties and antiprotozoal activities against *Acanthamoeba* spp. *J. Fluor. Chem.* **2014**, 164, 10–17.

Ю.И. Чуйко, Ю.В. Холин, М.А. Колосов. Синтез диэтил-2-{[3-(триэтоксисилил)пропил]амино}этилфосфоната.

Харьковский национальный университет имени В.Н. Каразина, химический факультет, пл. Свободы, 4, Харьков, 61022, Украина

Диэтил 2-{[3-(триэтоксисилил)пропил]амино}этилфосфонат – перспективный реагент для модификации поверхности кремнеземов и, таким образом, создания адсорбентов для извлечения ионов d-металлов из водных сред.

Диэтил-2-{[3-(триэтоксисилил)пропил]амино}этилфосфонат был синтезирован путем алкилирования 3-аминопропилтриэтоксисилана (APTES) диэтилвинилфосфонатом при быстром нагревании без растворителя. Были исследованы возможные альтернативные подходы к синтезу этого соединения (алкилирование APTES и N-ацетилAPTES), а также поведение APTES при нагревании в абсолютном этаноле и тетрагидрофуране. Показано, что APTES нестабилен в абсолютном этаноле, что вызвано процессами поликонденсации. Из-за этого факта ранее описанный подход к синтезу диэтил-2-{[3-(триэтоксисилил)пропил]-амино}этилфосфоната в этаноле оказался невозможным.

Ключевые слова: 3-аминопропилтриэтоксисилан (APTES), алкилирование, поликонденсация, модификация поверхности.

Ю.І. Чуйко, Ю.В. Холін, М.О. Колосов. Синтез діетил-2-{[3-(тріетоксисиліл)пропіл]аміно}етилфосфонату.

Харківський національний університет імені В.Н. Каразіна, хімічний факультет, майдан Свободи, 4, Харків, 61022, Україна

Діетил-2-{[3-(тріетоксисиліл)пропіл]аміно}етилфосфонат – перспективний реагент для модифікації поверхні кремнеземів і, таким чином, створення хелатних адсорбентів для вилучення іонів d-металів з водних середовищ.

Задум отримання діетил-2-{[3-(тріетоксисиліл)пропіл]аміно}етилфосфонату, як і інших функціональних N-похідних 3-амінопропілтріетоксисилану (APTES), полягає в отриманні шляхом органічного синтезу конкретної речовини (прекурсора) з надійно доведеною структурою, стабільної впродовж тривалого часу при зберіганні за кімнатної температури; ця сполука після одноразового прищеплення на поверхню кремнезему формує шар однотипних функціональних груп (вторинних аміногруп та залишків фосфонової кислоти, поєднаних вуглеводневим ланцюгом), стабільних у водному середовищі, на повітрі та у часі. Такий підхід вигідно відрізняється від поетапного прищеплення APTES та взаємодії поверхні APTES-модифікованих кремнеземів з певними реагентами, оскільки в останньому випадку після кожної стадії залишається незміненою частина поверхневих груп вихідного сорбенту, а будова функціональних груп є неоднозначною.

Діетил-2-{[3-(тріетоксисиліл)пропіл]аміно}етилфосфонат був синтезований шляхом алкілування APTES діетилвінілфосфонатом при швидкому нагріванні без розчинника. Окрім того, було досліджено можливі підходи до синтезу цієї сполуки (алкілування APTES і N-ацетилAPTES у різних умовах, які використовуються для N-алкілювання, відповідно, амінів та амідів), але, нажаль, усі вони не призвели до бажаного результату. Зокрема, негативний результат алкілування N-ацетилAPTES у присутності основи ми пояснюємо формуванням пасивного циклічного Si-вмісного аніону. Вивчено також поведінку APTES при нагріванні в абсолютному етанолі та тетрагідрофурані. Показано, що APTES нестабільний в абсолютному етанолі (зменшення кількості EtOSi-груп у спектрах [1]H ЯМР), що, вірогідно, викликано процесами поліконденсації, тому описаний раніше підхід до синтезу діетил-2-{[3-(тріетоксисиліл)пропіл]аміно}етилфосфонату в етанолі виходячи з APTES та діетилвінілфосфонату виявився неможливим.

Ключові слова: 3-амінопропілтріетоксисилан (APTES), алкілування, поліконденсація, модифікація поверхні.

УДК 547.7/8

ПОИСК НОВЫХ ЛЮМИНОФОРОВ С ЗАДАННЫМИ ФИЗИКО-ХИМИЧЕСКИМИ И ХИМИЧЕСКИМИ СВОЙСТВАМИ
XIV. N-АРИЛМЕТИЛЕН- И N-ГЕТАРИЛМЕТИЛЕНПРОИЗВОДНЫЕ ПОЛИ(3-АМИНОПРОПЕНА)

А.П. Шкумат [a], А.А. Зимина [b]

Харьковский национальный университет имени В.Н. Каразина, химический факультет, пл. Свободы, 4, Харьков, 61022, Украина

a) ✉ *shkumat@karazin.ua*   *https://orcid.org/0000-0001-9705-6235*
b) ✉ *zymina.ana@gmail.com*   *https://orcid.org/0000-0003-3624-7817*

Исследована возможность создания флуоресцирующих полимеров производных поли(3-аминопропена) (ПАП) путем алкилирования аминогрупп флуоресцирующими ароматическими или гетероциклическими альдегидами по реакции Лейкарта-Валлаха. Синтез N-алкилированных производных ПАП проводили путем последовательного превращения: акриламид → ПАА ($Mv = 100$ кДа) → ПАП → алкилированный ПАП. Вследствие невозможности использовать $LiAlH_4$ для восстановления амидных групп полиакриламида до аминных из-за низкой растворимости полимера в неводных (диэтиловый эфир, тетрагидрофуран и др.) растворителях проведена оптимизации восстановления ПАА другими восстановителями. Установлено, что наилучшие условия для восстановления амидных групп ПАА до аминных – уксусная кислота – диоксан как растворитель и $NaBH_4$ (суспендированный в безводном 1,4–диоксане) как восстановитель. По данным ИК спектроскопии полученные продукты – сополимеры 3-аминопропена (основное количество элементарных звеньев), акриламида и акриловой кислоты. Для модифицирования строения полученного полимера использовали реакцию Лейкарта-Валлаха, где в качестве альдегидов, обладающих люминесценцией были выбраны: пирен-3-альдегид, 2-гидрокси-1-нафтальдегид, антрацен-9-карбальдегид и 3,5 фенил-1-(4-формилфенил)-2-пиразолин. Для получения N-Ar/Het-метиленовых производных смесь ПАП, альдегида и 98 % муравьиной кислоты нагревали в жестких условиях (6 часов, глицериновая баня), выделяли и очищали. Полученные модифицированные образцы полимеров интенсивно флуоресцируют как в твердом состоянии, так и в виде растворов, что указывает на успешное прохождение реакции Лейкарт-Валлаха. Спектральные характеристики получены для растворов в смешанном растворителе – этилацетат – муравьиная кислота (9 : 1). Как для исходных альдегидов так и для сополимеров в используемом смешанном растворителе спектральные кривые флуоресценции теряют колебательную структуру, вероятно, из-за влияния смешанного растворителя на молекулы люминофора (для исходных альдегидов) и боковые метиламино-N-арилметиленовые -[...-CH_2-CH(CH_2—NH-CH_2-Ar)-] и метиламино-N-гетарилметиленовые [-CH_2-CH(CH_2—NH-CH_2-Het)- ...) группы как в основном так и в возбужденном состоянии, а для полимеров неоднородности среды с локальными зонами полярности.

Ключевые слова: синтез, поли(3-аминопропен), полиаллиламин, ПАП, люминофоры, ИК-спектры, спектры поглощения и флуоресценции.

Поли(3-аминопропен) (ПАП) или, чаще используемое, исторически сложившееся название, полиаллиламин (ПААм) – в отличие от ядовитого мономера, нетоксичный, механически достаточно прочный полимер волокнистой структуры, который применяется, например, в бумажной промышленности (для увеличения прочности бумаги), а также является ценным материалом для целого ряда биомедицинских применений. Так, на основе ПАП синтезируют полимерные хелатные смолы, а также сорбционные волокна. Но даже не модифицированный ПАП с его функциональными группами может быть использован для селективного удаления ионов меди (II) от ионов других тяжелых металлов [1–4]. Таким образом, ПАП и его сополимеры представляет большой интерес в связи с возможностью его простой модификацией путем алкилирования, ацилирования или других преобразований аминогруппы.

Получение ПАП и его сополимеров определенной молекулярной массы, кроме традиционной полимеризации аллиламина, возможно путем полимеризации акриламида в среде апротонного растворителя (инициатор – 2,2'-азобис(изобутиронитрил) или пероксид бензоила) [5] и последующего восстановления полиакриламида (ПАА) до ПАП. В этом случае возможно получение скорее сополимера аллиламина и акриламида. Однако наличие остаточных амидных

групп в этом случае будет полезным для сохранения частичной водорастворимости образую-
щегося продукта. Мы решили исследовать возможность модификации строения ПАП путем
последовательного превращения: акриламид → ПАА → ПАП → алкилированный ПАП с целью
получения новых флуоресцирующих материалов.

Полученный ПАА по методике описанной в нашей работе [5] с молекулярной массой
100 кДа (определено вискозиметрически) использовали для дальнейших его превращений в
ПАП:
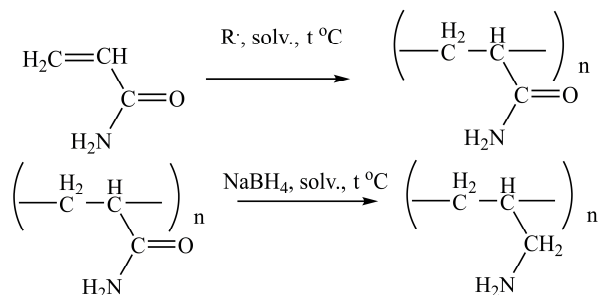
Схема 1. Схема синтеза поли(3-аминопропена)

К сожалению, использовать LiAlH$_4$ для восстановления амидных групп ПАА до аминных
оказалось невозможным, из-за низкой растворимости полимера в неводных растворителях (ди-
этиловый эфир, тетрагидрофуран и др.). В результате проверки многочисленных вариантов
восстановления амидных групп ПАА мы пришли к выводу, что наилучшие условия для восста-
новления амидных групп ПАА до аминных и, пожалуй, безальтернативные – уксусная кислота
как растворитель и NaBH$_4$ (суспендированный в безводном 1,4–диоксане) как восстановитель.
Об образовании ПАП при восстановлении ПАА мы можем утверждать по данным ИК спектров
для ПАА и ПАП в области 1600–1650 и 2200–3700 см$^{-1}$ (рис. 1) – изменение интенсивности
соответствующих полос поглощения – CONH$_2$ полиакриламида и NH$_2$ групп
поли(3-аминопропена) (Рис. 1). Выделенный и очищенный ПАП (многократной промывкой
этиловым спиртом) использовали для дальнейшей модификации.
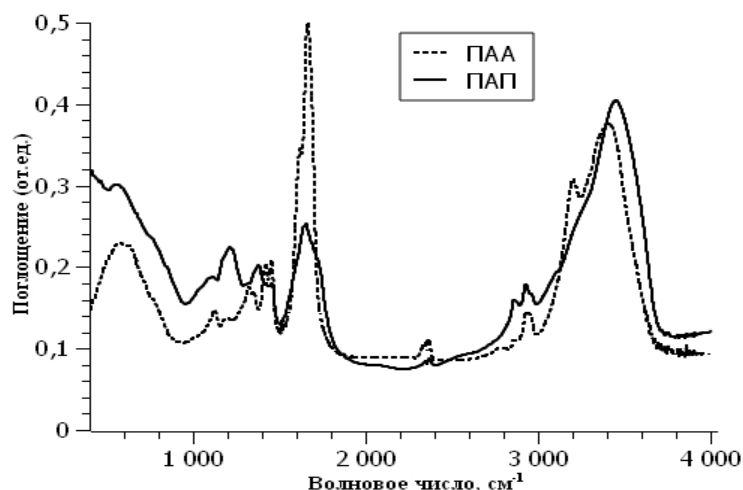
Рисунок 1. ИК спектры ПАА и ПАП (сополимер аллиламина – акриламида – акриловой кислоты : ПАП)
(табл. KBr)

На спектрограммах ПАА и ПАП (Рис. 1) в области 1600–1800 см$^{-1}$ наблюдается уменьшение
интенсивности ассиметричной мало структурированной полосы с максимумом в области
1652 см$^{-1}$ полосы поглощения CONH$_2$– групп от 0.5 до 0.24. Её незначительная асимметрич-
ность в сторону больших значений волновых чисел указывает на присутствие в синтезирован-
ном полимере некоторого количества карбоксильных групп, образовавшихся в результате по-
бочной реакции гидролиза амидных групп (из данных ИК-спектров количественно установить
соотношение карбоксильных и амидных групп не представляется возможным). Кроме того в
области 3100–3700 см$^{-1}$ наблюдается изменение формы структурированной полосы поглоще-

ния, которая обусловлена поглощением аминогрупп, как свободных так и связанных с карбоксильными группами сильными водородными связями и на их фоне полос поглощения, обусловленными колебаниями скелетных CH_2- i $CH-$ групп. Обращает на себя внимание также и факт появление новых полос поглощения при 1200 и 1380 см$^{-1}$. При 1445 см$^{-1}$ наблюдается изменение формы и интенсивности расположенных рядом полос, обусловленные деформационными колебаниями CH_2- i $CH-$ групп, в связи с появлением новых CH_2-групп, которые образовались в результате восстановления амидных групп до метиленаминных. Следует отметить, что точная интерпретация всех полос поглощения полимеров в области 1000-1600 см$^{-1}$ невозможна, т.к. это область «отпечатков пальцев».

Для модифицирования строения полученного полимера (сополимера аллиламина – акриламида – акриловой кислоты: ПАП) мы использовали реакцию Лейкарта-Валлаха:
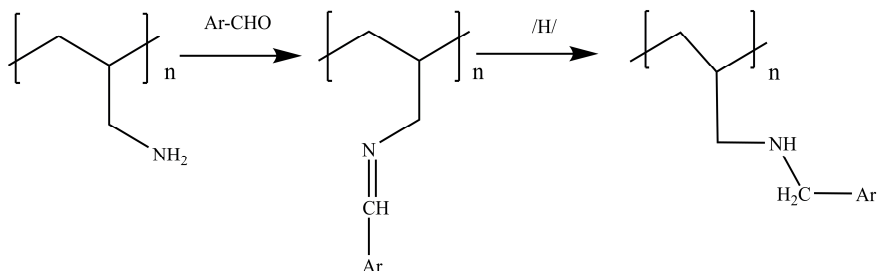
Схема 2. Модификация поли(3-аминопропена) по реакции Лейкарта-Валлаха.

В качестве альдегидов, обладающих люминесценцией, были выбраны:

a.   пирен-3-альдегид – соединение **Iа**;
b.   2-гидрокси-1-нафтальдегид – соединение **IIа**;
c.   антрацен-9-карбальдегид – соединение **IIIа**;
d.   3,5 фенил-1-(4-формилфенил)-2-пиразолин – соединение **IVа**.

В результате получены модифицированные полимерные образцы –**Iп, IIп, IIIп, IVп**.

Формулы модифицированных элементарных звеньев представлены ниже:
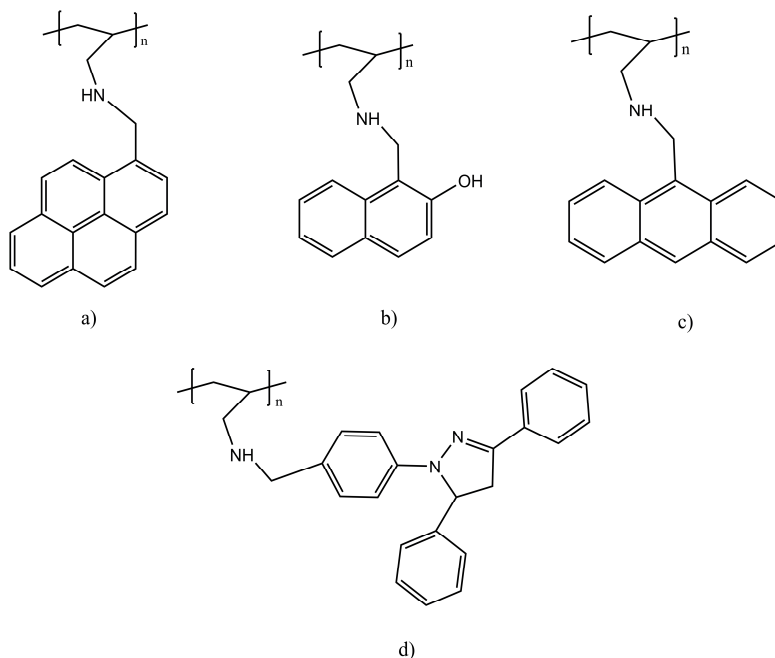
Рисунок 2. Формулы модифицированных элементарных звеньев сополимера ПАП, соответственно: a) пирен-3-альдегидом, b) 2-гидрокси-1-нафтальдегидом, c) антрацен-9-карбальдегидом, d) 3,5 фенил-1-(4-формилфенил) -2- пиразолином.

Взаимодействие элементарных звеньев, содержащих аминогруппы, полимера и указанных выше альдегидов проводили в среде муравьиной кислоты (и как растворителя и как восстано-

вителя) в достаточно жестких условиях (длительное кипячение на глицериновой бане, последующая отгонка муравьиной кислоты на 50–70%, а иногда до 90%). После длительного кипячения (6 часов) реакционной смеси, состоящей из модифицированного полимера, ароматического (или гетероциклического) альдегида, обладающих люминесценцией, и муравьиной кислоты, взятой в избытке, последующей отгонкой части муравьиной кислоты, густой вязкий остаток (с целью исключение из образца модифицированного ПАП избыточного количества молекул люминофоров, которые не вступили в реакцию), двукратно обрабатывали ацетоном, ацетон отделяли, продукт сушили, проверяли на чистоту (наличие остаточных количеств альдегидов ТСХ методом). Степень превращения зависит от условий проведения реакции и её длительности.

На ИК спектрах для модифицированных образцов ПАП (соответственно пирен-3-альдегидом, 2-гидрокси-1-нафтальдегидом, 9-антральдегидом и 3,5 фенил-1-(4-формилфенил)-2- пиразолином) за счет вклада поглощения ароматических ядер и уменьшения количества свободных аминогрупп в области 1500–1650 (I_1) и 2400–3700 (I_2) см$^{-1}$ изменяется форма, а также соотношение полос поглощения (I_1/I_2) (соответственно 0.55, 0.705, 0.81 та 0.865), более четко проявляются полосы поглощения в области деформационных колебаний (1450–1460 см$^{-1}$), а также несколько изменяется форма и положение составляющих полосы поглощения в области 3000–3600 см$^{-1}$. Однако, более существенные изменения видны в области 1000–1550 см$^{-1}$ (на рисунке 3 область обведена овалом) в связи с изменившимся количеством одинарных связей и проявлением новых деформационных колебаний.
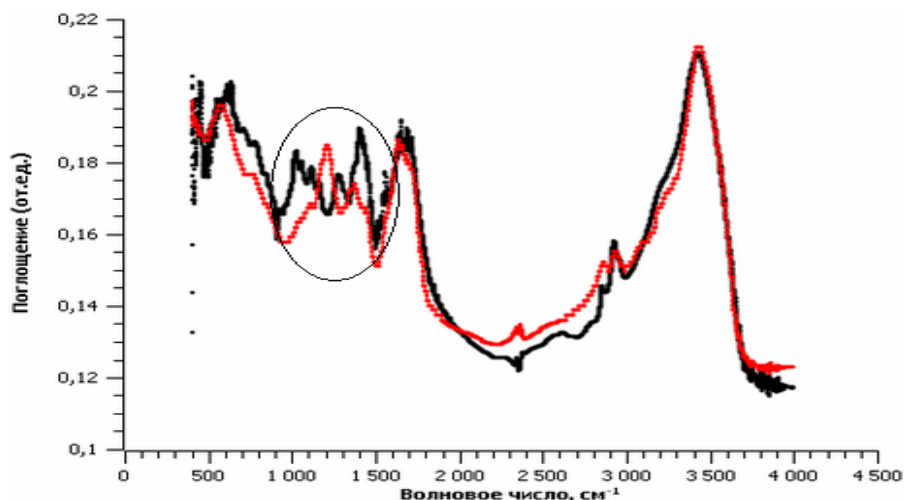
Рисунок 3. Сравнение ИК спектров поглощения сополимера ПАП (черная кривая) и продукта 3,5-фенил-1-(4-формилфенил)-2-пиразолином (соед. **IVп**) (красная кривая)

Полученные модифицированные образцы полимеров интенсивно флуоресцируют как твердом состоянии, так и в виде растворов, что указывает на прохождение реакции Лейкарт-Валлаха. Установлено, что наилучшая растворимость сополимеров достигается в смешанном растворителе этилацетат – муравьиная кислота (9 : 1). Растворы получены путем последовательного растворения навески полимера в муравьиной кислоте, а затем разбавления полученного раствора этилацетатом. Данные о спектрах поглощения и люминесценции приведены в таблице 1. Пример спектральных кривых для соединения **IVа** и полимера **IVп** приведены на рисунке 4.

При анализе спектров поглощения и флуоресценции обращает на себя внимание тот факт, что как для исходных альдегидов так и для сополимеров в используемом смешанном растворителе спектральные кривые флуоресценции теряют колебательную структуру, вероятно, из-за специфического влияния смешанного растворителя на молекулы люминофора (для исходных альдегидов) и боковые метиламино-N-арилметиленовые -[...-CH$_2$-CH(CH$_2$-NH-CH$_2$-Ar)-] и метиламино-N-гетарилметиленовые [-CH$_2$-CH(CH$_2$-NH-CH$_2$-Het)- ...) группы как в основном так и в возбужденном состоянии. Каждая группа имеет собственное окружение ближайшими фрагментами макромолекул, имеющих сложное конформационное строение, и собственное ближайшее окружение молекулами растворителя. Следовательно, хромофоры модифицированных

образцов находятся в неоднородной среде с локальными зонами различной полярности и из-за этого структурная релаксация различных хромофоров образца проходит неодинаково, и полосы флуоресценции получаются размытыми.
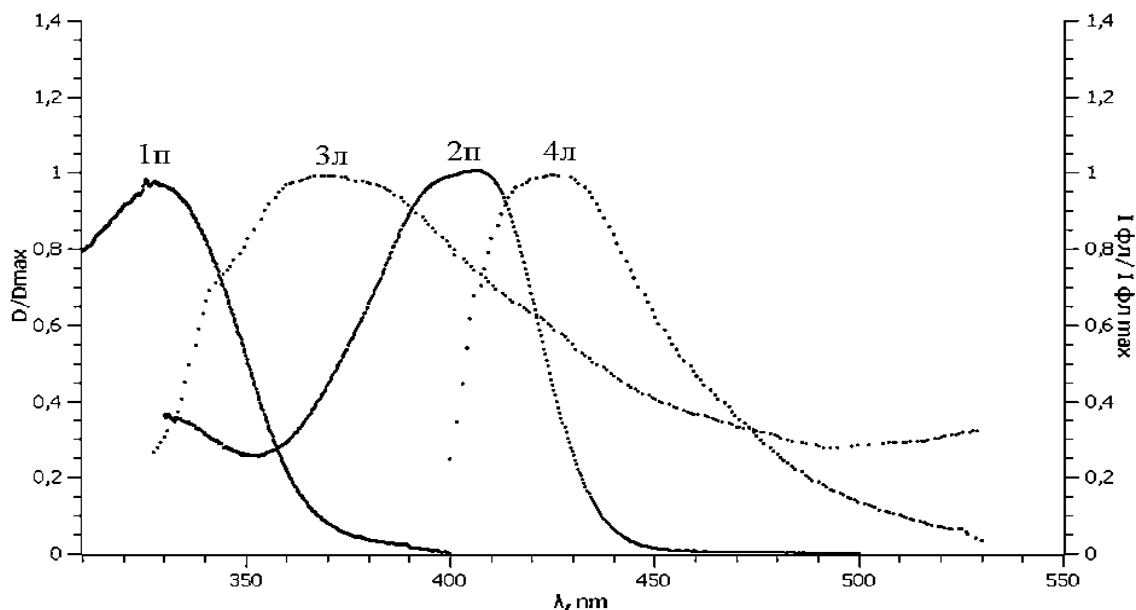
Рисунок 4. Спектры поглощения и флуоресценции IVa и IVп: **1·п** 3,5-фенил-1-(4-формилфенил)-2-пиразолина; **2·п** ПАП модиф. 3,5-фенил-1-(4-формилфенил)-2-пиразолином; **3·л** 3,5-фенил-1-(4-формилфенил)-2-пиразолина; **4·л** ПАП модиф. 3,5-фенил-1-(4-формилфенил)-2-пиразолином (где **п** - поглощение; **л** – люминесценция)

Таблица 1. Спектральные характеристики исходных люминофоров и модифицированных продуктов (растворитель: этилацетат – муравьиная кислота (9 : 1))

№	Поглощение, λ, нм		Люминесценция, λ, нм	
Соед. (превращение)	Альдегида	Модифицированного полимера	Альдегида	Модифицированного полимера
Ia→ Iп	382	381	460	459
IIa→ IIп	376	377	423	432
IIIa→ IIIп	390	395	512	513
IVa→ IVп	326	405	371	426

Экспериментальная часть

ИК-спектры измеряли на ИК-спектрометре с преобразованием Фурье Nicolet iS5 в диапазоне волновых чисел 4000–400 см$^{-1}$ для твердого состояния (таблетки KBr).

Спектры поглощения растворов альдегидов и полимерных продуктов измеряли на спектрофотометре Hitachi-U 3210, а спектры флуоресценции на спектрофлуориметре Hitachi-850. Из-за низкой растворимости полимерных продуктов использовали смешанный растворитель (этилацетат – муравьиная кислота (9 : 1)).

Синтез ПАА. К раствору акриламида в этилацетате (2 г на 50 мл) прибавляли инициатор полимеризации (бензоилпероксид – 0.2 г) и смесь нагревали с обратным холодильником в течение 2-х часов. Полученный полимер растворяли в воде, осаждали ацетоном и сушили. Очищенный от олигомеров ПАА с молекулярной массой 100 кДа (определяли вискозиметрически) использовали для дальнейших превращений.

Синтез ПАП. К раствору ПАА в ледяной уксусной кислоте (5 г на 100 мл) при интенсивном перемешивании порциями (через 0.5 часа, скорость прибавления ограничивается бурным выделение газа) добавляли 10 г NaBH$_4$, суспендированного в 1,4-диоксане. Общее время прибавления и последующего перемешивания – 4.5 часа. Реакционную смесь нагревали с обратным хо-

лодильником в течение еще 3-х часов. Смесь расслаивалась, смолу отделяли и высушивали. Полученный белый продукт промывали этиловым спиртом, измельчали и кипятили со спиртом в течение 2-х часов. Очищенный полимер высушивали, анализировали на наличие аминогрупп и использовали для последующей модификации.

Модификация ПАП. Смесь ПАП и альдегида последовательно растворяли в 98%-ной муравьиной кислоте, кипятили на глицериновой бане (температура бани 150 ^{O}C) в течение 6-ти часов, далее 50–70% (иногда до 90%) муравьиной кислоты отгоняли, из полученного вязкого остатка ацетоном осаждали сырой модифицированный полимер. Для удаления избыточного, не вступившего в реакцию, альдегида продукт переосаждали путем двукратной промывки горячим ацетоном и сушили.

Выводы

1. Восстановлением ПАА боргидридом натрия в среде уксусная кислота – диоксан получен сополимер полиаминопропена, акриламида и акриловой кислоты (сополимер ПАП). Химическое превращение подтверждено данными ИК спектров образцов полимеров и дальнейшими процессами их модификации.

2. Показано, что одним из методов модификации аминогрупп сополимера ПАП является реакция Лейкарта-Валлаха. Взаимодействием аминогрупп ПАП с ароматическими или гетероциклическими альдегидами получены производные ПАП с боковыми метиламино-N-арилметиленовыми-[...-CH$_2$-CH(CH$_2$-NH-CH$_2$-Ar)-] метиламино-N-гетарилметиленовыми группами [-CH$_2$-CH(CH$_2$-NH-CH$_2$-Het)- ...), где Ar- 3-пиренил, 9-антрил- та 2-гидрокси-1-нафтил- или Het – 4-(3,5-фенил-2-пиразолинил-1)фенил-.

3. Проведено сравнительное исследование и анализ ИК спектров, спектров поглощения и флуоресценции образцов ПАП и модифицированных соединений, которые подтверждают достоверность проведенных химических превращений.

Литература

1. Царик Л.Я., Подкуйко П.А., Олонцева Е.П., Соболева А.В., Подкуйко О.Г., Алексеева О.В., Кульпе Н.В., Ильюшенко Г.А. Способ получения полиаллиламина. РФ. 2013130138/04, 01.07.2013.

2. Zhao H. C. Synthesis and Thermal Property of Poly(Allylamine Hydrochloride). *Advanced Materials Research*. **2011**. 150-151, 1480-1483.

3. Li M., Li Y., Yu L., Sun Y. Characterization of poly(allylamine) as a polymeric ligand for ion-exchange protein chromatography. *Journal of Chromatography*. **2017**, 1486, 103-109.

4. Рычина Т. А. Сорбционные свойства полиаллиламина / Т. А. Рычина, Н. В. Лакиза, А. В. Пестов // Проблемы теоретической и экспериментальной химии : Тезисы докладов XXVIII Российской молодежной научной конференции с международным участием, посвященной 100-летию со дня рождения профессора В. А. Кузнецова (Екатеринбург, 25-27 апреля 2018 г.). – Екатеринбург : Издательство Уральского университета, 2018. – С. 147-147.

5. Шкумат А.П. Поиск новых люминофоров с заданными физико-химическими и химическими свойствами. IX. Новые водорастворимые сополимеры акриламида // *Вісник Харківського національного університету*. 2012. 1026. Хімія. Вип. 21(44); 126 – 133.

References

1. Tsarik L. Ya., Podkujko P. A., Olonceva E. P., Soboleva A.V., Podkujko O. G., Alekseeva O. V., Kul'pe N. V., Il'yushenko G. A. Method of obtaining polyallylamine. Patent RF. 2013130138/04, 01.07.2013 [in Rus].

2. Zhao H. C. Synthesis and Thermal Property of Poly(Allylamine Hydrochloride). *Advanced Materials Research*. **2011**. 150-151, 1480-1483

3. Li M., Li Y., Yu L., Sun Y. Characterization of poly(allylamine) as a polymeric ligand for ion-exchange protein chromatography. *Journal of Chromatography*. **2017**, 1486, 103-109.

4. Rychina T.A, Lakiza N. V., Pestov A. V. Sorption properties of polyallylamine. Problems of theoretical and experimental chemistry: Abstracts of the XXVIII Russian youth scientific conference with international participation. Yekaterinburg: Publishing House of the Ural University, **2018**. P. 147-147 [in Rus].

5. Shkumat A. P. The search of new luminophores with predetermined physical and chemical properties. IX. New water-soluble co-polymers of acrylamide. *Kharkiv Univ. Bull., Chem. Ser.* **2012**, 21, 126-133 [in Rus].

А.П. Шкумат, А.О. Зиміна. Пошук нових люмінофорів із заданими фізико-хімічними і хімічними властивостями. XIV.N-Арилметилен- и N-гетарилметиленпохідні полі(3–амінопропена).

Харківський національний університет імені В.Н. Каразіна, хімічний факультет, майдан Свободи, 4, Харків, 61022, Україна

Досліджено можливість створення полімерів, що мають флуоресценцію, похідних полі(3-амінопропена) (ПАП) шляхом алкілування аміногруп ароматичними або гетероциклічними альдегідами по реакції Лейкарта-Валлаха з власною флуоресценцією. Синтез N-алкільованих похідних ПАП проводили шляхом послідовного перетворення: акриламід → ПАА (Mv = 100 кДа) → ПАП → алкільовані ПАП.

Внаслідок неможливості використовувати LiAlH$_4$ для відновлення амідних груп поліакриламіду до амінних через низьку розчинність ПАА в неводних (діетиловий ефір, тетрагідрофуран і ін.) розчинниках проведена оптимізація відновлення ПАА іншими відновниками. Встановлено, що найкращі умови для відновлення амідних груп ПАА до амінних – оцтова кислота - діоксан як розчинник і NaBH$_4$ (суспендований в безводному 1,4-діоксані) як відновник.

За даними ІК спектроскопії отримані продукти - сополімери 3-амінопропена (основна кількість елементарних ланок), акриламіду і акрилової кислоти. Для модифікування будови отриманого полімеру використовували реакцію Лейкарта-Валлаха, де в якості альдегідів, що мають люмінесценцією, були обрані: пірен-3-альдегід, 2-гідрокси-1-нафтальдегід, антрацен-9-карбальдегід і 3,5 феніл-1-(4-формілфеніл) -2-піразолін.

Для отримання N-Ar/Het-метиленових похідних суміш ПАП, альдегіду і 98 % мурашиної кислоти нагрівали в жорстких умовах (6 годин, гліцеринова баня), виділяли і очищали. Отримані модифіковані зразки полімерів інтенсивно флуоресцирують як у твердому стані, так і у вигляді розчинів, що вказує на успішне проходження реакції Лейкарт-Валлаха.

Спектральні характеристики отримані для розчинів у змішаному розчиннику - етилацетат - мурашина кислота (9 : 1). Як для вихідних альдегідів, так і для сополімерів, у використовуваному змішаному розчиннику спектральні криві флуоресценції втрачають коливальну структуру, ймовірно, через специфічний вплив змішаного розчинника на молекули люмінофора (для вихідних альдегідів) і бічні метиламіно-N-арилметиленові - […CH$_2$-CH(CH$_2$-NH-CH$_2$-Ar)- …] і метиламіно-N-гетарилметиленові […-CH$_2$-CH(CH$_2$-NH-CH$_2$-Het)-…) групи як в основному так і в збудженому стані, а для полімерів неоднорідності середовища з локальними зонами полярності.

Ключові слова: синтез, полі(3-амінопропен), поліаліламін, ПАП, люмінофори, ІЧ-спектри, спектри поглинання і флуоресценції.

A.P. Shkumat, A.O. Zymina. Search for new luminophores with predetermined physicochemical and chemical properties. XIV.N-Arylmethylene- and N-hetarylmethylene derivatives of poly (3–aminopropene).

V.N. Karazin Kharkiv National University, School of Chemistry, 4 Svobody sqr., 61022 Kharkiv, Ukraine

The possibility of creating polymers with fluorescence, derivatives of poly (3-aminopropene) (PAP) by alkylation of amino groups with aromatic or heterocyclic aldehydes by Leykart-Wallach reaction with own fluorescence was investigated. Synthesis of N-alkylated PAP derivatives was performed by sequential conversion: acrylamide → PAA (Mv = 100 kDa) → PAP → alkylated PAP.

Due to the impossibility of using LiAlH$_4$ to reduce the amide groups of polyacrylamide to amine due to the low solubility of PAA in the non-aqueous (diethyl ether, tetrahydrofuran, etc.) solvents, the reduction of PAA by other reducing agents was optimized. It was found that the best conditions for the reduction of amide groups of PAA to amine - acetic acid - dioxane as a solvent and NaBH$_4$ (suspended in anhydrous 1,4-dioxane) as a reducing agent.

According to IR spectroscopy, the products obtained are copolymers of 3-aminopropene (the main amount of elementary units), acrylamide and acrylic acid. To modify the structure of the obtained polymer, the Leuckart-Wallach reaction was used, where the following aldehydes having luminescence were selected: pyrene-3-aldehyde, 2-hydroxy-1-naphthaldehyde, anthracene-9-carbaldehyde, and 3.5 phenyl-1-(4-formylphenyl)-2-pyrazoline.

To obtain N-Ar/Het-methylene derivatives, a mixture of PAP, aldehyde and 98% formic acid was heated under harsh conditions (6 hours, glycerol bath), isolated and purified. The obtained modified samples of polymers are intensely fluorescent both in the solid state and in the form of solutions, which indicates the successful passage of the Leykart-Wallach reaction.

Spectral characteristics were obtained for solutions in a mixed solvent – ethyl acetate – formic acid (9 : 1). For both the original aldehydes and the copolymers in the mixed solvent used, the spectral fluorescence curves lose their oscillatory structure, probably due to the specific effect of the mixed solvent on the phosphor molecules (for the original aldehydes) and the side methylamino-N-arylmethylene - […CH$_2$-CH(CH$_2$-NH-CH$_2$-Ar)- …] and methylamino-N-getarylmethylene […-CH$_2$-CH(CH$_2$-NH-CH$_2$-Het)-…] groups both in the ground and in the excited state, and for polymers of inhomogeneity of the medium with local polarity zones.

Keywords: synthesis, poly(3-aminopropene), polyallylamine, PAP, luminophores , IR spectra, absorption and fluorescence spectra.

УДК 543.442.5

АТОМНО-АБСОРБЦІЙНЕ ТА АТОМНО-ЕМІСІЙНЕ З ІНДУКТИВНО-ЗВ'ЯЗАНОЮ ПЛАЗМОЮ ВИЗНАЧЕННЯ ПЛЮМБУМУ ТА ФЕРУМУ В ПЛАСТОВИХ ВОДАХ З ВИКОРИСТАННЯМ НОВИХ СЕРЕДОВИЩ ТА СТАНДАРТНИХ ЗРАЗКІВ СКЛАДУ

О.І. Юрченко [a], Т.В. Черножук [b], О.А. Кравченко [c]

Харківський національний університет імені В.Н.Каразіна, хімічний факультет, майдан Свободи, 4, Харків, 61002, Україна

a) ✉ yurchenko@karazin.ua   https://orcid.org/0000-0002-7117-4556
b) ✉ tanya.chernozhuk@gmail.com   https://orcid.org/0000-0001-5580-7838
c) ✉ alekseykravch@ukr.net   https://orcid.org/0000-0003-1211-2459

Вивчено вплив концентрації поверхнево-активної речовини (Тритон Х-100) та часу обробки ультразвуком на величину аналітичного сигналу при атомно-абсорбційному та атомно-емісійному з індуктивно-зв'язаною плазмою визначенні аналітів в пластових водах. Найбільший аналітичний сигнал при визначенні Плюмбуму та Феруму досягнуто при використанні неіоногенної поверхнево-активної речовини, яка дозволяє зменшити поверхневий натяг аналізованого розчину та збільшити адсорбційність при визначенні аналітів. Показано, що при використанні сучасної пробопідготовки чутливість атомно-абсорбційного визначення Плюмбуму збільшується у 1.5, а Феруму в 1.8 рази. Методами атомно-абсорбційної та атомно-емісійної спектроскопії з індуктивно-зв'язаною плазмою визначено вміст Плюмбуму та Феруму в пластових водах з використанням ацетилацетонатів плюмбуму та феруму як стандартних зразків складу, що дозволило значно підвищити прецизійність та точність визначення аналітів. Шляхом варіювання об'єму зразку та методом «введено –знайдено» показано, що систематична похибка не значна. Узгодженість результатів, отриманих двома незалежними методами, оцінено за F– та t– критеріями. Показано, що дисперсії однорідні, а розбіжність середніх не значна та виправдана випадковим розкидом. Атомно-абсорбційним методом оцінено межу виявлення аналітів за розробленою методикою, та показано, що отримані результати нижче літературних. Розроблена методика, за метрологічними характеристиками, є конкурентоздатною на світовому рівні.

Ключові слова: пластові води, пробопідготовка, атомно-абсорбційна та атомно-емісійна з індуктивно-зв'язаною плазмою спектроскопія, Плюмбум, Ферум, Тритон Х-100, ультразвук, ацетилацетон, ацетилацетонати феруму та плюмбуму, метрологічні характеристики.

Вступ

При видобутку вуглеводнів пластову воду зазвичай вважають небажаним побічним продуктом. Аналіз зразків пластової води може дати життєво важливу інформацію для плану розробки родовищ, включаючи оптимізацію конструкції та закінчуючи вибором матеріалів для вилучення вуглеводнів.

Аналіз води на пласті грає роль в динамічному моделюванні запасів, їх кількісному визначенні та розрахунків вартості завершення проектів, отримати інформацію про те, скільки буде витрачено на обсадну та поверхневу техніку (капітальні витрати). Аналіз води допомагає оператором оцінити експлуатаційні витрати. Кількісна оцінка хімії води допомагає знайти порозуміння зв'язку запасів і характеристику перехідних зон в карбонатах, тим самим впливаючи на оцінку обсягу пласта. Ще допомагає фахівцям з планування визначити, чи можуть нові відкриття бути прив'язані до існуючої інфраструктури і чи мають вони вирішальне значення для розробки проектів хімічного дослідження води. Властивості пластової води можуть бути різними, в залежності від виду колектора [1]. Аналіз мікроелементного складу пластових вод дозволяє визначити наявність родовищ нафти та газу. Вміст таких елементів, як Феруму, Мангану та Цинку дозволяє стверджувати, що дане родовище багате покладами нафти та газу.

Сьогодні найбільш широко використовують для визначення аналітів в багатокомпонентних зразках атомно-абсорбційну та атомно-емісійну спектроскопію з індуктивно-зв'язаною плазмою. Особливу роль відіграють пробопідготовка, нові середовища та стандартні зразки складу. Методики повинні відповідати вимогам «зеленої хімії» [2–25].

Мета роботи – розробити конкуренто здатну методику атомно-абсорбційного та атомно-емісійного з індуктивно-зв'язаною плазмою визначення аналітів в пластових водах з викорис-

танням ультразвукової обробки, водних розчинів поверхнево – активної речовини та β – дикетонів металів як стандартних зразків складу.

Експериментальна частина

В роботі використано атомно-абсорбційний спектрометр i С-115 (полум'яний варіант, лампи з порожнистими катодами, полум'я ацетилен-повітря; атомно-емісійний спектрометр з індуктивно – зв'язаною плазмою i САР 6300 DUO: швидкість плазмо утворюючого потоку Аргону – 12 л/хв, потужність плазми – 1350 Вт, швидкість додаткового потоку Аргону – 1.5 л/хв, режим спостерігання плазми-аксіальний, потік аргону в розпорошувачі – 0.55 л/хв, швидкість обернення насосу – 50 об/хв, час інтегрування сигналу – 20 с, 5 паралельних вимірювань, довжина хвилі, нм: Плюмбум – 220,353; Ферум – 259, 940. Ультразвукова баня, модель PS – 20, потужність – 120 Вт частота – 40 кГц. Ваги лабораторні OHAUS PA 64 (65 / 0.0001 г). Тритон Х-100, $C_{12}H_{22}O(C_2H_4O)_n$, n= 9–10, M_r = 631 г/моль, ККМ = $2.9 \cdot 10^4$ моль/л. Ацетилацетон, ацетилацетонати плюмбуму та феруму. Вихідна концентрація розчинів металів для приготування градуювальник розчинів – 0.1 г/л. Використана дистильована вода та хімічні реактиви кваліфікації не нижче ч.д.а.

Відбирали пластову воду та підкисляли конц. HNO_3 до pH 1.5-2.0. Для аналізу в термостійкий стаканчик відбирали 250 мл води та випарювали до вологого залишку, який розчиняли в 10 мл нітратної кислоти (ω=1.5%), обробляли 20 хв ультразвуком та пробу кількісно переносили в мірну колбу місткістю 25 мл. До отриманого розчину добавляли 2.5 мл, Тритон Х-100 (ω=5%), 0.5 мл. Ацетил- ацетону та доводили до мітки 1.5% HNO_3 і ретельно переміщували.

Результати та їх обговорення

Метали в пластових водах знаходяться у вигляді комплексів з органічними лігандами, склад неорганічних стандартних зразків складу суттєво відрізняється від складу розчинів, що аналізують. Це суттєво впливає на результати визначення аналітів. Тому необхідно замінити неорганічні стандартні зразки на комплекси іонів металів з органічними лігандами. Використовуючи ультразвук, досягається інтенсифікація пробопідготовки. Добавляючи Тритон Х-100 зменшується поверхневий натяг аналізованого розчину та збільшується дисперсність аерозолю, що призводить до повної атомізації. До цього розчину додавали ацетилацетон для утворення ацетилацетонатів аналітів. Градуювальні розчини готували із стандартних розчинів іонів Плюмбуму (МЗС 0526:2003) та Феруму (МЗС 0518:2003), а також із ацетилацетонатів металів. Будували залежність аналітичних сигналів при атомно-абсорбційному визначенні аналітів від їх концентрації та розраховували чутливість як

$$S = tg\alpha = dA / dC . \tag{1}$$

Підвищення чутливості визначали за формулою

$$\Delta S = tg\alpha_2 / tg\alpha_1 , \tag{2}$$

де $tg\alpha_1$ – чутливість при використанні водних розчинів іонів металів, $tg\alpha_2$ – чутливість при визначенні аналітів при додаванні Тритон Х-100 використані ацетилацетанатів металів.

Таким чином, ми підвищили чутливість визначення Плюмбуму в 1.5 рази, а Феруму в 1.8 рази. Використовуючи ацетилацетонати металів як стандартні зразки складу (вони атестовані як стандартні зразки складу ряду підприємств України), наблизили склад аналізованих зразків до градуювальних розчинів, що дало можливість підвищити прецизійність та точність вимірювань.

В табл. 1 наведено дослідження по вибору концентрації ПАР для атомно-абсорбційного визначення аналітів, а табл. 2 – вибір часу обробки зразків ультразвуком.

При використанні Тритон Х-100 (ω=5%) досягається максимум аналітичного сигналу при визначенні аналітів.

Як видно із табл. 2, зразки необхідно обробляти УЗ протягом 20 хв.

В табл. 3 наведено результати атомно-абсорбційного визначення аналітів в пластових водах, в табл. 4 – атомно-емісійного з індуктивно-зв'язаною плазмою, а в табл. 5 – результати перевірки правильності атомно-абсорбційного визначення металів методом «введено – знайдено».

Показано, що методика не містить значних систематичних похибок. Оцінку систематичної похибки оцінено також шляхом варіювання об'єму аналізованого зразку. Проводили розбавлення зразку 1:10; 1:20; та 1:40. Також показано, що значима систематична похибка відсутня.

Проведено співставлення результатів, отриманих двома незалежними методами, за критеріями Фішера та Стьюдента. Показано, що дисперсії однорідні, а розбіжність середніх не значна та виправдана випадковим розкидом.

Оцінено межу виявлення [25] атомно-абсорбційного визначення Плюмбуму: $C_{min} = 0.004$, $C_{лім} = 0.05$ мкт/мл, а для Феруму – $C_{min} = 0.008$, $C_{лім} = 0.015$ мкт/мл.

Таблиця 1. Вибір концентрації Тритон *X*-100 при атомно-абсорбційному визначення Феруму та Плюмбуму *(n=5; p=0.95)*.

w, %	Pb, мг/л		Fe, мг/л	
	$\bar{C} \pm \dfrac{t_{p,f}S}{\sqrt{n}}$	S_r	$\bar{C} \pm \dfrac{t_{p,f}S}{\sqrt{n}}$	S_r
0	9.41±0.11	0.01	297±4	0.01
3	11.61±0.14	0.01	311±4	0.01
4	11.75±0.13	0.01	316±4	0.02
5	11.78±0.12	0.01	370±4	0.01
6	11.78±0.12	0.01	370±5	0.01

Таблиця 2. Вибір часу обробки ультразвуком при атомно-абсорбційному визначені розчинів Плюмбуму та Феруму *(n=5; p=0.95)*.

t, хв	Pb (Тритон X-100), мг/л		Fe (Тритон X-100), мг/л	
	$\bar{C} \pm \dfrac{t_{p,f}S}{\sqrt{n}}$	S_r	$\bar{C} \pm \dfrac{t_{p,f}S}{\sqrt{n}}$	S_r
10	11.09±0.11	0.01	370±5	0.01
15	11.61±0.14	0.01	396±5	0.01
20	11.78±0.13	0.01	448±6	0.02
25	11.78±0.12	0.01	448±6	0.01
30	11.78±0.12	0.01	448±6	0.01

Таблиця 3. Результати атомно-абсорбційного визначення Плюмбуму та Феруму в пластовій воді з використанням Тритон *X*-100, стабілізованих УЗ *(n=5; p=0.95)*.

Pb, мг/л		Fe, мг/л	
$\bar{C} \pm \dfrac{t_{p,f}S}{\sqrt{n}}$	S_r	$\bar{C} \pm \dfrac{t_{p,f}S}{\sqrt{n}}$	S_r
11.78±0.14	0.01	448±6	0.01

Таблиця 4. Результати визначення вмісту Плюмбуму та Феруму методом АЕС-ІЗП в розчинах пластової води з додаванням ПАР, стабілізованих УЗ *(n=5; p=0.95)*.

Pb, мг/л		Fe, мг/л	
$\bar{C} \pm \dfrac{t_{p,f}S}{\sqrt{n}}$	S_r	$\bar{C} \pm \dfrac{t_{p,f}S}{\sqrt{n}}$	S_r
11.78±0.15	0.01	448±6	0.01

Таблиця 5. Перевірка правильності результатів атомно-абсорбційного визначення Плюмбуму та Феруму методом «введено – знайдено» *(n=5; p=0.95)*.

	Вміст, *мг/л*	Введено, *мг/л*	Знайдено, $\bar{C} \pm \dfrac{t_{p,f}S}{\sqrt{n}}$	S_r
Pb	11.78	10.0	21.76±0.27	0.01
Fe	448	500	947±12	0.01

Висновки

Використання водних розчинів Тритон *Х-100* та УЗ-обробки виключає використання токсичних та дорогих реагентів, підвищує стабільність та гомогенність отриманих розчинів, зменшує час аналізу, підвищує чутливість визначення аналітів в 1.5 – 1.8 рази. Стандартні зразки складу на основі ацетилацетонатів металів наближають хімічний склад аналізованих зразків до градуювальник розчинів, що дозволяє підвищити прецизійність та точність вимірювань.

Література

1. Бурюкін Ф.А., Гавголенко Н.В., Степанова М.А., Костішина А.І. Проведення комплексних досліджень пластової води Ванкорського родовища. В *Молодь і наука: збірник матеріалів VII Всеросійської науково-технічної конференції студентів, аспірантів і молодих вчених, присвячений 50-річчю першого польоту людини в космос*, Красноярськ, 2011, с.10-12.
2. Насибуллина О.А. Коррозионные испытания ингибиторов коррозии в условиях низкой обводненности. В *Образование и наука в современных условиях*. Матер. внутривуз. науч. – практ. конф. Стерлитамак: Полиграфия, 2016; с. 287 – 288.
3. Гареев, А.Г. *Коррозия и защита металлов в нефтегазовой отрасли*; Уфа: Гилем, Башк. энцикл. 2016.
4. Хусаинова Р.Ф. Коррозия насосно-компрессорных труб в пластовых водах месторождение западной сибири. В *IX международная конференция студентов и молодых ученых «Перспективы развития фундаментальных наук»*. 2012. №9. С. 264.
5. Немец Н. Н., Пантелеймонов А.В., Шугай Е. А., Холін Ю. В. Створення зразка порівняння для візуального бінарного тестування заліза (III) у підземних. *Вісник Харківського національного університету*. **2008**, Хімія.вип.*16(39),* 151 – 158.
6. Басова Е.М., Іванов В.М., Апендеева О.К. Спектрофотометричне визначення тіоцианат-іонів в пластових водах. *Вістн. моск. ун-ту. сер. 2. хімія*. **2014**, 55,15.
7. Юрченко О.І. Титова Н.П., Мандрика Т.С., Добріян М.А., Черножук Т.В. Атомно-абсорбійне та атомно-емісійне з індуктивно-зв'язаною плазмою визначення заліза у нафтопродуктах з використанням ацетилацетонату залізу у якості стандартного зразка складу. *Вісник Харківського національного університету*. **2011**, Хімія.вип.*20(43),* 216.
8. Мариненко А.И., Пеляев О.И. Экспресс-метод определения содержания железа в бензинах. *Химия и технология топлив и масел*. **2008**, *1,* 29 – 31.
9. Кулакова В.В. Использование внутрипластовой очистки подземных вод от железа и марганца (на примере водоснабжения г. Хабаровск). *Вестник ДВЩ РАН*. **2013**, *2,* 85.
10. Юрченко О.И., Титова Н.П., Курочкина Е.М. Выбор способов пробоподготовки нефтепродуктов для атомного спектрального анализа. *Журн. прикл. спектр.* **2010**, *77,2,* 316-320.
11. Темердашева З.В. Исследование и анализ бензинов, измененных в процессах испарения и выгорания. *Заводская лаборатория. Диагностика материалов*. **2008**. *74,4,*4-8.
12. Трофимчук А.К., Латаєва А.В., Чуєнко А.В. Сорбційно-атомно-абсорбційне визначення свинцю у високомінералізованих водах. *Український хімічний журнал*. **2009**,*75,10,* 120-123.
13. Щербанчеко М.Д. Електротермічне атомно-абсорбційне визначення свинцю і кадмію у різноманітних видів спиртів. *Кріміналічтіний вісник*. **2014.** *2 (22),* 190-196.
14. Болдырев К.А., Кузьмин В. В., Куранов Н.П., Билек Ф. Геохимическое моделирование внутрипластового обезжелезивание и деманганации подземных вод. *Водоснабжение и санитарная техника*. **2012,** *4,*49-50
15. Кулаков В.В., Стеблевский В.И., Домин К.В., Херлитциус Й., Тесля В.Г. Опытно-промышленная эксплуатация пилотной установки очистки подземных вод на Тунгусском водозаборе. *Водоснабжение и санитарная техника*. **2012,** *7,*29-35
16. Кулаков В.В. Биогеохимические аспекты очистки подземных вод Приамурья. *Тихоокеан. геология*. **2008,** *27,1,* 109-118.

17. Duyck C., Miekeley N. Trace element determination in crude oil and its fractions by inductively coupled plasma mass spectrometry using ultrasonic nebulization of toluene solutions. *Spectrochimica Acta*, **2008**, *57*,1979-1990.

18. Болдирєв К.А. Геохімічне моделювання внутріпластового знезалізнення і деманганации підземних вод . *Водоснабжение и санитарная техника.* **2013,** *4*,49-55

19. Самтанова Д.Э. Характеристика пластовых вод нефтяних месторождений Республики Калмыкия как приоритетных загрязнителей при нефтедобыче: дисс. к. х. н.: 03.02.08. Иван. гос. хим. технол. ун-т. – Б.м. – 2017. – 175 с.

20. Юрченко А.О. Спектральні методи дослідження .*Наукові та методичні засади фізичної освіти*. **2013**, *1(5),*160-166.

21. Юрченко О.І., Титова Н.П., Сабір Корвані Саліх Сабір, Черножук Т.В.Атомно-абсорбційне та атомно-емісійне з індуктивно зв'язаною плазмою визначення Купруму в нафтопродуктах. *Вісник Харківського національного університету*. **2016**, Хімія.вип.*27(50),* 79-83.

22. Мазняка Н.В., Верхотурова А.П., Лосєва В.Н., Замай Т.Н. Визначення натрію та калію в біологічних об'єктах методами атомно-абсорбційної та атомно-емісійної спектроскопії. *Journal of Siberian Federal University. Chemistry*, **2012,** *3(5),* 320-330.

23. Fischbach F.T. *Manual of Laboratory and Diagnostic Tests.* N.Y.: Lippincott Willians Wilkins, 2008.

24. Белецкая Э.Н. Гигиенические аспекты остеотропности свинца как фактора рика кальцийдефицитной патологии у человека. *Медичні перспективи.* –**2014**, *2,*130-138.

25. Алемасова А.С., Зайцев В.М., Єнальєва Л.Я. *Аналітична хімія*. Донецьк: «Ноулідж»,2010.

26. Алемасова А.С., Рокун А.М., Шевчук І.О. *Аналітична атомно- абсорбційна спектроскопія*. Навчальний посібник. Севастополь: «Вебер», 2003.

References

1. Buryukin F.A., Gavgolenko N.V., Stepanova M.A., Kostishina A.I. Complex investigation of strata water of the Vankorskogo source. Youth and Science: materials of *VII Russian conference of students, postgraduates and young scientists, devoted to the 50 anniversary of the first human space flight.* Krasnoyarsk, **2011**, p.10-12 [in Ukr].

2. Nasibullina O.A. Corrosion testing of corrosion inhibitors under low water conditions. *Education and science in the modern conditions. Materials of scientific conference.* Sterlitamak: Poligrafiya, **2016**; p. 287 – 288 [in Rus]. http://dx.doi.org/10.17122/ngdelo-2019-1-120-123

3. Gareev A.G. Corrosion and protection of metals in the oil and gas industry. Ufa, Gilem, Bashk. encyklopedia. **2016** [in Rus].

4. Husainova R.F. Corrosion of compressor tubes in strata waters of the western Siberia sources. *The IX International Conference of Students and Young Scientists "Prospects for the Development of Fundamental Sciences",* **2012**. *9*. p. 264 [in Rus].

5. Reshetnyak E. A., Nemetz N. N., Panteleimonov A. V., Shugay E. A., Kholin Yu. V.. Development of a reference sample for visual binary testing of Fe(III) in groundwater. *Kharkov Univ. Bull., Chem. Ser.* **2008**, *16,* 151 – 158 [in Ukr].

6. Basova, V.M. Ivanov, O.C. Apendeeva. Spectrophotometric determination of thiocyanate ions in formation waters. *MSU Vestnik*, **2014**, *55*, 15 [in Rus]

7. Yurchenko O.I., Titova N.P., Mandryka T.S., Dobryian M.A., Chernozhuk T.V. Atomic-absorption and atomic-emission with the inductively-coupled plasma detection of iron in the oil products using ferric acetilacetonate as the standard composition sample. *Kharkiv Univ. Bull., Chem. Ser.* **2011**, *20*, 216-221 [in Ukr].

8. Marinenko A.I., Pelyaev O.I Express methods of determination of iron contain in petrol. *Chemistry and Technology of Fuels and Oils*, **2008**, *1*, 29 – 31 [in Rus].

9. Kulakova V.V. Using of intrastrata purification of underground water from iron and manganese. *Vestnik of Far Eastern Branch of Russian Academy of Sciences.* **2013**, *2*, 85 [in Rus].

10. Yurchenko O.I., Titova N.P., Kurochkina E.M. Choose of ways of sample preparation for atomic spectral analysis. *Journ. Appl. Spectroscopy*, **2010**, *77, 2,* 316-320 [in Rus].

11. Temerdasheva Z.V. Investigation and analysis of petrols, changed in processes of burning and evaporation. *Industrial laboratory. Diagnostics of materials.* **2008**, *74, 4*, 4-8 [in Rus].

12. Trofimchuk A.K., Lataeva A.V., Chuenko A.V. Sorbtion atomic absorbtion determination of lead in high miniralized water. *Ukrainian chemistry journal.* **2009**, *75, 10*, 120-123 [in Ukr].

13. Scherbancheko M.D. Electrochemical atomic absorbtion determination of lead and cadmium in various alcohols. *Kryminalistychnyi visnyk.* **2014**. *2 (22)*, 190-196 [in Ukr].

14. Boldyrev K.A., Kuzmin V.V., Kuranov N.P., Bilek F. Geochemical simulation of intrastrata reironing and remanganization of underground water. *Water Supply and Sanitary Technique.* **2012**, *4*, 49-50 [in Rus].

15. Kulakov V.V., Steblevskiy V.I., Domin K.V.,Herlitcius Y.,Teslya V.G. Experimental industrial operation of a pilot equipment for groundwater purification at the Tunguska water intake. Water Supply and Sanitary Technique. **2012**, *7,* 29-35 [in Rus].

16. Kulakov V.V. Biogeochemical aspects of Priamurye groundwater purification. Russian Journal of Pacific Geology. **2008**, *27, 1*, 109-118 [in Rus].

17. Duyck C., Miekeley N. Trace element determination in crude oil and its fractions by inductively coupled plasma mass spectrometry using ultrasonic nebulization of toluene solutions. *Spectrochimica Acta*, **2008**, *57*,1979-1990. https://doi.org/10.1016/S0584-8547(02)00171-4

18. Boldirev K.A. Geochemical simulation of intrastrata reironing and remanganization of underground water. *Water Supply and Sanitary Technique.* **2013**, *4*, 49-55 [in Rus].

19. Samtanova D.E. Characteristcs of strata water of oil sources of Kalmykia Republic as an important pollutants at oil production.: diss. Ph.D.: 03.02.08. Ivan. state. him. tehnol. un-t. - B.m. - 2017. - 175 p [in Rus].

20. Yurchenko A.O. Spectral methods of investigation. Sientific and methodic tasks of physical education. **2013**, *1(5),*160-166 [in Ukr].

21. O.I. Yurchenko, N.P. Titova, Sabir Karwan Salih Sabir, T.V. Chernozhuk. Atomic absorption and atomic emission with inductively coupled plasma determination of copper in petroleum products. *Kharkiv Univ. Bull., Chem. Ser.* **2016**, *27*, 79-83 [in Ukr].

22. Maznyaka N.V., Verhoturova A.P., Loseva V.N., Zamay T.N. Sodium and potassium determination in biological objects by the mehods of atomic absorption and atomic emission spectroscopy. *Journal of Siberian Federal University. Chemistry*, **2012**, *3(5),* 320-330 [in Ukr].

23. Fischbach F.T. *Manual of Laboratory and Diagnostic Tests*. N.Y.: Lippincott Willians Wilkins, 2008.

24. Biletska E.M., Onul N.M., Bezub O.V. Hygienic aspects of lead osteotropicity as a risk factor of calcium-deficit pathology in man. *Medical perspectives,* **2014**, *2*, 130-138 [in Rus]. https://doi.org/10.26641/2307-0404.2014.2.28461

25. Alemasova A.S., Zaycev V.M., Enaleva L.Ya. *Analytical chemistry.* Doneck: "Knowledge", 2010 [in Ukr].

26. Alemasova A.S., Rokun A.M., Shevchuk I.O. *Analytical atomic absorption spectroscopy.* Manual. Sevastopol: «Veber», 2003 [in Ukr].

О.И. Юрченко, Т.В. Черножук, А.А. Кравченко. Атомно-абсорбционное и атомно-эмиссионное с индуктивно-связанной плазмой определение свинца и железа в пластовых водах с использованием новых сред и стандартных образцов.

Харьковский национальный университет имени В.Н. Каразина, химический факультет, пл. Свободы, 4, Харьков, 61022, Украина.

Изучено влияние концентрации поверхностно-активного вещества (Тритон X-100) и времени обработки ультразвуком на величину аналитического сигнала при атомно-абсорбционном и атомно-эмиссионном с индуктивно-связанною плазмой определении аналитов в пластовых водах. Максимальный аналитический сигнал при определении свинца и железа был достигнут при использовании неионогенного поверхностно-активного вещества, что позволило уменьшить поверхностное натяжение анализируемого раствора и увеличить адсорбцион-

ность при определении аналитов. Показано, что при использовании современной пробоподготовки чувствительность атомно- абсорбционного определения свинца увеличивается в 1.5, а железа в 1.8 раза. Методами атомно-абсорбционной и атомно-эмиссионной с индуктивно-связанной плазмой спектроскопии определено содержание свинца и железа в пластовых водах с использованием ацетилацетонатов свинца и железа в качестве стандартных образцов состава, что позволило значительно повысить прецезионность и точность определения аналитов. Путём варьирования объема образца и методом «введено–найдено» было показано, что систематическая погрешность не значительна. Согласование результатов, полученных двумя независимыми методами, оценено согласно F– и t– критериям. Показано, что дисперсии однородны, а разброс средних не значителен, и оправдан случайным образом. Атомно-абсорбционным методом оценен предел обнаружения аналитов согласно разработанной методике, и показано, что полученные результаты ниже литературных. Разработанная методика, по метрологическим характеристикам, является конкурентоспособной на мировом уровне.

Ключевые слова: пластовые воды, пробоподготовка, атомно-абсорбционая и атомно-эмиссионная с индуктивно-связанной плазмой спектроскопия, свинец, железо, Тритон Х-100, ультразвук, ацетилацетон, ацетилацетонаты свинца и железа, метрологические характеристики.

O.I. Yurchenko, T.V. Chernozhuk, O.A. Kravchenko. Atomic absorption and atomic emission with inductive connected plasma detection of Lead and Iron in strata water using new medias and standard composition samples.

V.N. Karazin Kharkiv National University, School of Chemistry, 4 Svobody sqr.,61022 Kharkiv, Ukraine

An influence of SAS (Triton X-100) concentration and ultrasound treatment time on the value of analytical signal at atomic absorption and atomic emission with inductive connected plasma detection of analytes in strata water was studied. Maximal analytical signal at of Lead and Iron was reached at using nonionogenic SAS which let us to decrease surface tension of the analyzed solution and to increase absorptivity at analytes detection. It was shown that using of the modern sample preparation increase sensibility of atomic absorption detection of Lead in 1,5 times and Iron in 1,8 times. By the methods of atomic absorption and atomic emission with inductive connected plasma spectroscopy and using acetylacetonates of Lead and Iron as standard composition samples, that let us to increase sensitivity of the detection of analytes, contain of Lead and Iron in strata water was determined. By variation of the sample volume and by "injected-found out" method we have proved that systematic error is not significant. The results, obtained by two independent methods were compared according to F- and t-criteria. It was proved that dispersions are homogenous and run of the means is not sufficient and proved by random scatter. By atomic absorption method we estimated the detection limit of the analytes according to the developed methodic and show that the obtained results are lower than the same data from literature. The developed methodic, according to its metrological characteristics, is competitive at international level.

Keywords: strata water, sample preparation, atomic absorption and atomic emission with inductive connected plasma spectroscopy, Lead, Iron, Triton X-100, ultrasound, acetylacetone, acetylacetonates of Lead and Iron metrological characteristics.

ЕТИЧНІ НОРМИ ПУБЛІКАЦІЇ НАУКОВИХ РЕЗУЛЬТАТІВ ТА ЇХ ПОРУШЕННЯ. Редакційна колегія робить все можливе для дотримання етичних норм, прийнятих міжнародним науковим товариством, і для запобігання будь-яких порушень цих норм. Така політика є важливою умовою плідної участі журналу в розвитку цілісної системи знань в галузі хімії та суміжних галузях. Діяльність редакційної колегії значною мірою спирається на рекомендації Комітету з етики наукових публікацій (Committee of Publication Ethics), а також на цінний досвід міжнародних журналів та видавництв. Подання статті на розгляд означає, що вона містить отримані авторами нові нетривіальні наукові результати, які раніше не були опубліковані. Кожну статтю рецензують щонайменше два експерти, які мають усі можливості вільно висловити мотивовані критичні зауваження щодо рівня та ясності представлення матеріалу, його відповідності профілю журналу, новизни та достовірності результатів. Рекомендації рецензентів є основою для прийняття остаточного рішення щодо публікації статті. Якщо статтю прийнято, вона розміщується у відкритому доступі; авторські права зберігаються за авторами. За наявності будь-яких конфліктів інтересів (фінансових, академічних, персональних та інших), учасники процесу рецензування мають сповістити редакційну колегію про це. Всі питання, пов'язані з можливим плагіатом або фальсифікацією результатів ретельно обговорюються редакційною колегією, рівно як спори щодо авторства та доцільність роздроблення результатів на невеличкі статті. Доведені плагіат чи фальсифікація результатів є підставами для безумовного відхилення статті.

STATEMENT ON THE PUBLICATION ETHICS AND MALPRACTICE. The Editorial Board has been doing its best to keep the ethical standards adopted by the world scientific community and to prevent the publication malpractice of any kind. This policy is considered to be an imperative condition for the fruitful contribution of the journal in the development of the modern network of knowledge in chemistry and boundary fields. The activity of the Editorial Board in this respect is based, in particular, on the recommendations of the Committee of Publication Ethics and valuable practice of world-leading journals and publishers. The submission of a manuscript implies that it contains new significant scientific results obtained by authors that where never published before. Each paper is peer reviewed by at least two independent experts who are completely free to express their motivated critical comments on the level of the research, its novelty, reliability, readability and relevance to the journal scope. These comments are the background for the final decision about the paper. Once the manuscript is accepted, it becomes the open-access paper, and the copyright remains with authors. All participants of the review process are strongly asked to disclose conflicts of interest of any kind (financial, academic, personal, etc.). Any indication of plagiarism or fraudulent research receives extremely serious attention from the side of the Editorial Board, as well as authorship disputes and groundless subdivision of the results into several small papers. Confirmed plagiarism or fraudulent research entail the categorical rejection of the manuscript.

ЭТИЧЕСКИЕ НОРМЫ ПУБЛИКАЦИИ НАУЧНЫХ РЕЗУЛЬТАТОВ И ИХ НАРУШЕНИЯ. Редакционная коллегия делает все возможное для соблюдения этических норм, принятых международным научным сообществом, и для предотвращения любых нарушений этих норм. Такая политика является необходимым условием плодотворного участия журнала в развитии целостной системы знаний в области химии и смежных областях. Эта деятельность редакционной коллегии опирается, в частности, на рекомендации Комитета по этике научных публикаций (Committee of Publication Ethics), а также на ценный опыт авторитетных международных журналов и издательств. Представление статьи на рассмотрение подразумевает, что она содержит полученные авторами новые нетривиальные научные результаты, которые ранее нигде не публиковались. Каждую статью рецензируют минимум два эксперта, которые имеют все возможности свободно высказать мотивированные критические замечания относительно уровня и ясности изложения представленного материала, его соответствия профилю журнала, новизны и достоверности результатов. Рекомендации рецензентов являются основанием для принятия окончательного решения о публикации статьи. Статья, в случае принятия к опубликованию, размещается в открытом доступе; авторские права сохраняются за авторами. При наличии каких-либо конфликтов интересов (финансовых, академических, личных и т.д.) участники процесса рецензирования должны сообщить об этом редколлегии. Любые спорные вопросы, связанные с возможным плагиатом или фальсификацией результатов, внимательно рассматриваются редакционной коллегией, равно как споры об авторстве и целесообразность дробления результатов на небольшие статьи. В случае подтверждения плагиата или фальсификации результатов статья безоговорочно отклоняется.

ІНФОРМАЦІЯ ДЛЯ АВТОРІВ. Журнал публікує статті російською, англійською та українською мовами. До публікації приймаються: огляди (за погодженням з редколегією); оригінальні статті, обсяг 6-10 журнальних сторінок; короткі повідомлення, обсяг до 3 журнальних сторінок. Крім звичайного списку літератури, в статті обов'язково повинен бути другий список, всі посилання якого дані латиницею. Правила підготовки цього списку наведені в розділі «Транслітерація» на сайті журналу. Обидва списки повинні бути повністю ідентичні. При рецензуванні статей один з критеріїв - наявність посилань на публікації останніх років. Стаття обов'язково повинна містити резюме російською, українською та англійською мовами. У всіх трьох необхідно вказати назву статті, прізвища авторів і ключові слова. Орієнтовний обсяг резюме - 1800 знаків (без урахування заголовку і ключових слів). Редакція приймає електронний (MS Word) і два роздрукованих (для харків'ян) тексту рукопису. Адреси вказані в розділі «Контакти» на сайті журналу. Супровідний лист до статті, виправленої відповідно до зауважень рецензента, повинен містити відповіді на всі зауваження. Подається електронний і один роздрукований (для харків'ян) варіант. Рукописи, які пройшли рецензування, прийняті до публікації і оформлені відповідно до правил для авторів, приймаються у форматі doc (не docx) електронною поштою (chembull@karazin.ua). Роздрукований варіант не потрібен. Докладніша інформація розміщена на сайті журналу http://chembull.univer.kharkov.ua.

INFORMATION FOR AUTHORS. Papers in Ukrainian, Russian and English are published. These may be invited papers; review papers (require preliminary agreement with Editors); regular papers; brief communications. In preparing the manuscript it is mandatory to keep the statement on the publication ethics and malpractice, which can be found on the web-site and in each issue. The article should contain summaries in English, Russian, and Ukrainian. In all three it is necessary to indicate the title of the article, the names of the authors and the keywords. The approximate volume of summary is 1800 characters (excluding the title and key words). The help in translation is provided by request for foreign authors.. Any style of references is acceptable, but all references within the paper must be given in the same style. In addition, the second, transliterated, list of references is required if at least one original reference is given in Cyrillic. See section "Transliteration" of the web-site for details. Please use papers of previous issues as samples when prepare the manuscript. The MS Word format is used. Standard fonts (Times New Roman, Arial, Symbol) are preferable. Figures and diagrams are required in vector formats. Figure captions are given separately. All figures, tables and equations are numbered. Please use MS Equation Editor or MathType to prepare mathematical equations and ISIS Draw to prepare chemical formulas and equations. The decimal point (not coma) is accepted in the journal. Please avoid any kind of formatting when prepare the manuscript. Manuscripts may be submitted to the Editor-in-Chief via e-mai chembull@karazin.ua. For more detailed information see the journal web-site http://chembull.univer.kharkov.ua.

ИНФОРМАЦИЯ ДЛЯ АВТОРОВ. Журнал публикует статьи на русском, английском и украинском языках. К публикации принимаются: обзоры (по согласованию с редколлегией); оригинальные статьи, объем 6-10 журнальных страниц; краткие сообщения, объем до 3 журнальных страниц. Помимо обычного списка литературы, в статье обязательно должен быть второй список, все ссылки которого даны латиницей. Правила подготовки этого списка приведены в разделе «Транслитерация» на сайте журнала. Оба списка должны быть полностью идентичны. При рецензировании статей один из критериев - наличие ссылок на публикации последних лет. Статья обязательно должна содержать резюме на русском, украинском и английском языках. Во всех трех необходимо указать название статьи, фамилии авторов и ключевые слова. Ориентировочный объем резюме - 1800 знаков (без учета заглавия и ключевых слов). Редакция принимает электронный (MS Word) и два распечатанных (для харьковчан) текста рукописи. Адреса указаны в разделе «Контакты» на сайте журнала. Сопроводительное письмо к статье, исправленной в соответствии с замечаниями рецензента, должно содержать ответы на все замечания. Подается электронный и один распечатанный (для харьковчан) вариант. Прошедшие рецензирование и принятые к публикации рукописи, оформленные в соответствии с правилами для авторов, принимаются в формате doc (не docx) по электронной почте (chembull@karazin.ua). Распечатанный вариант не требуется. Более подробная информация размещена на сайте журнала http://chembull.univer.kharkov.ua.